UNIVERSITAT POLITÈCNICA DE CATALUNYA

DEPARTAMENT DE FÍSICA I ENGINYERIA NUCLEAR

# Determination of Longitudinal Electron Bunch Lengths on Picosecond Time Scales

PhD. Thesis submitted by

Cèsar Martínez

*Supervisors:*
Dr. H. Braun (CERN)
Dr. F. Calviño (UPC)

September 1999

## Acknowledgements

I would like to thanks all the people who has supported me in any way during my stay at CERN. I give my warmest thanks to all the members of the "CTF team", without whose constant help this thesis would not have been possible and specially to Hans Braun, responsible of the CTF and my supervisor at CERN, for his constant support, advice and for the fruitful discussions we had during the last three years.

Special thanks goes to my university supervisor, Francisco Caliviño, for his help, guidance and support during my stays at SEN and at CERN. Thanks also to SEN for hosting me as a PhD student.

I would also like to thanks the European Laboratory for Particle Physics for the award of a Doctoral Grant and especially the LP group for its hospitality during my stay at CERN.

And last but not least to all my friends who have always encouraged and supported me.

# Summary

At CERN (European Laboratory for Particle Physics) the CLIC (Compact Linear Collider) study is pursuing the design of an electron-positron high-energy linear collider using an innovative concept for the RF (Radio Frequency) power production, the so-called two-beam acceleration scheme. In order to keep the length of the collider in a reasonable range while being able of accelerating electrons and positrons up to 5 TeV, the normal-conducting accelerating structures should operate at very high frequency (in this case 30 GHz). The RF power necessary to feed the accelerating cavities is provided by a second electron beam, the drive beam, running parallel to the main beam.

The CLIC Test Facility (CTF) was build with the main aim of studying and demonstrating the feasibility of the two beam acceleration scheme and technology. It is composed of two beams, the drive beam that will generate the 30 GHz RF power and the main beam which will be accelerated by this power. In order to have a good efficiency for the power generated by the drive beam, the length of the drive beam electron bunches has to be shorter than 2 ps rms. Conventional bunch length measurement techniques did not have the required resolution or were destructive. An innovative approach is based on the measurement of the bunch spectrum using non-intercepting pick-ups.

The new bunch length monitor measures the frequency spectrum of the electromagnetic field of the bunch. The bunch length is obtained by studying the variation of the signal amplitude with frequency. Due to the small bunch lengths very high frequencies have to be measured, so that the monitor becomes a microwave spectrometer. The electromagnetic field of the bunch is collected by a rectangular RF pick-up connected to a waveguide of the same dimensions that leads the signal to the detection system. The field induced in the waveguide has a temporal evolution directly related to that of the electron bunch. Hence, it is possible to derive the spatial charge distribution from the frequency spectrum of that signal.

Detection is made either by a diode detector or by a combination of RF mixers with a RF sweeping oscillator. The diode detector allows single shot measurements and has proven to be a very fast qualitative method to observe variations in the bunch length. However, this method proved out to be very difficult to calibrate and is not suitable for measuring bunch trains due to interference effects. The mixing technique makes use of two RF mixers. The first one, with a local oscillator set at a fixed frequency $\nu$, down-shifts the frequency spectrum of the incoming RF signal by an amount $\nu$. The second mixers has a sweeping oscillator as a source, with each frequency step of the oscillator the mixer down-shifts the RF signal by a different quantity, allowing a digitizing oscil-

loscope to detect the part of the spectrum within its bandwidth. By sweeping over some given frequency range the oscilloscope will measure the frequency spectrum amplitude in this range. This technique can not only measure the frequency spectrum of a single bunch but also of a train of bunches. Furthermore, an independent self-consistent calibration procedure was developed and successfully applied to this detection system.

Two RF pick-ups have been installed in the CTF drive linac. One for the so called WR28 waveguide and the other for the so called WR12 waveguide. The two pick-up together with the proper detection system, allow the measurement of the signal in three frequency ranges, 28.5–40.5 GHz, 58.5–60.5 GHZ and 76.5–88.5 GHz. Experiments performed in the CTF, with a train of 48 bunches, have shown a very good agreement between the values measured with the mixing technique and the values obtained with the simulation programme PARMELA. Moreover, the experimental results demonstrated the capability of the system to measure bunches as short as 0.7 ps rms.

# Contents

# List of Figures

# List of Tables

# Chapter 1

# Introduction

Beam diagnostics plays a crucial role in the operation of any particle accelerator by providing information on the beam properties and behaviour. In this way the proper operational conditions can be established for both, the routine operation of accelerators and for machine developments. Each accelerator type has very different requirements concerning the diagnosis of the beam and each one requires a specialised study and, quite often, the development of new methods and tools, as it is the case for the CTF (Compact Linear Collider Test Facility) at CERN (European Laboratory for Particle Physics). The design parameters of this facility demand the generation of very intense and short electron bunches (on a picosecond scale). This thesis report deals with the design, construction, commissioning and operation of a novel non-intercepting bunch length monitor capable of resolving sub-picosecond bunch lengths. The system is currently implemented in the CTF beam line and it is used during routine operation.

## 1.1 High-Energy Colliders

At CERN, Geneva (Switzerland), the construction of the newest high-energy collider, the LHC (Large Hadron Collider) has already started [1]. LHC is a proton-proton circular collider, of 27 Km of circumference, using superconducting technology to make the proton beams collide at a centre of mass energy of 14 TeV. However, the international scientific community, under the auspices of the International Committee for Future Accelerators (ICFA), is already studying the design of the next high-energy collider.

These studies are mainly focussed to three different types of colliders: electron-positron linear colliders, muon-muon colliders and very large hadron colliders. In the framework of the analysis of a new electron-positron linear collider, the CLIC (Compact

Linear Collider) study [2] is being carried out at CERN, where some crucial aspects of the CLIC design have been and are being investigated in the CLIC Test Facility (CTF).

## 1.2 The CLIC study

The CLIC project is designing an electron-positron linear collider, that is two linear accelerator that will lead electrons to head-on collisions with positrons, with a centre of mass energy from 0.5 TeV to 5 TeV [3]. In order to limit the overall length, high accelerating fields are mandatory and these can only be obtained with RF accelerating structures operating at a high frequency. The choice of 30 GHz is considered to be close to the limit beyond which standard technology for the fabrication of normal-conducting travelling-wave accelerating structures can no longer be used [4]. The main parameters of the CLIC design are listed in Table 1.1.

Since pulsed high power power sources at 30 GHz do not exist the 30 GHz RF power necessary to feed the accelerating structures is extracted from a second electron beam, the so-called drive beam, running parallel to the main beam by means of power extracting and transfer structures [5]. This concept is called the Two Beam Acceleration scheme (TBA). A general layout of the CLIC complex at 3 TeV is shown in Figure 1.1.

| | | | | |
|---|---|---|---|---|
| Centre of mass energy | [TeV] | $2\,U_b$ | 0.5 | 3 |
| Luminosity | $[10^{34}\mathrm{cm}^{-2}\mathrm{s}^{-1}]$ | L | 0.5 | 10.6 |
| Number of photons/elecron | | $n\gamma$ | 0.8 | 2.2 |
| Linac repetition rate | [Hz] | $f_R$ | 200 | 75 |
| Number of particles/bunch | $[10^9\ e^{\pm}]$ | $N_b$ | 4.0 | 4.0 |
| Number of bunches/pulse | | $k_b$ | 150 | 150 |
| Bunch spacing | [ns] | $\Delta_b$ | 0.67 | 0.67 |
| Transverse emittances | $[10^{-8}\mathrm{rad\ m}]$ | $\gamma\varepsilon_{x/y}$ | 188/10 | 60/1 |
| Bunch width | [nm] | $\sigma_{x/y}$ | 196/4.5 | 40/0.6 |
| Bunch length | [$\mu$m] | $\sigma_z$ | 50 | 30 |
| Beam power per beam | [MW] | $P_b$ | 4.81 | 10.81 |
| RF frequency | [GHz] | $\frac{\omega}{2\pi}$ | 30 | 30 |
| Accelerating field | [MV/m] | G | 100 | 150 |
| Total length | [km] | $L_S$ | 6.6 | 27.5 |
| RF power per section | [MW] | $P_S$ | 116 | 231 |
| RF pulse length | [$\mu$s] | $\Delta_K$ | 0.121 | 0.121 |
| AC to beam efficiency | [%] | $\eta_{\mathrm{beam}}^{\mathrm{AC}}$ | 14.18 | 10.65 |

Table 1.1: Some parameters of the 0.5 and 3 TeV CLIC designs.

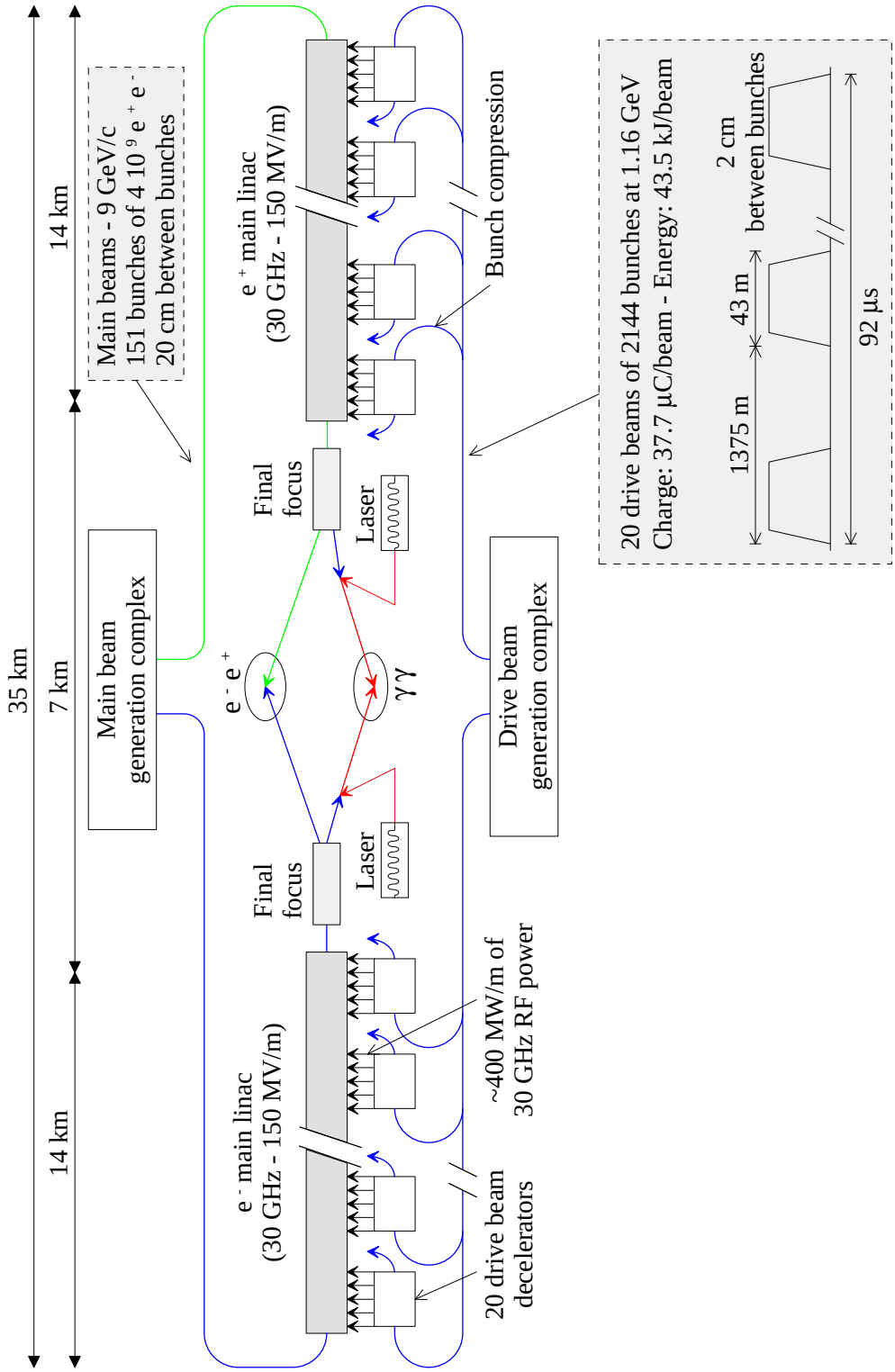


Figure 1.1: Overall layout of the CLIC complex at 3 TeV C.M.

Figure 1.2 shows the layout of the 30 GHz RF power transfer from the high-intensity low-energy drive beam to the low-intensity high-energy main beam. The drive beam is decelerated in the transfer structures, the energy loss is converted in 30 GHz power by means of specially designed corrugated waveguides and it is transferred to the accelerating structures through standard waveguides. In order to have a good power production efficiency, the electron bunches in the drive beam have to be shorter than 2 ps rms.

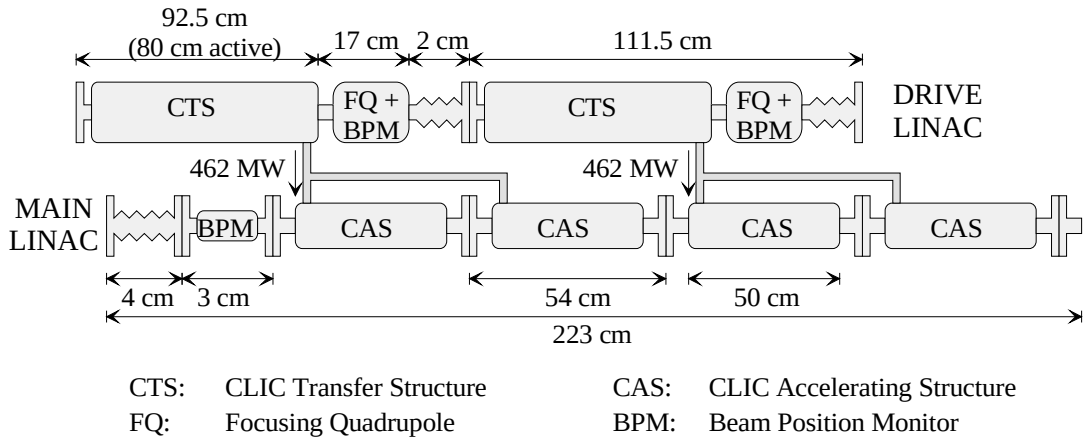


Figure 1.2: Layout of the CLIC Transfer and Accelerating modules (3 TeV C.M.).

## 1.3 The CLIC Test Facility

CTF II is the experimental facility of the CLIC study dedicated to demonstrate the feasibility of the CLIC two-beam accelerator scheme and its associated 30 GHz technology. In the frame of the CLIC studies, CERN has built two facilities: CTF I [6, 7], which has been operated from 1990 to 1995, and CTF II [8, 9], which is presently in operation.

CTF I was mainly dedicated to drive-beam and 30 GHz power production studies. A high impedance, disk-loaded, 30 GHz accelerating structure was used as the drive beam power extracting structure and produced 76 MW at 30 GHz. This power was used to establish an accelerating field of 94 MV/m in a 30 GHz accelerating structure. The first bunch of the drive beam was used to probe the accelerating field.

CTF II is the prototype of a two-beam accelerator, its layout with the two beam lines is shown in Figure 1.3. The drive beam generates power at 30 GHz, while the main beam probes the accelerating field in the 30 GHz accelerator. Both beams are generated by S-band RF-photo-injectors whose photo-cathodes [10, 11] are illuminated by short UV laser pulses (3.5 ps rms) [12]. Before injection in the 30 GHz two-beam accelerator, both beams are accelerated in S-band, disk-loaded structures and after acceleration the

drive-beam bunches are compressed in a magnetic chicane. The latter is essential for efficient power production at 30 GHz. The two-beam test accelerator consists of two fully-engineered CLIC building blocks. The test accelerator is equipped with a prototype micron-precision active-alignment system [13] in order to gain experience in a real accelerator environment. The CLIC Test Facility (CTF II) is described in more detail in the next section.

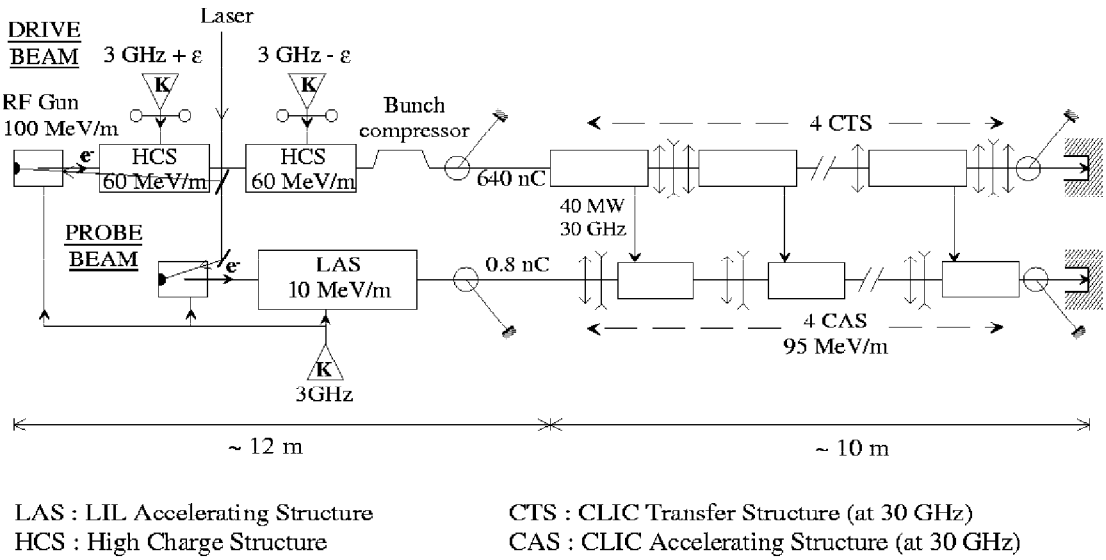


Figure 1.3: Layout of the CTF2.

### 1.3.1 The CTF II

A major challenge of CTF II is the production and transport of the drive-beam train, made of intense (13.4 nC) and short (2 ps rms) bunches, which is needed to produce the required microwave power for the main-beam acceleration. Some relevant design parameters of the drive and main beams are presented in Table 1.2.

The main beam is generated in a 2-cell RF photo-injector (M1) and operates with a single bunch of 1 nC charge. A second bunch, with a variable delay relative to the first, can be switched on to allow wakefield studies in the 30 GHz structures. Before being injected into the 30 GHz accelerator the main beam is accelerated up to about 46 MeV in an S-band travelling wave structure (M2). This is necessary to obtain a geometric emittance that is small enough to fit into the acceptance of the 30 GHz accelerating structures (M3), which have a beam aperture of only 4 mm in diameter. Magnetic spectrometers (M4) before and after the 30 GHz accelerator are used to measure the main beam energy.

| | Drive beam | | Main beam | |
|---|---|---|---|---|
| Beam energy | 60 | MeV | 45 | MeV |
| Pulse repetition frequency | 5 | Hz | 5 | Hz |
| Number of trains per pulse | 1 | | 1 | |
| Number of bunches per train | 48 | | 1–2 | |
| Bunch repetition frequency | 3 | GHz | variable | |
| Charge per bunch | 13.4 | nC | 1 | nC |
| Total charge per pulse | 640 | nC | 1 | nC |
| Bunch length (rms) | 2 | ps | 2.5 | ps |
| Drive beam 30 GHz decelerating field | 7.6 | MV/m | | |
| Probe beam 30 GHz accelerating field | | | 95 | MV/m |

Table 1.2: Main parameters of the CTF2 drive beam.

The drive beam is generated in a 2+1/2-cell RF photo-injector (D1) specially designed for high-charge acceleration [14]. At the design specifications, the photo-injector operates at a field of 100 MV/m and generates a train of 48 bunches with a bunch spacing of 10 cm and total charge of 640 nC. The train energy at the photo-injector exit is 7 MeV and the total energy spread due to beam loading is about 20%. The photo-injector is followed by two travelling wave S-band structures (D2) optimised for high-charge acceleration [15]. In order to provide approximate compensation of the beam loading, one of the accelerators is operated at +7.81 MHz while the other works at -7.81 MHz with respect to the bunch repetition frequency. The chosen accelerator frequencies reduce the residual train energy spread to about 7%.

As a result of the laser pulse length on the photocathode, longitudinal focusing RF forces and defocusing space-charge forces, the bunch length after acceleration is about 3.4 ps rms at the nominal charge. Since efficient 30 GHz power production requires shorter bunch lengths, a magnetic chicane (D3), together with optimised phasing in the accelerating structures, is used to compress the bunches to 2 ps rms [16, 17]. After the bunch compressor, the beam is injected into the 30 GHz decelerator (D4) where a part of its energy is converted into 30 GHz power. A downstream spectrometer magnet (D5) measures the energy spectrum of the beam after power extraction.

The CTF II 30 GHz two-beam accelerator consists of prototypes of CLIC modules, equipped with 30 GHz Power Extraction and Transfer Structures (CTS), 30 GHz disk-loaded accelerating structures and 30 GHz beam monitoring equipment. Since operation at high frequency requires tight alignment tolerances, each module of the 30 GHz two-beam accelerator is equipped with a micron-precision active alignment system, consisting of beam position monitors and actuators.

The 30 GHz accelerating sections are fully-engineered CLIC prototype accelerating sections optimised for single-bunch acceleration (i.e. they are not detuned or damped to suppress wakefields). The sections are manufactured to micron tolerances using parts made on ultra-precision diamond-tool lathes.

The 30 GHz Power Extraction and Transfer Structures (CTS) consist of a 15 mm diameter circular tube coupled by 4 slots to the broad sides of four corrugated rectangular waveguides. In order to selectively damp the transverse modes, lossy longitudinal slits terminated with resistive materials are cut in symmetry planes of the main decelerating mode. The adopted structures have an effective length of 0.6 m and a design r'/Q of 1080 Ω/m. The extracted power depends quadratically on the charge per bunch, this yields to a power production of 71 MW per structure when operated at design specifications. The decelerating field increases along the structure and reaches 7.6 MV/m at the end, corresponding to a drive-beam deceleration of about 2.3 MeV per structure.

A picture of the longitudinal section of a CTS is shown in Figure 1.4. In this picture can be seen the corrugated waveguides extracting and channelling the power to an output slit. Also visible to the right is a piece of SiC damping material to selectively damp the transverse modes.

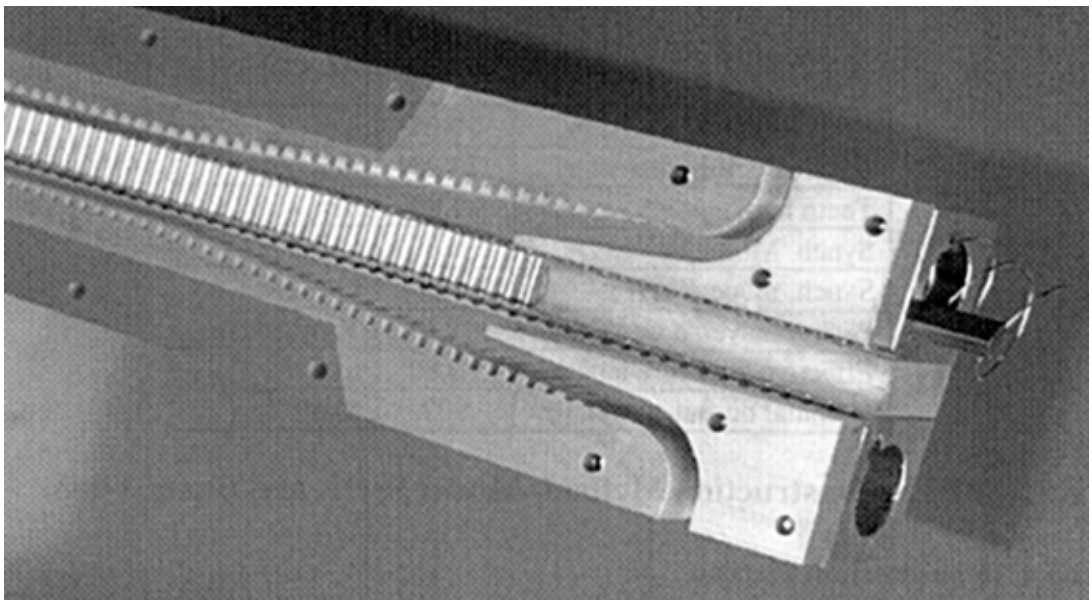

Figure 1.4: Extremity of open CTS with ouput couplers and channels.

**Two-Beam Acceleration and Power Production at 30 GHz**

Recently, experiments performed at the CTF II demonstrated the viability of the two-beam acceleration and power production at 30 GHz by simultaneously passing the drive beam through the 30 GHz decelerator and the main beam through the 30 GHz accelerator [18].

At present two power extraction structures are installed in the 30 GHz decelerator. Each power extraction structure is connected to one 30 GHz accelerating structure of the main beam. A comparison of these design parameters and the measured ones is given in Table 1.3. To date 27 MW at 30 GHz is produced in the CTS and used to establish a mean accelerating field of 59 MV/m in the 30 GHz accelerator. The total power at 30 GHz was 41 MW and the total main-beam acceleration was 28 MeV. As already experienced in CTF I (at higher power levels), no RF breakdowns were observed in either the 30 GHz waveguide networks or the accelerating structures. The 30 GHz power production is limited, at this moment, by the drive-beam charge that can be transported through the decelerator. Although the maximum accelerated charge exceeds the design goal, the drive-beam transmission through the 30 GHz decelerator is still unsatisfactory. Full transmission is presently achieved up to a drive beam charge of 340 nC. Above this value, the drive beam transmission progressively deteriorates and the maximum transported charge, so far, is 374 nC. Possible reasons for the unsatisfactory behaviour at high charge levels include the gradient in the drive-beam accelerator, which is still below the design value, transverse matching problems and various problems concerning the laser system.

| | Design specification | | Achieved performance | |
|---|---|---|---|---|
| Maximum drive beam accelerated charge | 640 | nC | 755 | nC |
| Drive beam charge during experiments | 640 | nC | 475 | nC |
| Maximum drive beam charge through CTS | 640 | nC | 374 | nC |
| Number of drive beam bunches | 48 | | 48 | |
| Drive beam bunch length (rms) | 2 | ps | 2 | ps |
| 30 GHz power from CTS | 71 | MW | 27 | MW |
| 30 GHz power pulse length | 14 | ns | 14 | ns |
| Mean accelerating field in HCS | 95 | MV/m | 59 | MV/m |
| Maximum probe beam acceleration | 47 | MeV | 28 | MeV |

Table 1.3: Design specification and current performance in the CTF2.

## 1.4 A New Bunch Length Monitor

One of the crucial issues of the CTF II is the generation of very short bunches (2 ps rms or less) and the possibility to monitor and measure such short lengths. The work presented in this report covers the crucial subject of measuring such short bunches. At the moment the work started, the bunch length in the CTF was measured by means of a streak camera to analyze transition or Cerenkov radiation produced by a screen inserted in the beam path. This method presents two major drawbacks, first the use of a screen in the beam path spoils the beam characteristics and lead to beam losses as well as to radiation hazards, due to the high beam intensity. Secondly, the resolution of the measurement is limited to about 2 ps rms. After a thorough study of the state of the art in very short bunch lengths measurements, it was decided to design a new system based on the determination of the bunch frequency spectrum using microwave spectroscopy.

The bunch spectrum is picked-up by a rectangular waveguide coupled to the beam pipe. The signal is then analyzed with either fast diode detectors or by a RF mixer in combination with a RF sweep oscillator. The diode detector gives real-time monitoring of the variation of the bunch length, while the mixer set-up allows quantitative bunch measurements for both, single bunches and train of bunches. The mixing technique has been adopted as the detection system for bunch length measurements. Such system has the advantages of being non-intercepting, self-calibrating, easy to implement in the beam line and relatively low-cost (compared, for example, to a streak camera).

The thesis work includes the design, the installation, the commissioning and the operation of the new monitor. The design task includes the choice of the signal pick-up, the system to transport the signal and the design of the detection system. During the operation of the monitor it was demonstrated its capability to measure bunches as short as 0.7 ps rms. It should be remarked that a self-consistent calibration procedure has been developed to obtain and independent and absolute calibration of the monitor.

In Chapter 2 is described the state of the art of bunch length measurement techniques. These methods can be categorised in time domain methods and frequency domain methods. Some of them are capable of measuring picosecond electron bunches but they cannot be used in linacs or they are destructive. Since some methods use the radiation emitted by the electron bunches a short introduction to different types of radiation (transition, Cerenkov and synchrotron) is also given.

Chapter 3 covers the design of the bunch length monitor adopted in the CTF. First it is explained how to reconstruct the bunch length from the bunch spectrum, both for a single bunch and a train of bunches. The frequency response of the RF pick-up is studied

by using the computer code MAFIA and the transport of the signal with waveguides is calculated analytically. Two detection systems are adopted, the first consisting of a fast diode detector which allows real time monitoring of the variation of the bunch length. The second, a series of microwave mixers in combination with a sweeping RF source, acting as a spectrum analyzer, which can measure the length of single bunches and trains of bunches.

Chapter 4 deals with the experimental set-up of the bunch length monitor in the CTF and the data acquisition procedure. Typical signals obtained with both detection methods are also shown.

In Chapter 5 and 6 the experimental results and their analysis are presented and discussed. The experimental signals are shown and compared with the expected ones. The explanations of unexpected effects are given. A description of different calibration procedures is also presented. The results obtained with the mixing technique are compared with the values measured with a streak camera and with the predictions of the simulation programme PARMELA. These comparison show, first, that the streak camera resolution is limited to 2 ps and second that the microwave monitor is in very good agreement with the bunch length values predicted by PARMELA.

Finally the conclusions are discussed.

# Chapter 2

# Methods for Measuring the Length of Electron Bunches

Direct measurement (i.e. with a pick-up and an oscilloscope) of the length of bunches of electrons with $\sigma \leq 1$ ns, is very difficult, thus more elaborate techniques have been developed. In this chapter several methods for measuring the length of short bunches are reviewed [19]. The different techniques can be divided into two main areas, time domain methods and frequency domain methods.

- The time domain methods reviewed are,
  - Picosecond photoconductive detectors
  - Streak camera
  - RF deflector
  - Spectrometer
- The frequency domain methods described are,
  - Coherent radiation
  - Microwave spectroscopy

Some of these methods require the use of the radiation emitted by the electron bunch, therefore a brief introduction to different types of radiation emitted by charged particles is given first.

## 2.1 Radiation Emitted by a Charged Particle

A charged particle (e.g. an electron) in motion can emit electromagnetic radiation [20]. Emission can happen when the particle is accelerated(or decelerated); this radiation is usually called bremsstrahlung when acceleration is produced by the electromagnetic field of the atomic nuclei of a target element and synchrotron radiation when the acceleration is produced by a external electromagnetic field. There is also emission when the electron changes media, that is, passes through a interface between two media with different refraction index. The latter can be regarded as a special case of acceleration, as a change in the refraction index implies a change of light speed. A different case is the Cerenkov radiation emitted when the speed of an electron travelling in a medium is larger than the speed of light in the medium [21, 22].

It is important to remark that for these types of radiation the emission can be considered to be instantaneous, thus the temporal distribution of the radiation is directly related to that of the bunch of charged particles that emitted it.

- Cerenkov Radiation
  A charged particle moving in a continuum medium at a constant velocity will polarise the medium in the region close to the particle path. If the charge is travelling at a speed higher than the phase velocity of light in this medium, the polarisation will not be symmetric along the particle path and there will be a resultant dipole field along this axis. The radiation emitted at different points of the charge track will be in phase with one another for an emission angle $\theta$ so that the Cerenkov relation,

  $$\cos\theta = \frac{c}{vn(\omega)} \qquad \text{with} \qquad \nu \geqslant \frac{c}{n(\omega)} \tag{2.1}$$

  is fulfilled, where $v$ the velocity of the charge, $c$ the speed of light in vacuum and $n(\omega)$ the refraction index of the medium [23].

- Transition Radiation
  It is emitted by a charged particle moving at constant velocity in an inhomogeneous medium, in a medium changing in time or when passing close to such a medium. In general, a charged particle moving at velocity $v$ (constant) in a medium of refractive index $n(\omega)$ will radiate if the ratio of the particle velocity to the light phase velocity $c_{ph}$

  $$\frac{v}{c_{ph}} = \frac{vn(\omega)}{c} \tag{2.2}$$

changes (where c is the speed of light). It is clear that this ratio can change both due to the variation of $v$ (accelerated particle) and due to a change in the refraction index $n(\omega)$. The simplest problem of this type is the crossing of a boundary between two media by a charge (usually vacuum-metal). Transition radiation can also occur when a charge passes close to some obstacles (diaphragms, slits, etc.), which in this case is called diffraction radiation. Transition radiation is emitted in the forward and backward direction for a particle impinging in a direction normal to a surface, and is strongly peaked at an angle $\theta = \gamma^{-1}$ with respect to the particle trajectory, where $\gamma$ is the Lorentz factor ($\gamma^{-2} = 1 - (v/c)^2$).

- Synchrotron Radiation
  Synchrotron radiation differs from the other types of radiation explained above in the fact that is emitted by charges moving on a non-straight trajectory. In this case the radiation is due to a change, not in the modulus of $\vec{v}$, but in its direction. The radiation is emitted in a direction tangent to the trajectory of the charged particle and within a highly collimated angle of $\pm\gamma^{-1}$. The radiation power is proportional to the fourth power of the particle momentum and inversely proportional to the square of the trajectory radius.

## 2.2 Picosecond Photoconductive Detectors

These detectors are based on fast CdTe (or GaAs) photoconductors and are in use, for instance, at LEP (CERN's Large Electron Positron collider) to measure the bunch length via autocorrelation of the X-ray synchrotron radiation [24, 25].

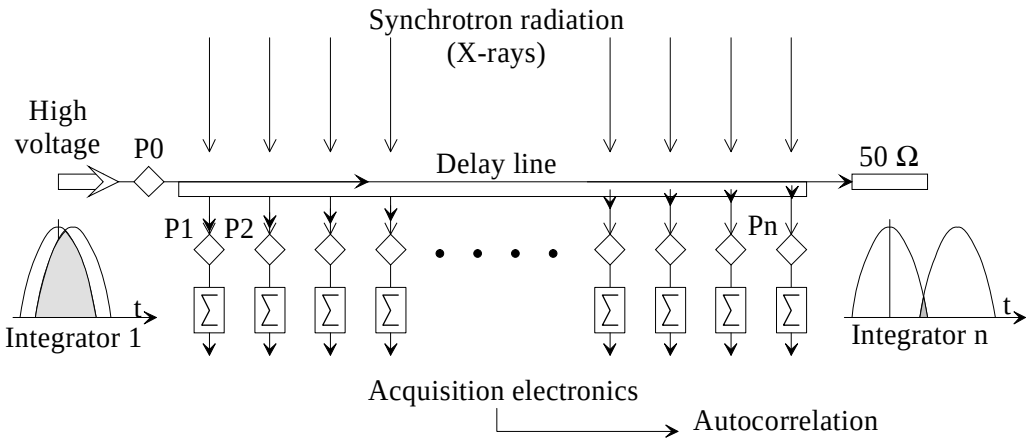


Figure 2.1: Layout of detector principle.

Figure 2.1 shows the basic principle of the detector. The synchrotron light illuminates the fast photoconductors (Pn), that are connected to a delay line. The signal travelling through the delay line comes from the (biased) photoconductor P0. This signal adds up to the signal induced by the synchrotron light with a different delay time in each photoconductor. The integrated signal is then read by the data acquisition electronics and each photoconductor gives a point for the autocorrelation profile of the bunch shape, from where the bunch length can be extracted. The evaluation of the performance with a laser has shown a resolution of 5.7 ps (rms) for the autocorrelation of two photoconductors.

This system allows individual bunch measurements in LEP bunch trains due to the fast response of the detectors and the use of a fast gating (10 ns) for the polarisation (bias) voltage.

## 2.3 Streak Camera

A streak camera is an optoelectronic device able to obtain very high temporal resolution of radiation pulses [26]. In the particle accelerator domain transition, Cerenkov or synchrotron radiation produced by the electron beam are used as sources for the streak camera as their temporal intensity is directly related to that of the electron beam. Therefore, by measuring the length and structure of the light pulse the length and structure of the electron beam is obtained.

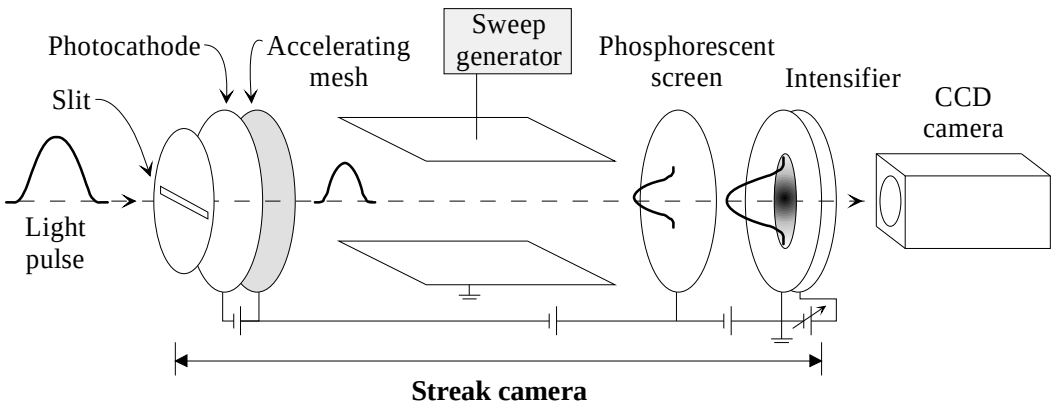


Figure 2.2: Schematic layout of a streak camera.

Usually only a section of the radiation source is investigated, for this purpose a slit is placed at the input of the camera. The photons that pass the slit will hit a photocathode

producing an electron beam with a temporal structure that will be proportional to that of the light pulse. After acceleration these electrons are swept by a deflecting electric field generated by a fast ramped voltage applied to two metallic plates. In this way, the temporal variation of intensity is transformed into spatial information when hitting a phosphorescent screen. The light intensity of the phosphor screen is recorded by a CCD camera. For a schematic layout see figure 2.2.

The resolution of the streak camera will depend on several factors. First the electron energy spread from the photocathode (that will also depend on the chromaticity of the light pulse), second the static image size of the slit and third the electron beam self field effects and the deflection ramp speed. Time resolutions of a few hundred femtoseconds have been achieved measuring monochromatic laser pulses.

## 2.4 RF Deflector

The general principle of this technique is very similar to that of the streak camera, to convert the time information of the beam into transverse spatial information [27], however, a direct measurement is done on the electron beam instead of using radiation emitted by the beam.

In figure 2.3 a schematic layout of a RF-deflector system is shown. The beam goes

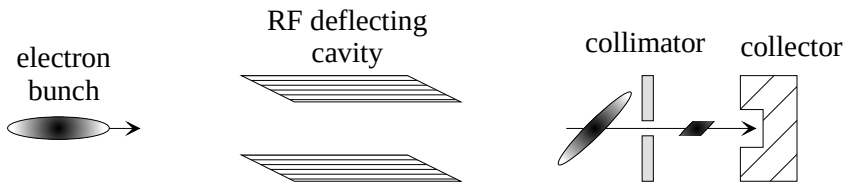


Figure 2.3: Schematic layout of a RF-deflector for bunch shape measurements.

through a RF-deflecting cavity whose deflecting angle depends on the phase of the applied field (that can be adjusted). The beam goes then through a collimator and only the part of the beam with the correct phase passes through the slit to the collector. The intensity distribution of the whole bunch is obtained by changing the phase of the deflecting field, that results in the different portions of the beam passing the slit. A faraday cup can be used as collector device.

The performance of this system is limited by the deflection angle,

$$\text{deflection angle} \gg \frac{\text{emittance}}{\text{beam radius}}$$

by wakefield effects due to interactions of the beam with the deflecting cavity and by uncorrelated energy spread. All this factors reduce the resolution with increasing charge. For low bunch charges, a resolution of 1 *ps* can be achieved.

For high intensity or ion beams, the secondary electrons emitted by the beam when hitting a thin wire can be use for diagnostics [28–30], see Figure 2.4. In this case, the resolution of the measurement will be reduced by the conversion of the main beam into a secondary electron beam.

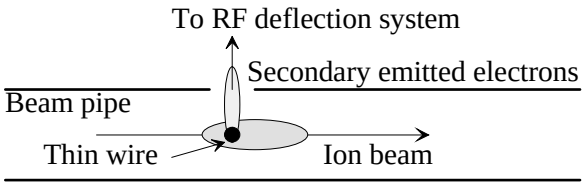


Figure 2.4: Emission of secondary electron by an ion beam hitting a wire.

## 2.5 Spectrometer

The principle is the same than for the previous methods, i.e. transform the time information into transverse spatial information. The electron beam is deflected by a dipole magnet after having gone through a time dependent accelerating field. The effect of the time dependent acceleration is a distribution of particle energy along the bunch relative to its phase. In this way when going through the dipole field every longitudinal section will feel a different field strength (that is proportional to the particle energy) and follow a different trajectory, as the bending radius is proportional to the field strength. Therefore the time (or longitudinal) information will be transformed into transverse spatial information.

This method has the same limitations than the RF-deflector, a good resolution can only be obtained for low charges.

## 2.6 Coherent Radiation

Electromagnetic radiation from electron bunches (Cerenkov, transition, synchrotron) is coherently enhanced at wavelengths which are of the order or longer that the electron bunch length. The frequency spectrum of the coherent radiation carries information of the bunch distribution.

The total intensity of the radiation emitted by a bunch of N electrons at wavelength λ, using far-field approximation, can be expressed as [31]

$$I_{total}(\lambda) = [N + N(N+1)\, f(\lambda)] I_e(\lambda) \tag{2.3}$$

where $I_e(\lambda)$ is the intensity of the radiation emitted by an electron. The coherent part is proportional to $N^2$ and contains the form factor $f(\lambda)$, that is the magnitude squared of the Fourier transform of the bunch distribution $S(\vec{r})$,

$$f(\omega) = \left| \int e^{i\frac{2\pi}{\lambda}\hat{n}\vec{r}} S(\vec{r})\, d\vec{r} \right|^2 \quad \text{and} \quad \int S(\vec{r})\, d\vec{r} = 1 \tag{2.4}$$

where $\hat{n}$ is the unit vector directed from the centre of the bunch to the observation point and $\vec{r}$ is the position vector of an electron relative to its bunch centre. If the radiation is observed in the forward direction from a transversely symmetric beam, the form factor is independent of the transverse bunch distribution, it is therefore determined only by the longitudinal bunch distribution. For wavelengths larger than the bunch length the form factor approaches unity and the total radiation intensity is coherent ($I_{total}(\lambda) \propto N^2$). On the other hand, for wavelengths shorter than the bunch length, the form factor reduces to zero, and the radiation becomes incoherent ($I_{total}(\lambda) \propto N$). If radiation can not be observed in the forward direction (which is the case for transition and Cerenkov radiation) the transverse bunch distribution contributes to the form factor [32]. This contribution can be neglected under certain conditions, nevertheless it is advisable to have a small transverse beam size and small detector angular acceptance for accurate subpicosecond bunch length measurements.

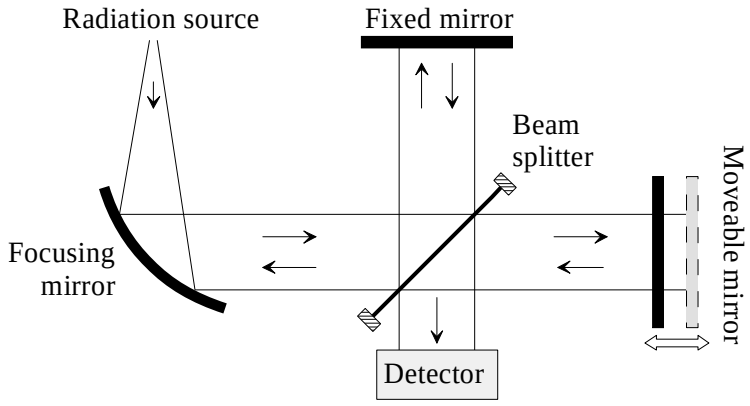


Figure 2.5: Schematic layout of a Michelson interferometer.

The coherent part of the radiation, which contains all the information about the longitudinal properties, can be used to measure the bunch length by means of autocorrelation or spectral analysis techniques. One of the most used techniques to measure the

form factor spectra is the Michelson interferometer, whose schematic layout is shown in figure 2.5.

It consists of a beam splitter (usually made of Mylar) that will split the radiation into two rays directed towards the two mirror arms. These two rays are reflected from the mirrors and recombined, at the beam splitter, and sent into the detector. By moving one of the mirrors we obtain the interferogram, that is the variation of intensity (at the detector) as a function of the optical path difference. The bunch length can be deduced from this interferogram, but since the phase of the signal is not measured, only symmetric distribution can be obtained. Some developments have been made to measure the bunch asymmetry using this type of techniques [33, 34], but these methods demand the measurement of a very wide frequency range and they make assumptions on the behaviour of the signal at frequencies that are not covered by the measurement device.

## 2.7 Microwave Spectroscopy

Microwave spectroscopy is based on the analysis of the RF spectrum of the electron bunch. Different methods have been proposed to couple the field radiated by the bunch into a transmission line that will bring the signal to the detection system, see figure 2.6.

In 2.6 (a) the bunch passes by a ceramic gap in the vacuum chamber, its field radiates from the gap into a cavity and then into a waveguide leading to a detector [35, 36]. The cavity resonates at a fixed frequency and the signal can be detected by using either a diode detector or a bolometer. Several (and different) resonance boxes can be installed giving the possibility to measure the amplitude at several frequencies.

Case 2.6 (b) shows an antenna pick-up [37–39], usually working also at a fixed frequency. The signal can be transported by a coaxial cable or a waveguide depending on the frequency range of the excited signal. It is a system similar to case (a).

These two systems measure the signal at fixed frequencies so that only a few points of the frequency spectrum can be obtained. The calibration of the systems is difficult and usually requires the use of alternative methods for cross checking. In any case, it is a very fast way of monitoring the bunch length, any change in the bunch length is immediately detected.

The next two cases, 2.6 (c) and (d), allow the exploration of a broad bandwidth of the electron RF field spectrum [40, 41]. In this way a knowledge of the frequency content of the signal is possible and allows the use of frequency domain spectroscopy (using a Michelson interferometer for example) as well as time domain analysis, the methods

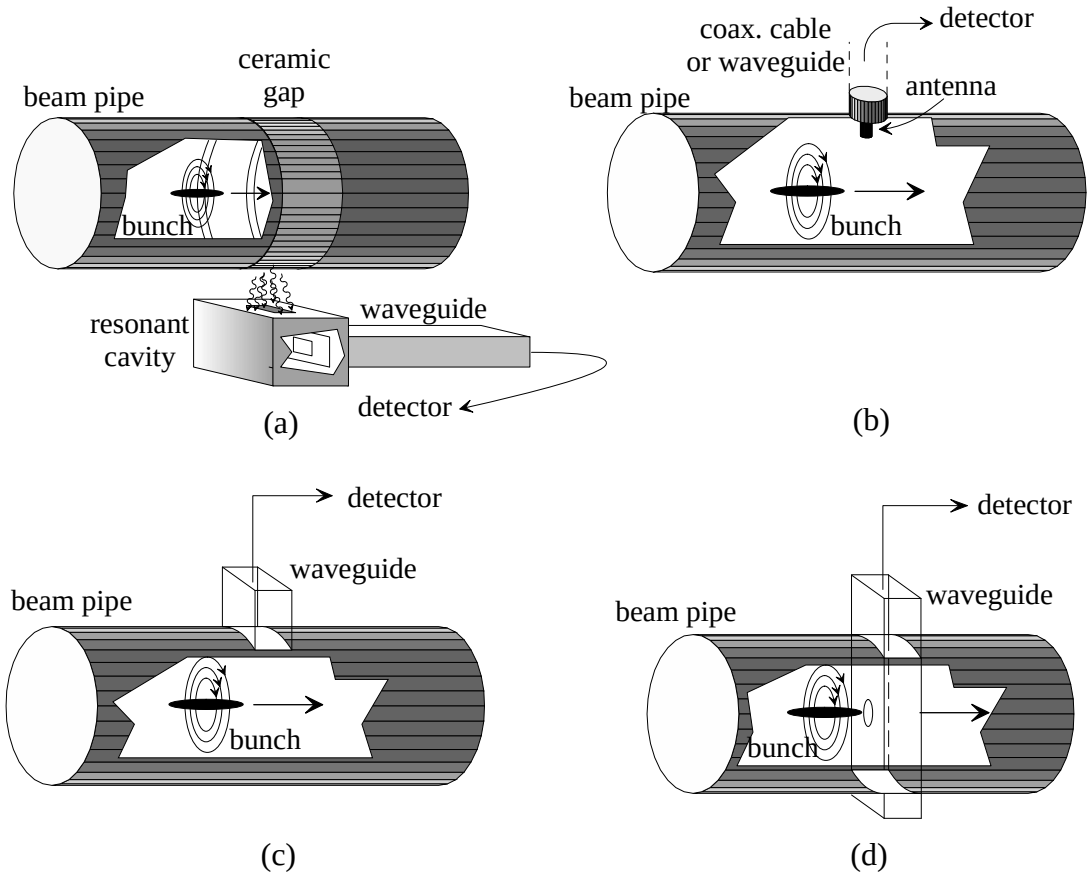


Figure 2.6: Different set-ups for coupling the electron bunch field.

used depends on the requirements. In case (c) the time evolution of the electric field launched in the waveguide is directly related to the electric field of the bunch at the beam pipe wall, therefore it carries the information about the electron bunch shape. In case (d) the electron beam couples energy into the waveguide mode when the waveguide mode oscillation decelerates the electrons, hence this method has a non-negligible effect on the beam; and while the transmission of the waveguide imposes a low frequency limit on the transmitted signal, the transit time, the time required for the electron to cross the waveguide, imposes a high-frequency limit as well.

Methods (b) and (c) are non-destructive and produce a negligible disturbance in the beam, in cases (a) and (d) the coupling geometry can be disturbing, especially in the case of a train of bunches due, to excitation of wakefields.

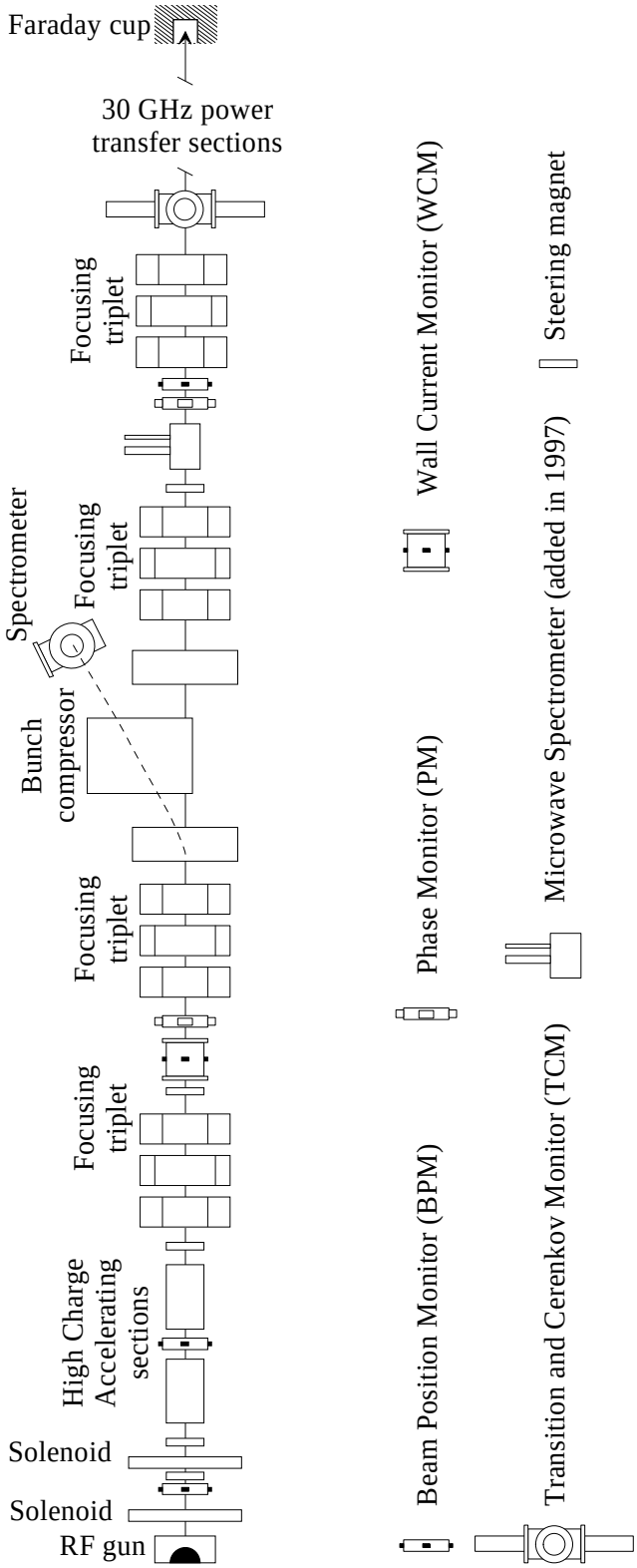


Figure 2.7: Instrumentation in the CTF.

## 2.8 Measure of the bunch length in the CTF

The electron bunch distribution in CTF is usually measured using a streak camera that analyses the light coming from transition and Cerenkov converters (TCM) installed in the CTF line [21]. See figure 2.7 on page 20 for a more detailed layout of the CTF drive beam where it is shown the position of the instrumentation to control and measure the beam properties.

A TCM is composed of a piece of vacuum pipe, an aluminium foil (as transition radiator) and a thin sapphire layer (as Cerenkov radiator) and a pneumatic motor to move the radiators in and out the beam trajectory.

The sapphire sheet has a thickness of 0.3 mm and is tilted by $65.5^o$ with respect to the horizontal plane, in this way the radiation is directed in a direction perpendicular to the electron beam. The aluminium foil is 0.5 mm thick and is tilted at an angle of $45^o$, to produce radiation in a direction perpendicular to the electron beam.

The radiation produced in the TCM is then transported, using mirrors and focusing lenses, to the streak camera room, which is outside the CTF installation hall to avoid radiation damage. The transport system introduces time and transverse dispersion in the light pulse. Several effects account for this dispersion, the chromatic aberration of the lenses, the image distortion of a non-zero size source image, the defects in the lens angular positions, the chromatic dispersion of air. All these effects lead to a time dispersion of 2 ps (rms) and a transverse dispersion of 70 $\mu$m.

The streak camera installed in the CTF is a RGM-SC1 model with an amplifier RAGM2 and a CCD camera KRCCD, everything provided by the ARP company. The overall system is believed to have a resolution of about 2 ps rms for the type of radiation in use in CTF (a better resolution can be achieved for a monochromatic laser beam).

## 2.9 Design of the New Bunch Length Monitor for the CTF

One of the main objectives of CTF is to test and study the feasibility of power transmission at 30 GHz from the drive beam to the main beam. For an efficient power generation in the drive beam short bunches are needed, the fwhm length should be less than 5 ps (0.6 mm). In order to obtain this short bunches a bunch compressor was built and installed in 1995 [16], it was designed to obtain bunch-lengths below 1 ps.

In the previous section is was shown that the resolution of the streak camera (the only method available in the CTF to measure the bunch length) was 4 ps, therefore, with

this set-up it is not possible to test the performance of the compressor and to know the length of the bunches within the required precision for the experiments. Furthermore, this method was highly disturbing for the beam.

According to the study of the state of the art of bunch length measurements and the CTF requirements, it was concluded at this point to develop a new bunch length monitor (BLM) with the conditions of being non-invasive and having a resolution of the order of 1 ps (rms). It has been shown, in this chapter, that all known methods except the microwave spectroscopy are destructive and some of them are only suitable for low beam charges. Therefore, the development of the new BLM will be based on the microwave spectroscopy technique.

# Chapter 3

# Design of a Millimetre-Wave Bunch Length Monitor

The Bunch Length Monitor (BLM) has been designed to measure the beam frequency spectrum from which the bunch length can be deduced. For the bunch lengths in use in CTF the relevant frequency range is above 25 GHz (12 mm wavelength), and the shorter the bunches the higher the frequencies to inspect.

In order to study the beam spectrum, a rectangular waveguide is coupled to the beam pipe (a so called rectangular RF pick-up). The bunch travelling in the beam pipe will excite a signal in the waveguide that carries the information about the bunch shape. A computer code, MAFIA [42], is used to compute the signal excited in the waveguide. That signal travels in the waveguide until it reaches the detection system. The transmission in the waveguide is affected by dispersion and attenuation. Dispersion is due to the fact that the group velocity is frequency dependent, different frequencies travel with different velocities, thus every frequency will arrive at a different time to the detector. Attenuation is caused by the finite conductivity of the waveguide walls.

The detection system has to be able to measure the frequency spectrum of the signal. Several systems, designed for this purpose, are discussed and a description of the design of special high-pass filters used in these systems is also given.

## 3.1 Beam spectrum

The frequency spectrum of a bunch contains all the information about the bunch shape and length, however, to determine the shape it would be necessary to measure the amplitude and phase for all frequencies (or at least in a wide range). If no information about

the phase is available and only positive frequencies are measured then only symmetric distributions can be obtained due to the fact that the inverse Fourier transform of a even real function is another even real function. Furthermore, for frequencies not too far from zero, all bunch distributions have a similar frequency spectrum so that the spectrum can be assumed to be parabolic. That comes from a second order development of the Fourier transform. Let us expand $\exp(-j\omega t)$ in a Taylor series using the integral form of the Fourier transform,

$$F(\omega) = \int_{-\infty}^{\infty} f(t)e^{-j\omega t}dt \approx \int_{-\infty}^{\infty} f(t)dt + j\int_{-\infty}^{\infty} \omega t f(t)dt - \frac{1}{2}\int_{-\infty}^{\infty} (\omega t)^2 f(t)dt \ldots \quad (3.1)$$

Since the measurement system does not distinguish between positive and negative frequencies, the signal that is measured is a real even function, and taking into account

$$F(\omega) \text{ real even} \Leftrightarrow f(t) \text{ real even} \quad (3.2)$$

the function $f(t)$ is also real and even and then the imaginary part of Equation (3.1) vanishes. As a result, we obtain

$$F(\omega) = \int_{-\infty}^{\infty} f(t)e^{-j\omega t}dt \approx Q\left(1 - \frac{\omega^2\sigma^2}{2}\right) + O(\omega^4) \quad (3.3)$$

where $Q$ is the charge of the bunch and $\sigma$ is the second momentum of $f(t)$,

$$\sigma^2 = \int t^2 f(t)dt \quad (3.4)$$

In Figure 3.1 several bunch distributions and their Fourier transforms are plotted, the corresponding analytical functions are listed in Table 3.1.

| | Bunch distribution | Fourier transform | rms |
|---|---|---|---|
| Square | $f(t) = \begin{cases} \frac{1}{\text{fwhm}} & \text{if } \lvert t\rvert \le \frac{\text{fwhm}}{2} \\ 0 & \text{otherwise} \end{cases}$ | $F(\omega) = \frac{\sin(0.5\,\text{fwhm}\,\omega)}{0.5\,\text{fwhm}\,\omega}$ | $\sigma = \frac{\text{fwhm}}{\sqrt{12}}$ |
| Triangular | $f(t) = \begin{cases} \frac{1}{\text{fwhm}}\left(1 - \frac{\lvert t\rvert}{\text{fwhm}}\right) & \text{if } \lvert t\rvert \le \text{fwhm} \\ 0 & \text{otherwise} \end{cases}$ | $F(\omega) = \left(\frac{\sin(0.5\,\text{fwhm}\,\omega)}{0.5\,\text{fwhm}\,\omega}\right)^2$ | $\sigma = \frac{\text{fwhm}}{\sqrt{6}}$ |
| Gaussian | $f(t) = \frac{1}{\sqrt{2\pi}\,\sigma}\exp(-\frac{t^2}{2\sigma^2})$ | $F(\omega) = \exp(-0.5\,\omega^2\,\sigma^2)$ | $\sigma = \frac{\text{fwhm}}{\sqrt{8\ln 2}}$ |

Table 3.1: Some possible bunch distributions and their Fourier transforms.

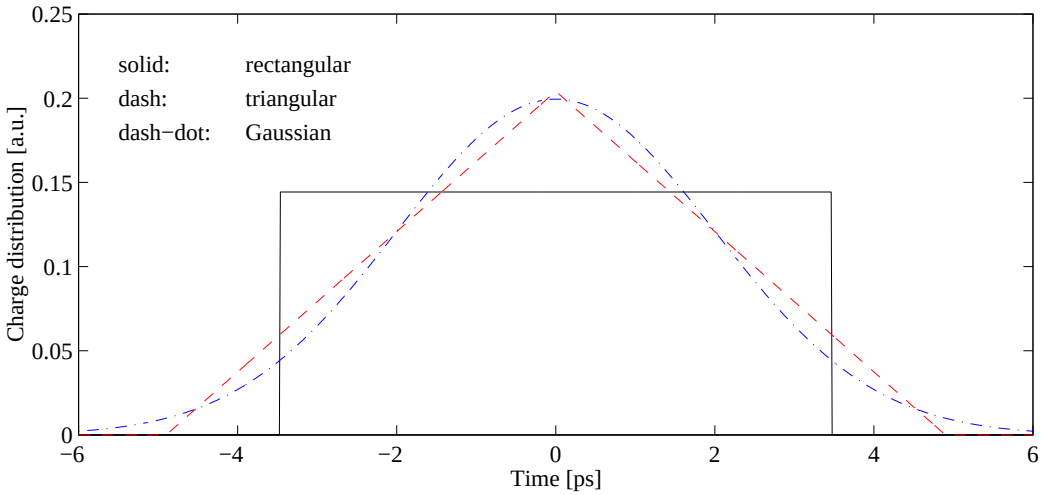


(a) Different charge distributions.

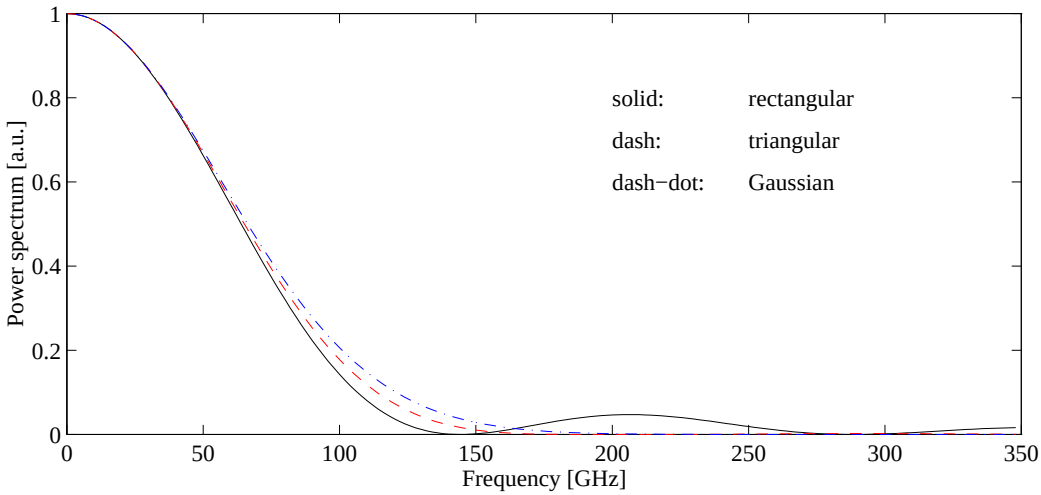


(b) The corresponding power spectrum.

Figure 3.1: Several bunch distributions and their power spectrum.

For any given distribution the term fwhm denotes the full width at half maximum while $\sigma$ is the rms of the distribution. The relation between these two quantities depends on the type of distribution (e.g. for a gaussian function fwhm$= \sqrt{8\ln 2}\,\sigma$ while for a triangular function fwhm$= \sqrt{6}\,\sigma$). All the distributions plotted have the same $\sigma$ (=2 ps) and it is clearly seen that is difficult to distinguish one distribution from another at low frequencies. The BLM measures two frequency ranges, 26.5–40 GHz and 60–90 GHz, in both ranges it is still valid to assume a gaussian or a parabolic distribution.

In order to see the effect of the bunch length on the bunch distribution in Figure 3.2 are plotted the Gaussian power spectra for different values of $\sigma$, the shorter the bunch the larger the amplitude at high frequencies.

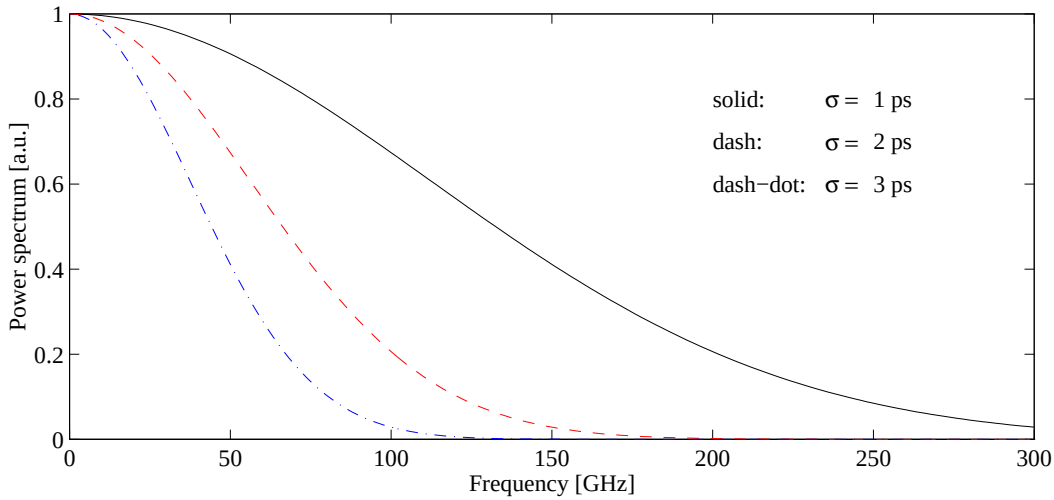


Figure 3.2: Power spectrum for Gaussian bunches of different length.

Figure 3.3 shows the layout of the Bunch Length Monitor (BLM). As the bunch travels by the rectangular RF pick-up, its electromagnetic field induces a field in the waveguide that is then guided to a detector for analysis.

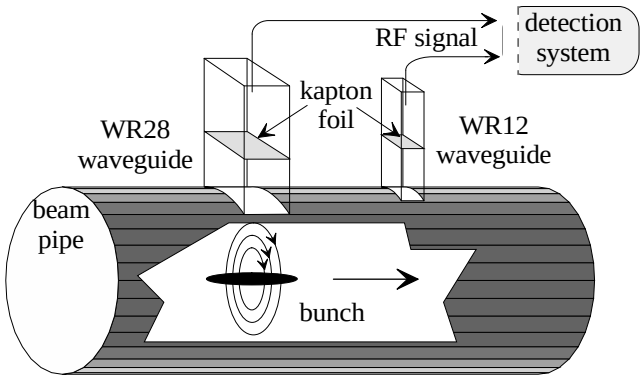


Figure 3.3: Layout of the monitor.

The field induced in the waveguide carries all the information of the bunch spectrum ($BS(\omega)$), but the signal that is detected ($SD(\omega)$) contains also the response function ($RF(\omega)$) of the whole system, hence in order to obtain the bunch spectrum the response function has to be known,

$$SD(\omega) = BS(\omega)RF(\omega) \qquad \Longrightarrow \qquad BS(\omega) = SD(\omega)RF^{-1}(\omega) \tag{3.5}$$

The response function of the system is composed of the different responses of the different elements, such as the coupling hole, the waveguide and the detector itself.

Different approaches can be followed to obtain the frequency response of the different components, theoretically, by direct measurement (e.g. with a network or spectrum analyser) or using special techniques to analyse the data.

## 3.2 Field Induced by the Electron Bunch

This section outlines the process to obtain the fields induced by a bunch in the waveguide and the corresponding frequency spectrum, that is the frequency response of the rectangular pick-up. The frequency spectrum of a train of bunches is also shown.

### 3.2.1 Fields of a Bunch of Charged Particles

To obtain the electromagnetic fields created by a bunch of charged particle it is easier to first write down the field in a co-moving frame and use then the Lorentz transformations to obtain the fields in the laboratory frame.

The Lorentz transformation relate the fields in the frame were the particles are at rest to the fields in the laboratory frame. The component of the electric field parallel to the bunch velocity remains unchanged,

$$\vec{E}_{\parallel} = \vec{E}'_{\parallel} \tag{3.6}$$

while for the transverse components the transformation is:

$$\vec{E}_{\perp} = \gamma \vec{E}'_{\perp} \qquad \text{and} \qquad \vec{H}_{\perp} = \frac{\vec{1}}{\mu_0 c^2} \vec{v} \times \vec{E}_{\perp} \tag{3.7}$$

where the primed quantities are in the rest frame of the bunch, $\vec{v}$ is the velocity of the bunch and $c$ the speed of light. For an ultra-relativistic bunch, $v \simeq c$, the length in the co-moving frame is $\gamma$ times larger than in the laboratory frame, hence the longitudinal charge density is $\gamma$ times smaller and the component $E_{\parallel}$ is reduced by a factor $\gamma$. As the perpendicular component of the electric field in the laboratory is gamma times the field in the co-moving frame this component is not reduced in amplitude, therefore, for ultra-relativistic bunches we are only interested in the transverse components of the electromagnetic field.

Let us consider now an electron bunch of N particles with longitudinal charge distribution $\Lambda(z)$ following a straight trajectory in free space. The transverse fields in the laboratory moving frame will be (in cylindrical coordinates) [43, 44]

$$E_r(r,z) = \frac{eN}{2\pi\varepsilon_0 r}\Lambda(z) \qquad \text{and} \qquad H_\theta(r,z) = \frac{eN\nu}{2\pi r}\Lambda(z) \qquad r \geq \text{beam radius} \tag{3.8}$$

for a round uniform beam or

$$E_r(r,z) = \frac{eN}{2\pi\varepsilon_0 r}\left(1 - e^{-\frac{r^2}{2\sigma^2}}\right)\Lambda(z) \quad \text{and} \quad H_\theta(r,z) = \frac{eN\nu}{2\pi r}\left(1 - e^{-\frac{r^2}{2\sigma^2}}\right)\Lambda(z) \tag{3.9}$$

for a round gaussian beam. From the above equations we can derive the fields at the beam pipe wall at z=0 for a beam travelling coaxially [36, 40]

$$E_r(r,t) = \frac{eN}{2\pi\varepsilon_0 R}\Lambda(t) \qquad \text{and} \qquad H_\theta(r,t) = \frac{eN\nu}{2\pi R}\Lambda(t) \tag{3.10}$$

The bunch is very often supposed to be Gaussian in the longitudinal direction,

$$\Lambda(t) = \frac{1}{\sqrt{2\pi}\sigma_z} e^{-\frac{t^2}{2\sigma_t^2}} \tag{3.11}$$

where $\sigma_t$ is the bunch length in time units, $\sigma_z = \nu\sigma_t$.

The frequency spectrum is found by Fourier transforming Equation 3.10. For the magnetic field,

$$\widetilde{H}(r,\omega) = \int_{-\infty}^{\infty} H(r,t)e^{-j\omega t}dt = \frac{eN\nu}{2\pi R}\widetilde{\Lambda}(\omega) \tag{3.12}$$

where $\widetilde{\Lambda}(\omega)$ is the Fourier transform of $\Lambda(t)$, for a gaussian distribution:

$$\Lambda(\omega) = \frac{1}{\nu} e^{-\frac{t^2}{2\sigma_t^2}} \tag{3.13}$$

### 3.2.2 Fields induced in the waveguide

The frequency response of the rectangular pick-up is found by applying the field equivalence principles, due to Schelkunoff, across the aperture formed by the waveguide entrance coupled to the beam pipe [45],

$$\hat{n} \times \vec{H}_{wg} = \vec{J}_c = \hat{n} \times \vec{H}_{bunch} \tag{3.14}$$

where $\vec{J}_c$ is the current induced on the walls. According to the previous equation the field launched in the waveguide will have the same temporal evolution than the field produced by the bunch.

The actual field induced in the waveguide can not be calculated analytically as it is a sum of a large number of modes and numerical methods has to be used to solve the resulting equations. However there is a computer program, MAFIA, than can calculate the amplitude of the modes by solving the Maxwell's equation numerically. The results obtained with this program are shown in the next section.

### 3.2.3 A Train of Bunches

CTF can operate in single bunch mode or with a train of bunches, therefore it is necessary to know the frequency spectrum of a train of bunches as well as that of a single bunch.

The field distribution in time of an infinite train of bunches having all of them the same distribution and a constant period $\tau$ is the convolution of the field for one single bunch with an impulse train,

$$\vec{H}_{train}(r,t) = \vec{H}_{bunch}(r,t) \otimes \sum_{i=-\infty}^{\infty} \delta(t - i\tau) \tag{3.15}$$

Taking into account that the fourier transform of the convolution of two functions is the product of the Fourier transform for each function,

$$\mathfrak{F}(f_1(t) \otimes f_2(t)) = \mathfrak{F}(f_1(t)) \cdot \mathfrak{F}(f_2(t)) \tag{3.16}$$

the frequency spectrum is found to be also a sum of pulses

$$\vec{H}_{train} = \widetilde{H}(r,\omega) \sum_{i=0}^{n} e^{-j\omega i\tau} \tag{3.17}$$

This effect is best illustrated graphically, Figure 3.4 shows a train of 5 identical gaussian bunches (with the same charge and the same length $\sigma = 2$ ps) separated by a distance $\delta t$ = 30 ps while Figure 3.5 shows the corresponding frequency spectrum. The frequency spectrum of a train of bunches is a line spectrum which amplitudes decrease with increasing frequency. The distance between these lines is given by $\delta\nu = 1/\delta t$ (= 33.3 GHz in this example). The envelope of the line spectrum, shown with a dashed line, is that of a single bunch with the same $\sigma$ that the individual bunches of the train, in this case a gaussian function with $\sigma_f$ = 50 GHz (= $1/\sigma$).

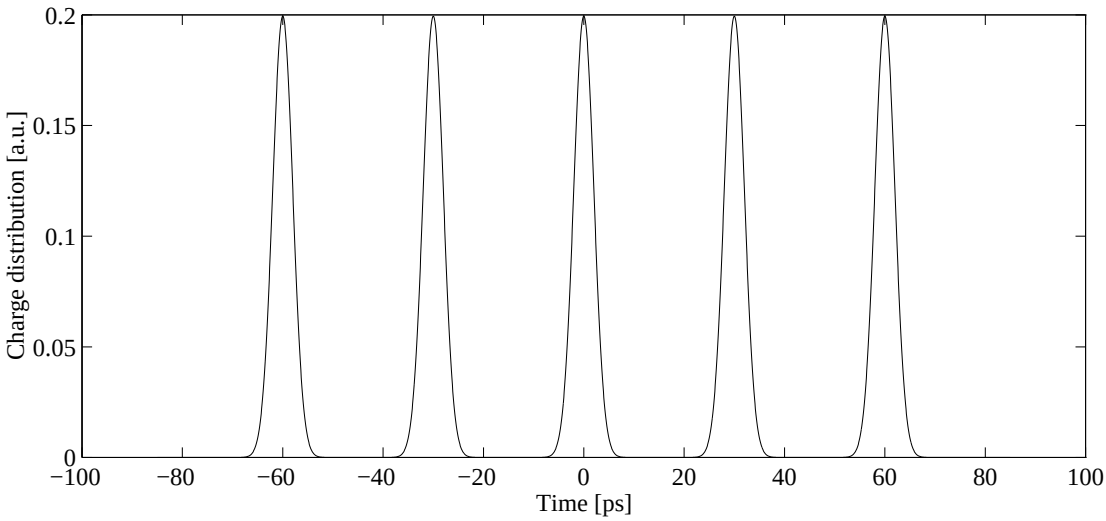


Figure 3.4: A train of 5 bunches.

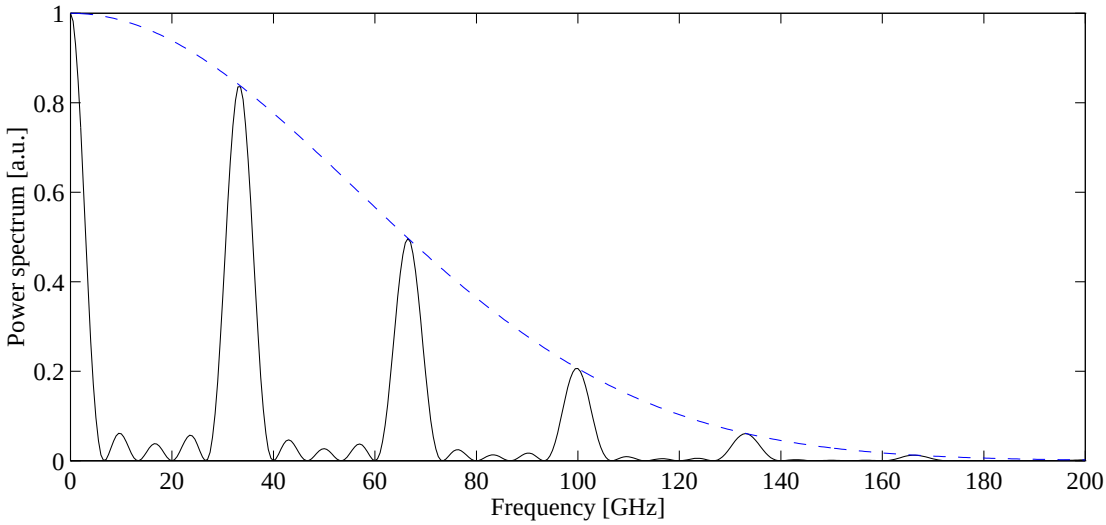


Figure 3.5: Frequency spectrum of a train of 5 bunches.

## 3.3 Transmission through Waveguides

The following introduction to transmission in waveguides is derived from [45] and [46]. The type of waveguide considered is a hollow conducting cylindrical tube (i.e. with only one boundary) with a cross section which is uniform along the direction of propagation, as shown in Figure 3.6. The waveguide is assumed to be either empty or filled with an homogeneous isotropic medium with permittivity and permeability parameters $\varepsilon$ and $\mu$ and to be infinitely long.

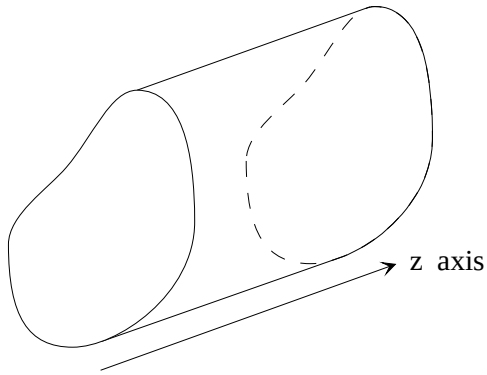


Figure 3.6: Cilindrical waveguide.

The determination of the electromagnetic fields within that region is obtained by solving the Maxwell's equations with the corresponding boundary conditions (by choosing the right coordinate system). It is found that the solutions can be divided into two sets of solutions or modes. For one set of modes, no axial magnetic field component exists. These modes are called "electric type" (E modes) or "transverse magnetic", that is, TM modes. The other set of solutions have no axial component of electric field and are referred to as "magnetic type" (H modes) or "transverse electric", that is TE modes.

### 3.3.1 General Properties

The electric and magnetic field in the interior of the waveguide are solutions of the homogeneous vector Helmholtz equation, i.e.,

$$\nabla^2\vec{E} + k_0^2\vec{E} = 0 \qquad \nabla^2\vec{H} + k_0^2\vec{H} = 0 \tag{3.18}$$

where $k_0^2 = \omega^2\mu_0\varepsilon_0$. The type of solution is that of a wave that propagates along the z axis. Since the Helmholtz equation is separable for this kind of boundary conditions, it is possible to find solutions of the form $f(z)\,g(x,y)$. Being z the axis of propagation and

x and y suitable transverse coordinates. The z dependence can be assumed to be of the type $e^{\pm\Gamma z}$ and the time dependence is $e^{j\omega t}$.

In order to simplify Maxwell's equations all the fields are decomposed into transverse and axial components and after separating out the z dependence (time dependence suppressed)

$$\begin{aligned}\vec{E}(x,y,z) &= \vec{E}_t(x,y,z) + \vec{E}_z(x,y,z) = \vec{e}(x,y)e^{\pm\Gamma z} + \vec{e}_z(x,y)e^{\pm\Gamma z} \\ \vec{H}(x,y,z) &= \vec{H}_t(x,y,z) + \vec{H}_z(x,y,z) = \vec{h}(x,y)e^{\pm\Gamma z} + \vec{h}_z(x,y)e^{\pm\Gamma z}\end{aligned} \tag{3.19}$$

where $\vec{E}_t$, $\vec{H}_t$ are the transverse components, and $\vec{E}_z$, $\vec{H}_z$ are the axial components.

The Maxwell's equations using the above decomposition and $\nabla = \nabla_t + \nabla_z = \nabla_t \pm \Gamma\hat{a}_z$ for a z dependence $e^{\pm\Gamma z}$ result in

$$\begin{aligned} \nabla_t \times \vec{e} &= j\omega\varepsilon_0\vec{h}_z & \nabla_t \times \vec{h} &= j\omega\varepsilon_0\vec{e}_z \\ \hat{a}_z \times \nabla_t e_z \pm \Gamma\hat{a}_z \times \vec{e} &= j\omega\varepsilon_0\vec{h}_z & \hat{a}_z \times \nabla_t h_z \pm \Gamma\hat{a}_z \times \vec{h} &= -j\omega\varepsilon_0\vec{e}_z \\ \nabla_t\vec{h} &= \pm\Gamma h_z & \nabla_t\vec{e} &= \pm\Gamma e_z \end{aligned} \tag{3.20}$$

The solutions are classified as follows,

1. Transverse electric (TE) modes. Solutions with $E_z = 0$ but $H_z \neq 0$. All the field components may be derived from the axial component $H_z$ of the magnetic field.

2. Transverse magnetic (TM) modes. Solutions with $H_z = 0$ but $E_z \neq 0$. The field components may be derived from $H_z$.

**TE modes**

Separating Equation 3.18 into transverse and axial parts yields

$$\nabla_t^2 h_z(x,y) + k_c^2 h_z(x,y) = 0 \tag{3.21}$$

$$\nabla_t^2\vec{h} + k_c^2\vec{h} = 0 \tag{3.22}$$

where $k_c^2 = k_0^2 + \Gamma^2$.

From the Maxwell equation (3.20) to (3.3.1) with $\vec{e}_z = 0$ a solution is obtained for $\vec{h}$ in terms of the transverse component $h_z$

$$\vec{h} = \frac{\pm\Gamma}{k_c^2}\nabla_z h_z \tag{3.23}$$

and $\vec{e}$ in terms of $\vec{h}$

$$\vec{e} = \frac{k_0}{\pm\Gamma}Z_0\hat{a}_z \times \vec{h} \tag{3.24}$$

The factor $jZ_0k_0/\Gamma$ is called the wave impedance of TE modes, with $Z_0 = \sqrt{\mu_0/\varepsilon_0}$ being the intrinsic impedance of free space. For a propagating mode, $\Gamma$ is imaginary and will be taken as $j\beta$. The wave impedance $Z_h = k_0/\beta Z_0$ is now real. For a non-propagating mode, the wave impedance is imaginary and inductive.

The boundary conditions determine the allowed values for $k_c$, thus the propagation constant $\Gamma$ will depend on the waveguide geometry. The parameter $k_c$ is called the cutoff wave number, since it determines the wavelength at which free propagation ceases ($\Gamma = 0$). This occurs when $\lambda_0$ is so that $k_c = k_0$ for a given mode, hence, the free space cutoff wavelength is given by

$$\lambda_c = \frac{2\pi}{k_c} \tag{3.25}$$

Once the cutoff wavelength has been determined for a particular propagating mode, the value of $\beta$ and the guide wavelength may be found. The guide wavelength $\lambda_g$ is the distance the wave must propagate to undergo a phase change of $2\pi$ radians, hence

$$\lambda_g = \frac{2\pi}{\beta} = \frac{\lambda_0}{[1-(\lambda_0/\lambda_c)^2]^{1/2}} \left(\frac{\mu_0\varepsilon_0}{\mu\varepsilon}\right)^{1/2} \tag{3.26}$$

For $\lambda_0 < \lambda_c$ there is free propagation of the mode, at $\lambda_0 = \lambda_c$ free propagation stops and for $\lambda_0 > \lambda_c$ the mode is exponentially damped with distance along the guide (evanescent mode).

### TM Modes

The TM (or E) modes have $\vec{h}_z = 0$ but $\vec{e}_z \neq 0$. These modes may be considered the dual of the TE modes by exchanging the roles of the electric and magnetic fields. Thus, similar equation are obtained for fields

$$\nabla_t^2 e_z(x,y) + k_c^2 e_z(x,y) = 0 \tag{3.27}$$

$$\vec{e} = \frac{\pm\Gamma}{k_c^2}\nabla_z e_z \tag{3.28}$$

$$\vec{h} = \pm j\frac{k_0}{\Gamma}Y_0\hat{a}_z \times \vec{e} \tag{3.29}$$

where $Y_0 = Z_0^{-1}$and the wave admittance $Y_e$ for TM modes is given by

$$Y_e = Z_e^{-1} = j\frac{k_0}{\Gamma}Y_0 \tag{3.30}$$

and $Z_e Z_h = Z_0^2$.

In analogy to TE modes, an infinite number of values for $k_c^2$ exists given some boundary conditions. For $\Gamma = j\beta$, the wave admittance is real, $Y_e = Y_0 k_0/\beta$, while for $\Gamma$ real (non-propagating mode) it is imaginary and capacitive.

### 3.3.2 Power, Energy and Attenuation

In a waveguide with perfectly conducting walls, each mode propagates power along the guide independently of the presence of other modes. The time-average power flow for a single propagating TE mode is given by

$$P = \frac{1}{2}\mathrm{Re}\iint_S \vec{E}\times\vec{H}^*\,\hat{a}_z\,ds \quad = \quad \frac{Z_h}{2}\iint_S \vec{h}\cdot\vec{h}^*\,ds \quad = \quad \frac{Y_h}{2}\iint_S \vec{e}\cdot\vec{e}^*\,ds \tag{3.31}$$

and for a single TM mode,

$$P = \frac{Z_e}{2}\iint_S \vec{h}\cdot\vec{h}^*\,ds \quad = \quad \frac{Y_e}{2}\iint_S \vec{e}\cdot\vec{e}^*\,ds \tag{3.32}$$

It can be proven that that for a propagating mode, the time-average electric and magnetic energies are equal, e.g. for a TE mode

$$W_e = \frac{1}{4}\varepsilon_0 Z_h^2 \iint_S \vec{h}\cdot\vec{h}^* = W_m \tag{3.33}$$

The power flowing along the waveguide is equal to the product of the total energy per unit length and the velocity, $v_g$, of energy propagation $P = 2W_e v_g$, and from here

$$v_g = \frac{\beta}{k_0}v_c = \frac{\lambda_0}{\lambda_c}v_c \tag{3.34}$$

where $v_c = (\mu_0\varepsilon_0)^{-1/2}$.

The phase velocity $v_p$ is given by

$$v_p = \frac{\omega}{\beta} = \frac{k_0}{\beta}v_c \tag{3.35}$$

and it can be easily shown that $v_p v_g = v_c^2$. Equations 3.34 and 3.35 are valid for TM modes as well.

### Attenuation in Waveguides

If the metallic walls of the waveguide have a finite conductivity $\sigma$, they exhibit a surface impedance given by

$$Z_m = \frac{1+j}{\sigma \delta_s} \tag{3.36}$$

where $\delta_s = (2/\omega\mu\sigma)^{1/2}$ is the skin depth. The finite conductivity results in a power loss, $P_l$, in the waveguide walls. Since loss is present the propagating power must decrease according to a factor $e^{-2\alpha z}$, where $\alpha$ is the attenuation, for a power $P_0$ at the beginning of the line the power at a distance $z$ is $P = P_0 e^{-2\alpha z}$. The rate of decrease of power along the line equals the power loss

$$-\frac{\partial P}{\partial z} = P_l = 2\alpha P_0 e^{-2\alpha z} = 2\alpha P \tag{3.37}$$

Hence the attenuation $\alpha$ arising from conductor loss is given by,

$$\alpha = \frac{P_l}{2P} = \frac{R_m \oint_C \vec{J} \cdot \vec{J}^* \, dl}{2Z \int \vec{H} \cdot \vec{H}^* \, dS} \tag{3.38}$$

where $R_m = (\sigma\delta_s)^{-1}$

## 3.3.3 Rectangular Waveguide

This is the most commonly used waveguide, the cross section is illustrated in Figure 3.7.

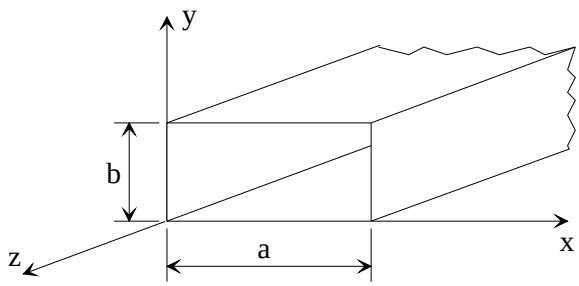


Figure 3.7: Rectangular waveguide.

Once the equations for the magnetic and electric field inside the waveguide are solved with the proper boundary conditions a double infinity set of possible solutions is found for both TE and TM waves. However, only a finite number of modes propagates in a given frequency range, and in particular there is a range were only the first mode, the

$TE_{10}$, propagates. The modes may be labelled by two identifying integer subscripts $n$ and $m$. Each mode has associated a characteristic cutoff frequency $\nu_{c,nm}$ below which the mode does not propagate. Once $\nu_{c,nm}$ has been determined the propagation factor is given by

$$\beta = \sqrt{k_0^2 - k_c^2} \tag{3.39}$$

where $k_0 = \omega\sqrt{\mu_0\varepsilon_0}$ and $k_c = 2\pi\nu_c\sqrt{\mu_0\varepsilon_0}$. Since the cutoff frequency differs for different modes, there is always a lower band of frequencies for which only one mode propagates (unless $\nu_c$ has the same value for two or more modes).

The propagation constant $\beta$ is function of frequency,

$$\beta = \frac{1}{c}\sqrt{\omega^2 - \omega_c^2} \tag{3.40}$$

any signal consisting of several frequencies is dispersed, or spread out, in both time and space as it propagates along the guide. This dispersion results from the different velocities at which the different frequency components propagate.

**TE modes**

The field components are for $n = 0, 1, 2, \ldots$, $m = 0, 1, 2, \ldots$, $n = m \neq 0$

$$\begin{aligned}
H_z &= A_{nm}\cos\frac{n\pi x}{a}\cos\frac{m\pi y}{b}e^{\mp j\beta_{nm}z} \\
H_x &= \pm j\frac{n\pi\beta_{nm}}{ak_{c,nm}^2}A_{nm}\sin\frac{n\pi x}{a}\cos\frac{m\pi y}{b}e^{\mp j\beta_{nm}z} \\
H_y &= \pm j\frac{m\pi\beta_{nm}}{bk_{c,nm}^2}A_{nm}\cos\frac{n\pi x}{a}\sin\frac{m\pi y}{b}e^{\mp j\beta_{nm}z} \\
E_x &= Z_{h,nm}\,j\frac{m\pi\beta_{nm}}{bk_{c,nm}^2}A_{nm}\cos\frac{n\pi x}{a}\sin\frac{m\pi y}{b}e^{\mp j\beta_{nm}z} \\
E_y &= -Z_{h,nm}\,j\frac{n\pi\beta_{nm}}{ak_{c,nm}^2}A_{nm}\sin\frac{n\pi x}{a}\cos\frac{m\pi y}{b}e^{\mp j\beta_{nm}z}
\end{aligned} \tag{3.41}$$

where the $Z_{h,nm}$ is the wave impedance for the $nm$th TE mode

$$Z_{h,nm} = \frac{k_0}{\beta_{nm}}Z_0 \tag{3.42}$$

The cutoff wave number is given by

$$k_{c,nm} = \left[ \left( \frac{n\pi}{a} \right)^2 + \left( \frac{m\pi}{b} \right)^2 \right]^{1/2} \tag{3.43}$$

and is clearly a function of the guide dimensions only. The propagation constant is given by

$$\beta_{nm} = (k_0^2 - k_{c,nm}^2)^{1/2} = \left[ \left( \frac{2\pi}{\lambda_0} \right)^2 - \left( \frac{n\pi}{a} \right)^2 - \left( \frac{m\pi}{b} \right)^2 \right]^{1/2} \tag{3.44}$$

When $k_0 > k_{c,nm}$, $\beta_{nm}$ is pure real and the mode propagates; when $k_0 < k_{c,nm}$ it is imaginary and the mode decays exponentially. The frequency separating the propagation and no-propagation bands, $\nu_c$, is given by the solution of $k_0 = k_{c,nm}$, that is,

$$\nu_{c,nm} = \frac{c}{2\pi} \left[ \left( \frac{n\pi}{a} \right)^2 + \left( \frac{m\pi}{b} \right)^2 \right]^{1/2} \tag{3.45}$$

where c is the velocity of light.

A typical guide may have $a = 2b$, in which case

$$\nu_{c,nm} = \frac{c}{2a} (n^2 + 4m^2)^{1/2} \tag{3.46}$$

and $\nu_{c,10} = c/2a$, $\nu_{c,01} = c/a$, $\nu_{c,11} = \sqrt{5}c/2a$, etc. Therefore, there is a frequency band

$$\frac{c}{2a} < \nu < \frac{c}{a} \tag{3.47}$$

for which only the $TE_{10}$ mode propagates. This is the dominant mode in rectangular waveguides and the most commonly used in practice.

### Power

Substituting the fields found in the previous section in Equation 3.31, it is found

$$P_{nm} = \frac{|A_{nm}|^2 ab}{2\varepsilon_{on}\varepsilon_{om}} \left( \frac{\beta_{nm}}{k_{c,nm}} \right)^2 Z_{h,nm} \tag{3.48}$$

where $\varepsilon_{on}$ is the Neumann factor, equal to 1 for $n = 0$ and equal to 2 for $m > 0$.

If two modes are present simultaneously, the power is the sum of that contributed by each mode. This is a property of loss-free waveguides due to the orthogonality of the eigenfunctions that describe the transverse variation of the fields.

### Attenuation

There will be a continuous loss of power due to the finite conductivity of the waveguide walls. Consequently the propagation constant becomes a complex quantity, $\Gamma = \alpha + j\beta$, where $\alpha$ is an attenuation constant.

For the dominant mode $TE_{10}$ the attenuation constant is

$$\alpha = \frac{R_m}{ab\beta_{10}k_0Z_0}(2bk_{c,10}^2 + ak_0^2)^2 \ \frac{\mathrm{Np}}{\mathrm{m}} \tag{3.49}$$

To convert attenuation given in nepers to decibels, multiply by 8.686 ($= 20\lg e$).

### TM modes

For TM modes similar solutions to those for the TE modes are found. A summary of the solutions is given in Table 3.2 Friday, May 28, 1999 at 17:46

| | **TE modes** | **TM modes** |
|---|---|---|
| $Z_{nm}$ | $\frac{k_0}{\beta_{nm}}Z_0$ | $\frac{\beta_{nm}}{k_0}Z_0$ |
| $k_{c,nm}$ | $\sqrt{\left(\frac{n\pi}{a}\right)^2 + \left(\frac{m\pi}{b}\right)^2}$ | |
| $\beta_{nm}$ | $\sqrt{k_0^2 - k_{c,nm}^2}$ | |
| $\nu_{c,nm}$ | $\frac{c}{2a}\sqrt{n^2+4m^2}$ | |
| $P_{nm}$ | $\frac{\lvert A_{nm}\rvert^2 ab}{2\varepsilon_{on}\varepsilon_{om}}\left(\frac{\beta_{nm}}{k_{c,nm}}\right)^2 Z_{h,nm}$ | $\frac{\lvert A_{nm}\rvert^2 ab}{2\varepsilon_{on}\varepsilon_{om}}\left(\frac{\beta_{nm}}{k_{c,nm}}\right)^2 Y_{e,nm}$ |
| $\alpha_{nm}$ | $\frac{2R_m}{bZ_0\sqrt{1-k_{c,nm}^2/k_0^2}}\left[\left(1+\frac{b}{a}\right)\frac{k_{c,nm}^2}{k_0^2} + \frac{b}{a}\left(\frac{\varepsilon_{0m}}{2} - \frac{k_{c,nm}^2}{k_0^2}\right)\frac{n^2ab+m^2a^2}{n^2b^2+m^2a^2}\right]$ | $\frac{2R_m}{bZ_0\sqrt{1-k_{c,nm}^2/k_0^2}}\frac{n^2b^3+m^2a^3}{n^2b^2a+m^2a^3}$ |

Table 3.2: Properties of modes in rectangular waveguides.

## 3.4 MAFIA Simulations - Frequency response of the RF pick-up

The frequency response of the RF pick-up was computed with the help of MAFIA. MAFIA is a program package for the computation of electromagnetic fields by solving the Maxwell's equations. The basis of all simulations is the theory of the discrete Maxwell grid equations, the so called Finite Integration Technique [42].

MAFIA can calculate the amplitude of the different modes excited in a small piece of rectangular waveguide connected to the beam pipe in which an electron bunch (with Gaussian charge distribution) is travelling. To solve this problem, in Cartesian coordinates, it is necessary to define mesh steps in each direction, $\Delta x$, $\Delta y$ and $\Delta z$. The time step for integration has to be defined proportional to $\Delta z/c$, where c is the velocity of light. These two parameters, $\Delta z$ and $\Delta t$, are the most important ones, as $\Delta z$ limits the lower wavelength that can be computed with a good accuracy and $\Delta t$ determines the computing time (that can be more than 1 day of CPU time on a IBM-RS6000 for very small time steps).

Several simulation where done for different sizes of the mesh step $\Delta z$ to find a compromise between good accuracy for short wavelengths (high frequencies) and a not too long computing time. The parameters finally chosen for the mesh structure are listed in Table 3.3. The beam pipe radius is 20 mm (that is, the nominal CTF pipe radius).

| | WR28 waveguide (3.56 x 7.11 $mm^2$) | WR12 waveguide (1.549 x 3.099 $mm^2$) |
|---|---|---|
| $\Delta z$ [mm] | 3.560/16 = 0.222 | 1.549/7 = 0.221 |
| $\Delta x = \Delta y$ [mm] | 0.222 | 0.221 |
| Beam pipe length [mm] | 21.360 | 21.686 |
| Waveguide length [mm] | 2.0 | 2.0 |

Table 3.3: Parameter for the MAFIA mesh.

These parameter where chosen so that there is an integer number of mesh steps in each direction. Figures 3.8(a) and 3.8(b) show the geometry used for the simulations with both types of waveguides.

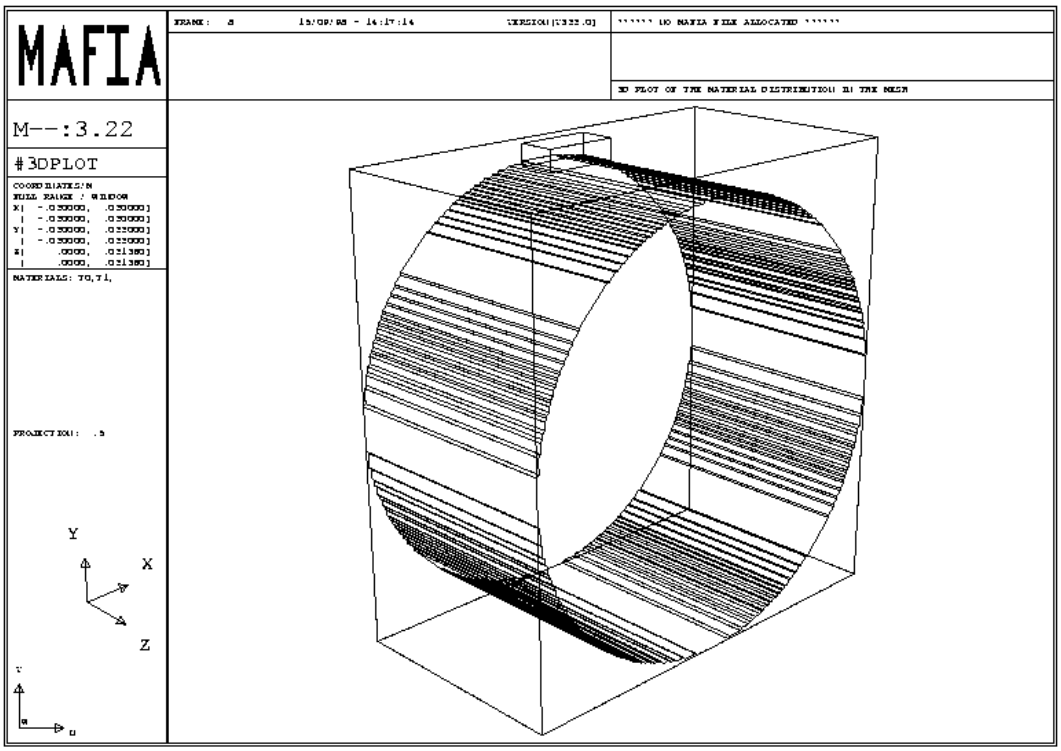


(a) Waveguide: WR28

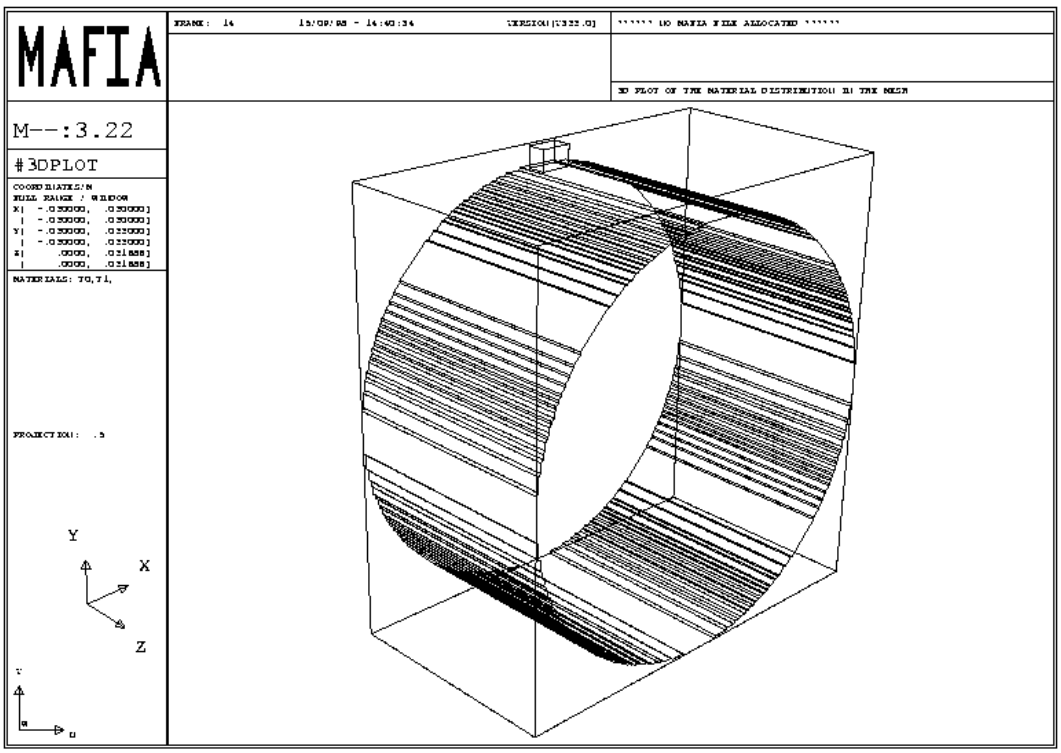


(b) Waveguide: WR12

Figure 3.8: Mesh geometry for the MAFIA simulations.

For these geometries MAFIA will obtain the $TE_{10}$ mode amplitude at the end of the short (2 mm) waveguide coupled to the beam pipe. In fact, other modes are computed but the $TE_{10}$ is the dominant mode and the only one propagating in the frequency range covered by the detection system. If MAFIA could be considered to give an error-free solution, only one simulation for a bunch with a given length would be necessary to obtain the desired frequency response of the system, however, any result obtained with a numerical method using a finite mesh has an associated error. In order to have an estimate of the error carried by MAFIA, several simulations were made for different values of $\sigma$ of the Gaussian bunch. The bunch lengths used were $\sigma$ = 0.25, 0.50, 0.75, 1.00, 1.25, 1.50, 1.75 and 2.00 mm. Figure 3.9 shows the results of two different simulations ($\sigma$ = 0.75 mm and $\sigma$ = 1.25 mm) for both type of waveguides.

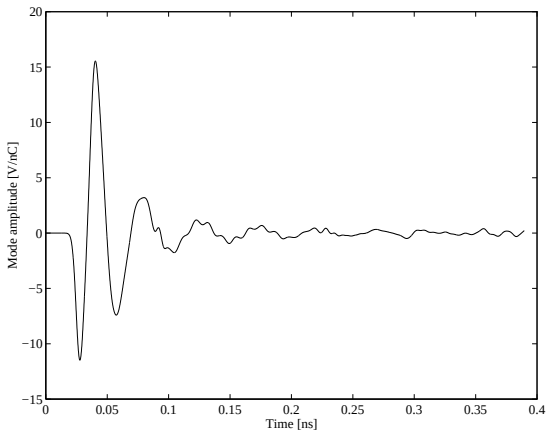


(a) WR28; $\sigma_z = 0.75\ mm$

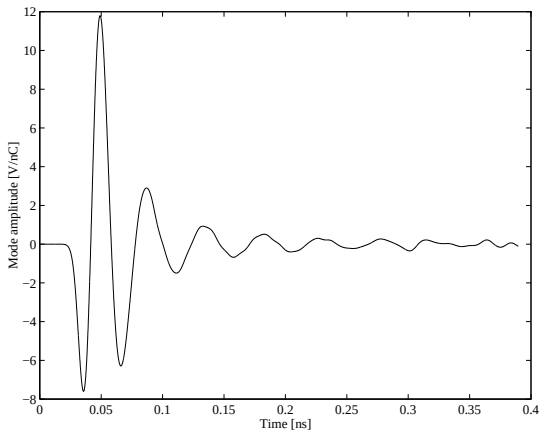


(b) WR28; $\sigma_z = 1.25\ mm$

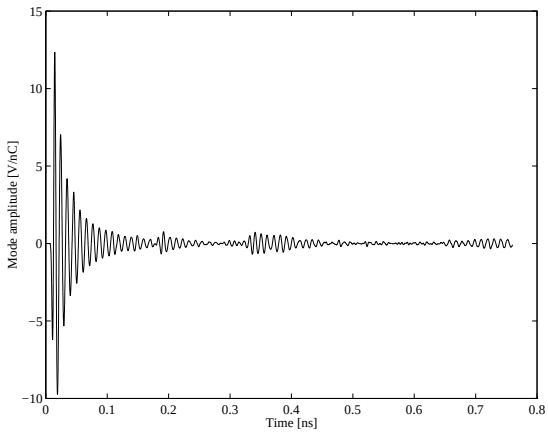


(c) WR12; $\sigma_z = 0.75\ mm$

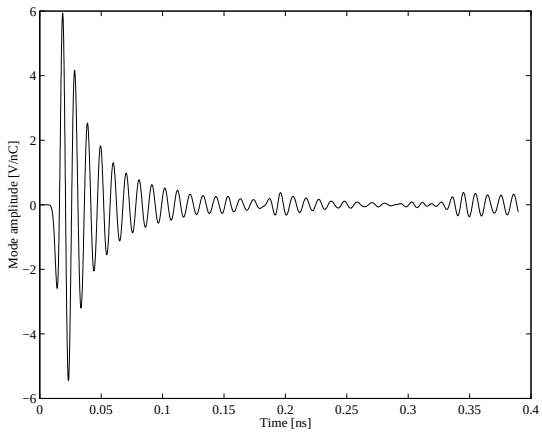


(d) WR12; $\sigma_z = 1.25\ mm$

Figure 3.9: Mode amplitudes.

The Fourier transform of the (time dependent) mode amplitude will give the frequency spectrum of the excited mode. Therefore, a FFT (Fast Fourier Transform) is applied to all the results given by MAFIA, a different frequency spectrum is obtained for each bunch length, as shown in Figure 3.10 for the previous cases.

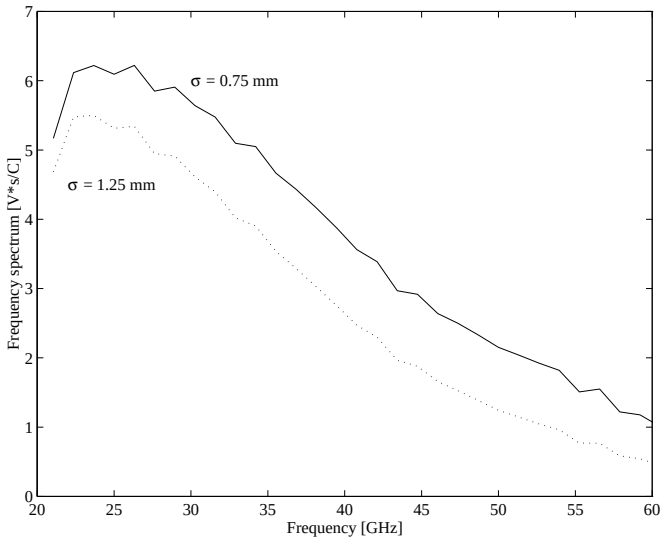


(a) WR28

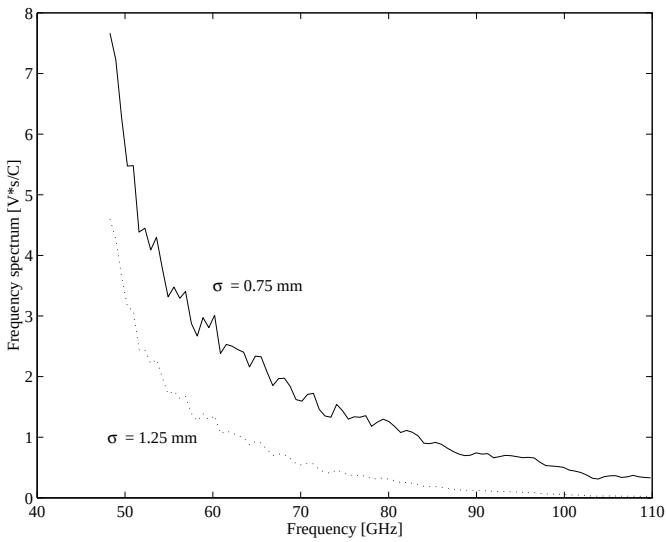


(b) WR12

Figure 3.10: Frequency spectra for two different bunch lengths.

The frequency spectrum of the electron bunch is also Gaussian, (the Fourier transform of a Gaussian function is another Gaussian function), and the signal in the waveguide is proportional to the bunch spectrum. Therefore, the response function of the pick-up can be obtained by dividing each result obtained from the FFT by a gaussian

distribution with the corresponding σ (since each simulation was made with a different bunch length).

$$pu(\omega) = \frac{FFT\{\text{Mode amplitude}(t)\}(\omega)}{\text{Bunch shape}(\omega)} \quad \left[\frac{V}{Hz}\right]$$

The frequency response of the pick-up is then obtained by averaging over the different simulations. The result is shown is Figure 3.11 and the corresponding standard deviation in Figure 3.12, this standard deviation gives an estimate of the error contained in the numerical result. It can be seen that the value of standard deviation is very small except for very high frequencies (>90 GHz), that are, nevertheless, above our measurement range.

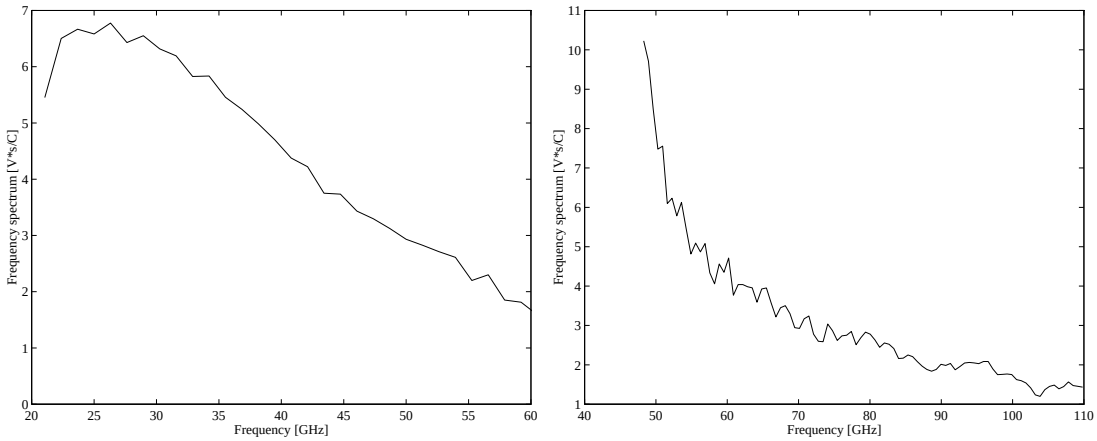


(a) WR28 pick-up (b) WR12 pick-up

Figure 3.11: Frequency response of the pick-ups.

The power spectrum gives an estimate of the signal strength, the square root of the power is obtained dividing the frequency spectrum by the (frequency dependent) impedance of the waveguide, $Z(\omega)$,

$$\sqrt{Power(\omega)} = \frac{pu(\omega)}{\sqrt{Z(\omega)}} \quad \left[\frac{\sqrt{W}}{Hz}\right]$$

The results for the power spectrum are shown in Figure 3.13. This quantity is important because its inverse Fourier transform squared gives the power (as a function of time) coupled to the pick-up.

$$Power(t) = \left| \mathfrak{F}^{-1}\left\{ \sqrt{Power(\omega)} \right\} \right|^2$$

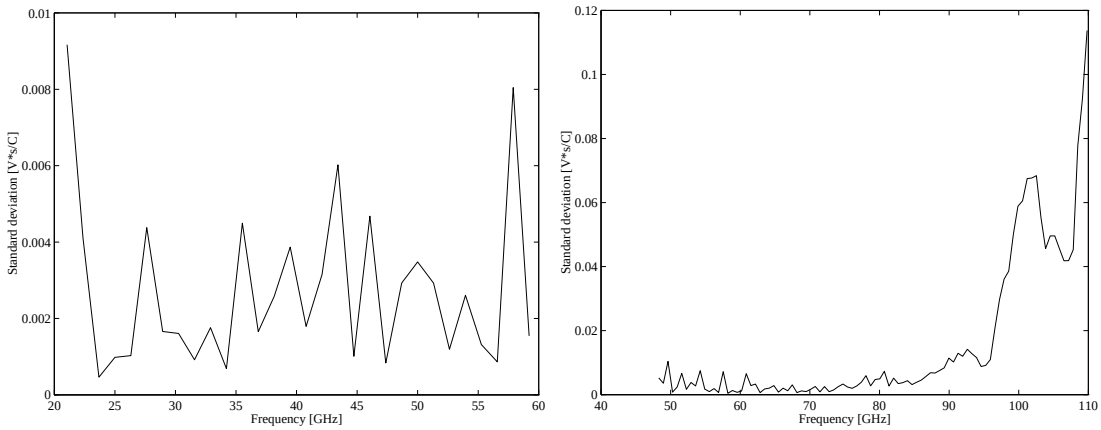


(a) WR28 pick-up (b) WR12 pick-up

Figure 3.12: Standard deviation.

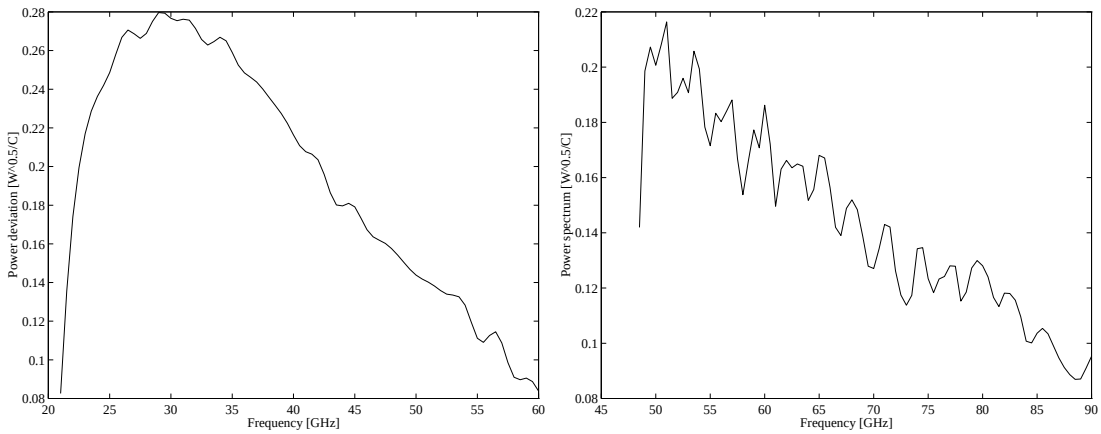


(a) WR28 pick-up (b) WR12 pick-up

Figure 3.13: Power spectrum.

### 3.4.1 Beam off Axis

The signal excited in the waveguide depends on the transverse position of the beam inside the beam pipe, therefore several simulations were also made to know how the amplitude of the signal changes when the beam is not centred. These simulation were made only for the WR28 waveguide as the first results already indicated that the variation of the signal did not depend on frequency. The different beam positions simulated are shown in Table 3.4.

In Figure 3.14(a) is shown the frequency spectrum of the signal excited in the waveguide for several vertical offsets ($x = 0$ always) and in Figure 3.14(b) are plotted the same amplitudes normalised to the amplitude of the centred beam. It can be seen that

| x | y | x | y | x | y | x | y | x | y |
|---|---|---|---|---|---|---|---|---|---|
| 0 | 3 | 3 | 3 | 3 | 0 | 3 | -3 | 0 | -3 |
| 0 | 5 | 5 | 5 | 5 | 0 | 5 | -5 | 0 | -5 |
| 0 | 7 | 7 | 7 | 7 | 0 | 7 | -7 | 0 | -7 |
| 0 | 9 | 9 | 9 | 9 | 0 | 9 | -9 | 0 | -9 |
| 0 | 11 | 11 | 11 | 11 | 0 | 11 | -11 | 0 | -11 |

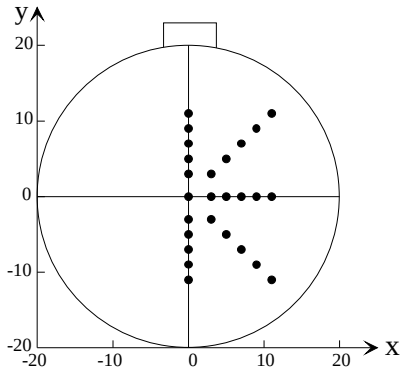


Table 3.4: Off-centre beam positions for MAFIA calculation.

the variation in amplitude with the offset is frequency independent in the range that we are measuring (26.5–40 GHz). The small changes for high frequencies are probably due to numerical errors. As it was expected when the beam is closer to the pick-up the amplitude of the signal increases while it decreases when the beam is further away.

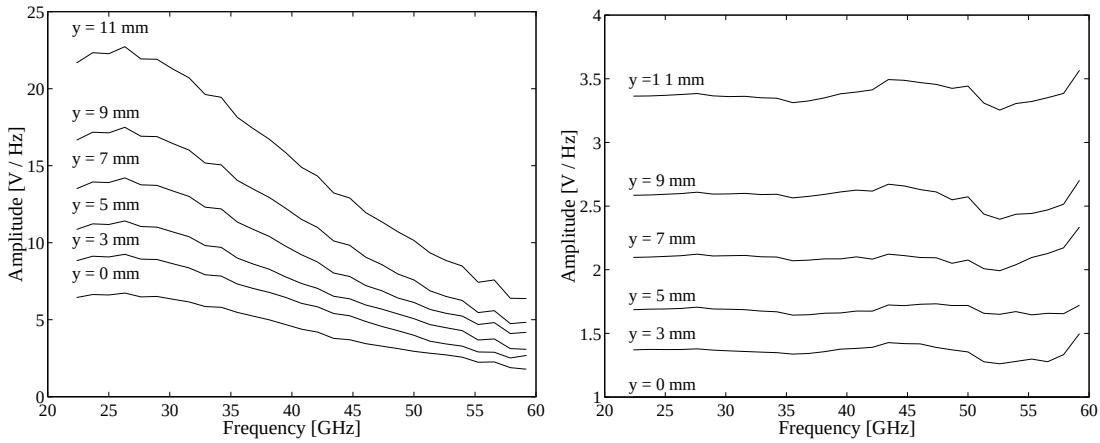


(a) Frequency spectrum.

(b) Normalised frequency spectrum.

Figure 3.14: Spectra for the different vertical offsets simulated with MAFIA.

In order to know the variation of the amplitude of the signal with respect to a centred beam, all of them were normalised to the spectrum of a centred beam. As the relative variation of the amplitude proved to be frequency independent the results are plotted for a single frequency (30 GHz) as a function of the offset in the different directions. Figure 3.15(a) shows the variation of the amplitude for different position of the beam along the *y* axis, in Figure 3.15(b) is shown the variation for the beam in different position along the *x* axis and Figures 3.15(c) and 3.15(d) show the variation as the beam moves

in diagonal, this two plots are symmetric as one would expect from the geometry of the set-up; the horizontal axe labels give the position of the beam on the $x$ axis and the $y$ position is given either by $y = x$ or $y = -x$, so that the distance to the centre is $\sqrt{2}x$. Table 3.4 gives the position of the beam for all the simulations.

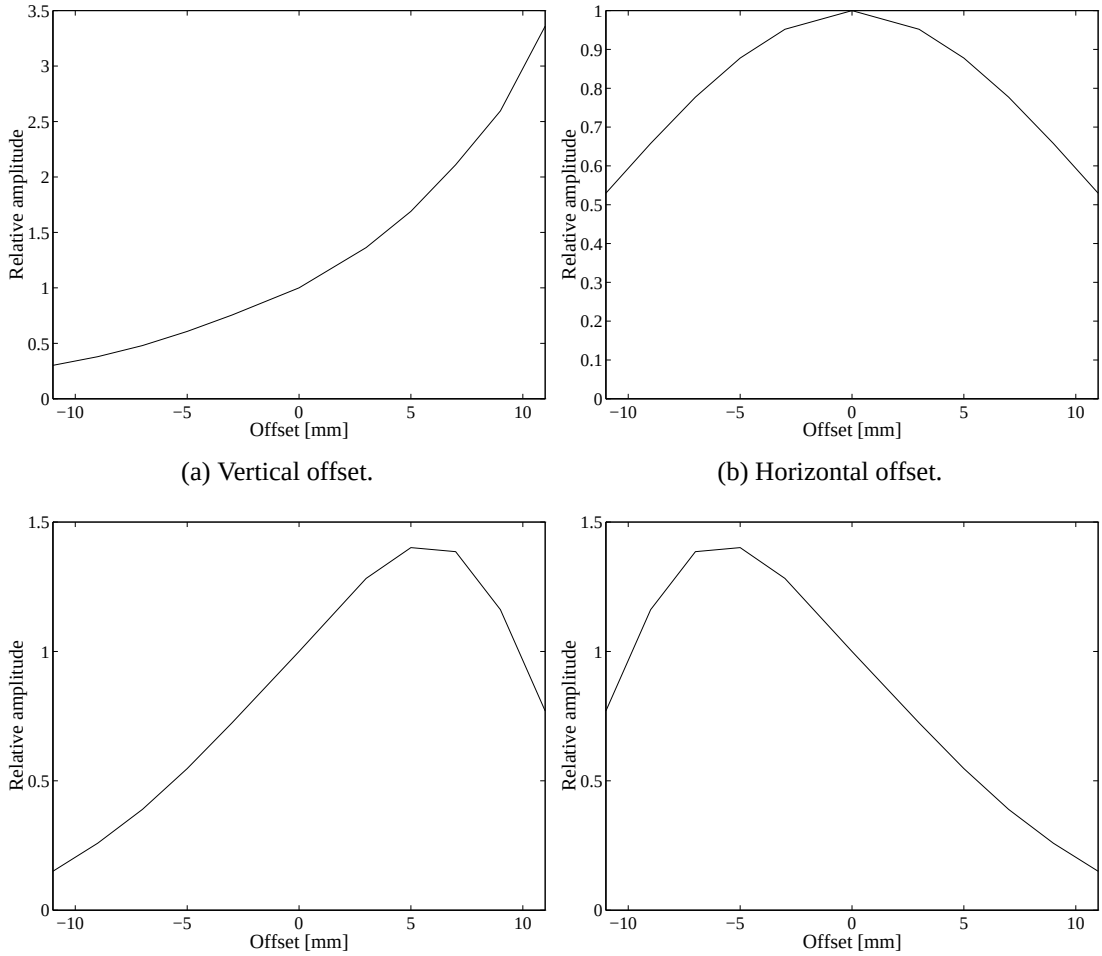


(a) Vertical offset.

(b) Horizontal offset.

(c) Diagonal (x = y) offset.

(d) Diagonal (x = -y) offset.

Figure 3.15: Signal amplitude for different bunch positions normalised to the amplitude when the beam is on axis.

## 3.5 Waveguides Used in the Monitor

Two types of rectangular waveguides are used to pick-up the e.m. field of the bunch, the WR28 covering the $K_a$ band (26.5–40 GHz) and the WR12 covering the E band (60–90 GHz). These frequency ranges are those where only the $TE_{10}$ mode propagates. In fact, the $TE_{10}$ starts to propagate at the cut-off frequency (21.1 GHZ for a WR28 and 48.4 GHz for a WR12), but for frequencies close to the cut-off the attenuation is very strong. Therefore the ranges given are those in which the attenuation is already weak enough to allow a good transmission, these are the "useful" ranges of the waveguide. The physical dimensions and other parameters of these waveguides are given in Table 3.5,

| | Inside | | Outside | | Cutoff | Frequency range | Theoretical |
|---|---|---|---|---|---|---|---|
| | Width [mm] | Height [mm] | Width [mm] | Height [mm] | frequency [GHz] | $TE_{10}$ mode [GHz] | attenuation [dB/m] |
| WR28 | 7.11 | 3.56 | 9.14 | 5.59 | 21.1 | 26.5–40 | 1.45–0.99 |
| WR12 | 3.099 | 1.549 | 5.130 | 3.581 | 48.4 | 60–90 | 2.57–1.72 |

Table 3.5: Characteristics of the waveguides used in the bunch length monitor.

Some (frequency dependent) characteristics of the transmission in these waveguides, such as impedance, attenuation and phase and group velocity, are plotted in Figure 3.16. The plot of the attenuation clearly shows, for both cases, that its amplitude increases to lower frequencies (as much as 50% from the highest to the lowest frequency plotted).

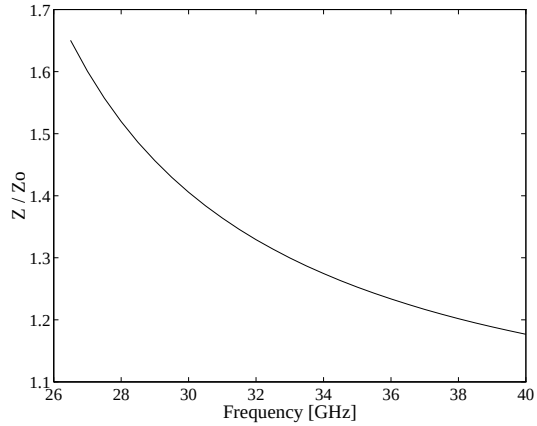


(a) WR28: impedance

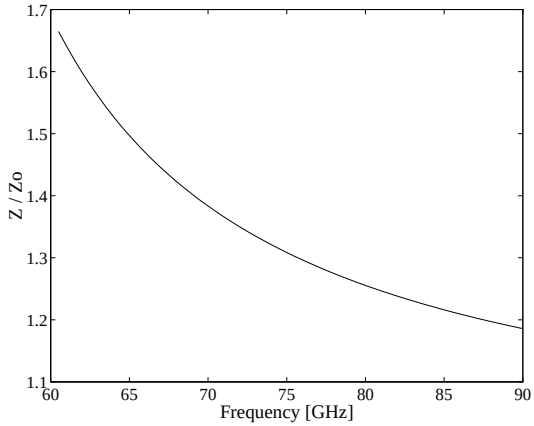


(b) WR12: impedance

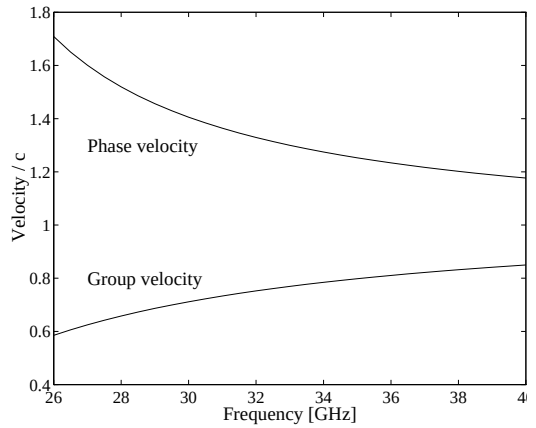


(c) WR28: propagation

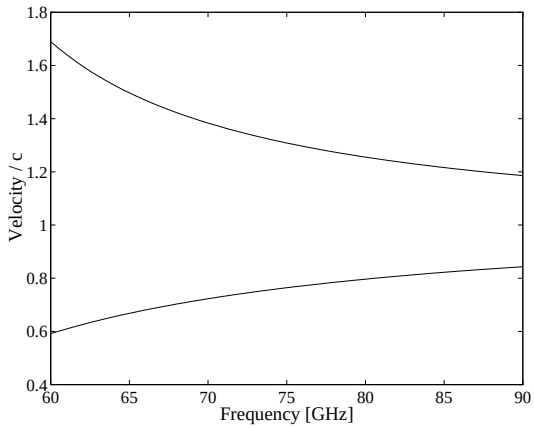


(d) WR12: propagation

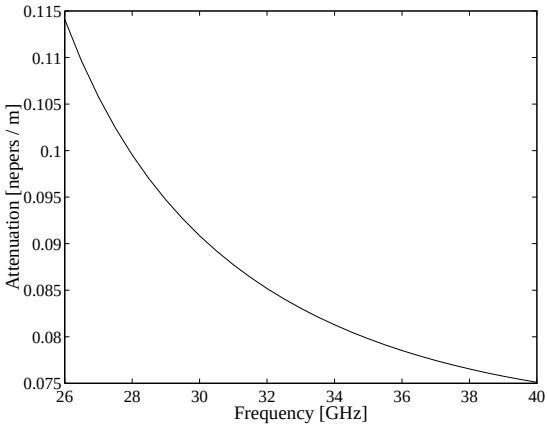


(e) WR28: attenuation

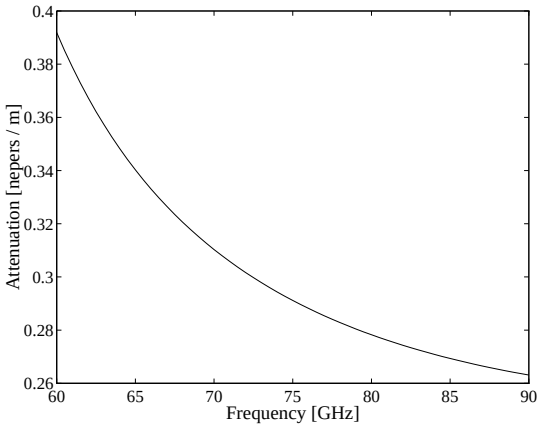


(f) WR12: attenuation

Figure 3.16: Waveguide characteristics.

## 3.6 Design of the Detection System

The detection system has to give the frequency spectrum of the signal, the variation of its amplitude with frequency will give the length of the electron bunch. In other words, we want to build a frequency spectrometer. Several system were designed for this purpose

- A mixer and a YIG filter
- Two mixers
- A power detector and a set of different high-pass filters

in the next sections these three systems are described.

Before going into details about theses system a short description on how mixers and YIG filters work is given.

### 3.6.1 YIG Filters and Mixer, Brief Description

A YIG filter is a tunable microwave filter. YIG stands for Yttrium-Iron-Garnet, that is the single-crystal material of the ferrimagnetic resonator that is used to magnetically tune the filter.

The filter used in the detection system is a multi-octave band filter from OMNIYIG, Inc. (California, USA), which characteristics are listed in Table 3.6. The maximum bandwidth of this filter is 65 MHz.

| Omniyig model No. | Frequency range | Insertion loss | Bandwidth at 3 dB | Off resonance isolation |
|---|---|---|---|---|
| M1022 | 2.0–12.4 GHz | 5 dB | 25–65 MHz | 50 dB |

Table 3.6: Characteristics of the YIG filter.

In our application the mixer can be regarded as a multiplier of two input signals, this is shown schematically in Figure 3.17. The signal applied to the RF port has a carrier frequency $\omega_s$ and a modulation waveform $A(t)$. The other signal, the LO (Local Oscillator), is a sinusoid at frequency $\omega_p$. As can be seen, by applying simple trigonometry, the output is found to consist of modulated components at the sum and difference frequencies. The sum frequency is then rejected by a low-pass filter. In this operating mode it is also called down converter. The use of nonlinear multipliers results in the generation of harmonics and different mixing products so that filtering is necessary to obtain the desired output.

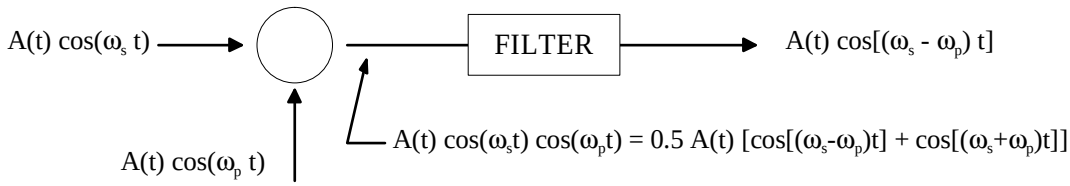


Figure 3.17: Schematic representation of a mixer as an ideal multiplier.

Different types of mixer are used for the experiments,

- A QMB-2808-AG balanced mixer with integral oscillator from QUINSTAR (California, USA) to cover the $K_a$ band (26.5–40 GHz). The local oscillator is set to 26.5 GHz.
- Three balanced mixers with integral local oscillators from ELVA-1 (Riga, Latvia) to cover different parts of the E band. The local oscillator were set to 56.5 GHz, 74.5 GHz and 75 GHz. The current set-up uses the 56.5 GHz and 74.5 GHz oscillators.
- Three double balanced mixer, model DB0218LW2 from MITEQ (NY, USA) covering the range 2–18 GHz and with and IF bandwidth of 750 MHz.

### 3.6.2 Mixer + Mixer

The two mixer are used to down-convert the frequency spectrum so that the signal can be read out directly with a digitizing oscilloscope. A detailed description is given of the application of this method to the $K_a$ band (26.5–40 GHz), the extension to the E band (60–90 GHz) is straight forward. Figure 3.18 shows an schematic representation of the detection process.

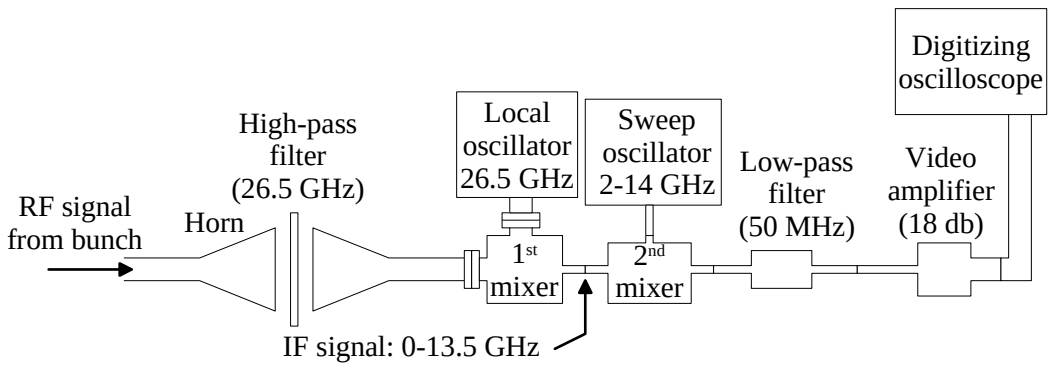


Figure 3.18: Schematic representation of the two-mixer detection system.

The signal coming from the bunch and travelling trough the WR28 waveguide extends from 21.1 GHz to 40 GHz for the dominant mode $TE_{10}$, although the specification for the waveguide range is 26.5–40 GHz it is advisable to use a high-pass filter to cut off the signal below 26.5 GHz. See Figure 3.19 for a graphical representation of the following description. The first mixer with a LO at 26.5 GHz will downconvert the whole frequency spectrum so that the output signal will be in the range 0–13.5 GHz. The second mixer has a sweeping LO, it will downconvert the signal according to the frequency given by the LO. To clarify the procedure lets assume that the LO is at 8 GHz, then the frequency spectrum (0–13.5 GHz) will be shifted to the range 0–5.5 GHz, although the output signal if limited to 750 MHz because of the bandwidth of the mixer. The oscilloscope will read only the signal within its bandwidth what will give us the amplitude of the signal at 8 GHz (± oscilloscope bandwidth). The oscilloscopes reads the signal at each frequency step of the LO oscillator. Two optional elements can be used in order to improve the measured signal, an additional low pass filter to reduce the bandwidth of the signal read by the oscilloscope and an amplifier to increase the signal.

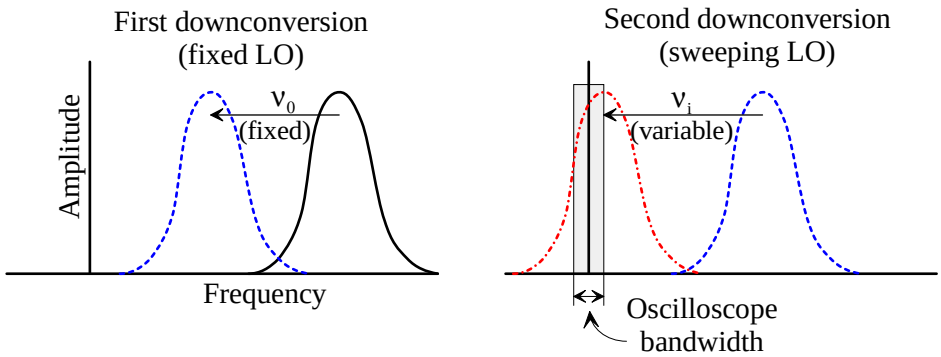


Figure 3.19: Spectrum downconversion.

The same process that is done by this combination of two mixer could have been achieved with only one mixer and a sweeping oscillator in the frequency range 26.5–40 GHz. However, the cost of such a source, at these very high frequencies, is much larger than the cost of the second mixer with a 2–15 GHz local oscillator and exceeds the budget of the experiment. Furthermore, such a system would not necessarily give a better accuracy, although it could be more compact and easy to install.

### 3.6.3 Power Detector + High-Pass Filters

The power detector used is a planar-doped barrier detector HP R422C (from Hewlett Packard), for the $K_a$ band and a ELVA detector for the E band. The power detector is

coupled to the waveguide output and the signal is directly read by the oscilloscope, as shown in Figure 3.20.

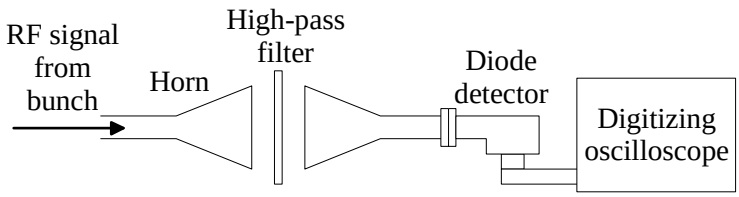


Figure 3.20: Power detector set-up.

The power spectrum can be obtained by using a set of filters with different cut-off frequencies. For each filter the detector will give the intensity integrated over a different frequency range. From this data, together with the transmission function of each filter it is possible to reconstruct the power spectrum.

### 3.6.4 Mixer+YIG Filter+Power detector

This set-up is similar to the previous ones where we used high-pass filter. The frequency spectrum is first shifted by the mixer so that it is within the frequency range of the YIG filter (2.0–12.4 GHz). The YIG filter is a tunable band-pass filter, when tuned at a certain frequency the power detector will integrate the intensity of the signal over the bandwidth of the filter ($\sim$50 MHz). By moving the filter across the whole spectrum we will obtain the power at each frequency (integrated over the filter bandwidth) and finally we can reconstruct the power spectrum.

During the tests made with this system it was not possible to obtain any signal on the scope. The signal amplitude after the passage through the filter is too low to be measured by the power detector. However, it is not possible to increase the input signal intensity because its maximum intensity is limited by the mixer installed before the YIG filter. This problem could be solved with the use of a more sensitive power detector or an amplifier at the exit of the mixer, however the equipment at so high frequencies is very expensive and none of this devices was acquired.

## 3.7 Microwave Filters Design

Perforated metal plates (grids) can be used for the construction of transmission filters in the far infrared and in the microwave regions. The complementary structure, a periodic array of metallic disks, also possesses filtering properties. Although these type of filter

are in use since many years some filter with new characteristics were designed and fabricated to fulfill the requirements of our detection system.

The geometry of the apertures (circular, rectangular, cross-like) determines the main characteristic of the filter, a plate perforated with slots has bandpass properties while if perforated with circular holes acts as a high-pass filter [47–49], moreover the reflection characteristics of a high-pass transmission filter is that of a low-pass filter. The two dimensional arrangement of the holes (symmetry, distance between holes) and the thickness of the plate determine the filtering properties of the grid. For example, increasing the thickness enhances the filtering properties (the slope of the transmission curve at the cut-off frequency gets steeper) but it also reduces the transmission and can lead to Fabry-Perot-like resonances under certain conditions [50].

Fabry-Perot resonances can appear when the radiation is reflected back and forth between the boundaries of the holes. The condition to obtain a resonance is that the thickness of the plate, d, has to be an integer multiple of half the wavelength, $\lambda$, for normal incidence. In general, for a radiation with an angle of incidence $\theta$, the condition is written as

$$\frac{\lambda}{2} = \frac{nd\cos\theta}{m} \tag{3.50}$$

where $n$ is the refractive index of the medium and $m$ is an integer.

A grid with circular holes will behave as a high-pass filter. The cut-off frequency of the transmission spectrum, $\nu_c$, is obtained regarding the holes as cylindrical waveguides. As in a cylindrical waveguide the electromagnetic fields is characterised in TE and TM modes the cut-off wavelength of each mode is given by

$$\lambda_{c,mn} = \frac{2\pi}{\chi_{mn}}a \qquad \text{for TM modes} \tag{3.51}$$

$$\lambda_{c,mn} = \frac{2\pi}{\chi'_{mn}}a \qquad \text{for TE modes} \tag{3.52}$$

where $a$ is the radius of the cylindrical waveguide, $\chi_{mn}$ is the $n$th non-vanishing root of the $m$th-order Bessel function, $J_m(\chi)$, and $\chi'_{mn}$ is the $n$th non-vanishing root of its derivative.

Table 3.7 shows the values of $\chi_{mn}$ and $\chi'_{mn}$ for the first modes. The lowest cut-off is for the $TE_{11}$ mode and is given by

$$\frac{1}{\lambda} = \frac{0.586}{2a} \tag{3.53}$$

which will be the frequency cut-off for the transmission spectrum.

| roots of J($\chi$) | | | | | |
|---|---|---|---|---|---|
| | | m | | | |
| | | 0 | 1 | 2 | 3 |
| n | 1 | 2.405 | 3.832 | 5.136 | 6.380 |
| | 2 | 5.520 | 7.016 | 8.417 | 9.761 |

| roots of J'($\chi$) | | | | | |
|---|---|---|---|---|---|
| | | m | | | |
| | | 0 | 1 | 2 | 3 |
| n | 1 | 3.832 | 1.841 | 3.054 | 4.201 |
| | 2 | 7.016 | 5.331 | 6.706 | 8.015 |

Table 3.7: Roots of the *m*th-order Bessel function and its derivative.

### 3.7.1 Theoretical Model

The theoretical formalism shown here is based on the method of moments for inductive grids and was developed initially by Chen in [51, 52], application of these grids to solar selective surfaces and corresponding microwave measurements have also been considered in [53].

Consider a planar electromagnetic wave incident on a perfectly conducting screen perforated with apertures as shown in Figure 3.21. The grid is assumed to be infinite in extent, $d_x$ is the period of the array in the x direction while $d_y$ is the projection of the other period of the array onto the y direction. The angle $\alpha$ is formed between the directions of periodicity. The incident wavevector $\vec{k}$ is at an angle $\theta$ to the normal of the grid and $\phi$ is the angle between the x axis and the projection of $\vec{k}$ onto the x-y plane (the screen surface).

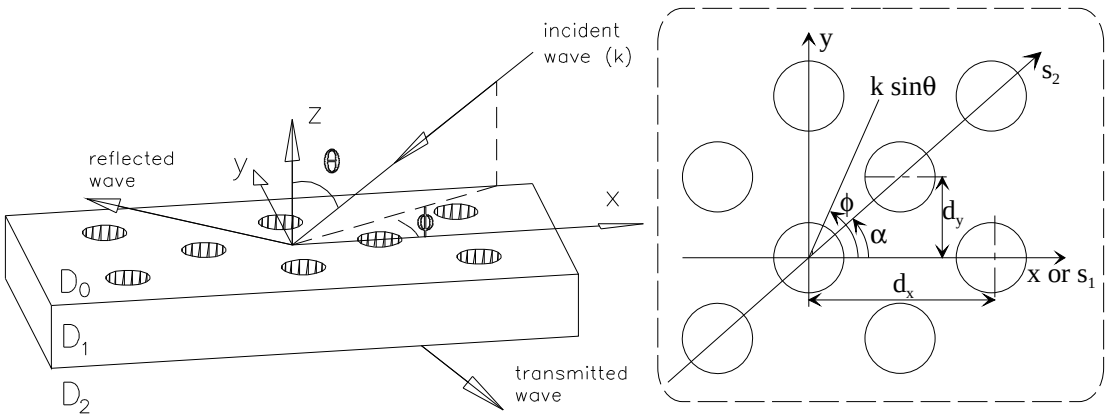


Figure 3.21: Geometry of a two-dimensional array of circular holes.

Let us divide the space into three regions, $D_0$, $D_1$ and $D_2$. $D_0$ and $D_2$ are the regions above and below the grid and $D_1$ is the region within the aperture. Expanding the unknown electric and magnetic field distribution near the screen in a set of Floquet's mode functions and relating the unknown fields in each region by means of continuity

conditions at the surfaces an integral equation is obtained for the unknown fields in each aperture. The integral equation is reduced, by the method of moments, to a set of linear algebraic equations which can then be numerically solved with the use of a computer.

The transverse components of the electric field above and below the mesh can be written as discrete sums over plane waves

$$E_t(x,y,z) = E_t^i + \sum_{rpq} E_{rpq}\Phi_{rpq}(x,y,z) \tag{3.54}$$

in $D_0$ and

$$E_t(x,y,z) = \sum_{rpq} E_{rpq}\hat{\Phi}_{rpq}(x,y,z) \tag{3.55}$$

in $D_2$, where $\Phi_{rpq}(x,y,z)$ and $\hat{\Phi}_{rpq}(x,y,z)$ represent upward and downward travelling plane waves. The transverse components of the magnetic fields, $H_t$ can be expressed in a similar manner. The subscript $r$=1,2 is used to indicate TE or TM waves, respectively. The orthonormal mode functions can be expressed as

$$\Phi_{pq}^{TE} = \frac{1}{\sqrt{d_x d_y}}\left(\frac{v_{pq}}{t_{pq}}\hat{x} - \frac{u_{pq}}{t_{pq}}\hat{y}\right)\Psi_{pq} \tag{3.56}$$

$$\Phi_{pq}^{TM} = \frac{1}{\sqrt{d_x d_y}}\left(\frac{u_{pq}}{t_{pq}}\hat{x} + \frac{v_{pq}}{t_{pq}}\hat{y}\right)\Psi_{pq} \tag{3.57}$$

where $\Psi_{pq}$ is the scalar mode potential that, with the exp(j$\omega$t) time dependence omitted, can be written as [54]:

$$\Psi_{pq} = \exp(-j(u_{pq}x + v_{pq}y + \gamma_{pq}z)) \tag{3.58}$$

where

$$\begin{aligned} u_{ps} &= k\sin\theta\cos\phi + \frac{2\pi p}{d_x} \\ v_{ps} &= k\sin\theta\sin\phi + \frac{2\pi q}{d_y} - \frac{2\pi p}{d_x\tan\alpha} \\ \gamma_{pq} &= \begin{cases} \sqrt{k^2 - t^2} & \text{for } k^2 \geq t^2, \\ -j\sqrt{k^2 - t^2} & \text{for } k^2 < t^2 \end{cases} \end{aligned} \tag{3.59}$$

with

$$t_{pq}^2 = u_{ps}^2 + v_{ps}^2$$

for $p,q = 0,\pm1,\pm2,...,\pm\infty$

The orders ($p$,$q$)=(0,0) correspond to specularly reflected and transmitted orders, other orders correspond to diffracted waves. The modal propagation constant $\gamma_{pq}$ is positive and real for the propagating modes and is negative and imaginary for evanescent modes.

For the case of an isosceles triangular array where the element spacings and the angle of incidence satisfy

$$\left(\frac{\lambda}{d_x}\right)^2 + \left(\frac{\lambda}{2d_y}\right)^2 \geq (1+\sin\theta)^2 \tag{3.60}$$

and

$$2\left(\frac{\lambda}{d_x}\right), \left(\frac{\lambda}{d_y}\right) \geq 1+\sin\theta \tag{3.61}$$

the distant scattered field consist of the $p = q = 0$ modes, otherwise other modes may also exist. In the later case, an anomaly will appear, in the transmission and reflection spectra, at the frequency points where orders cease to propagate. These discontinuities are known as "Wood anomalies".

The fields within the circular apertures are written as sums over circular waveguide modes $\Psi_{snml}(\rho,\theta)$

$$E_t(x,y,z) = \sum_{snml} \left[a_{snml}\sin k_2\nu_{snml}z + b_{snml}\cos k_2\nu_{snml}z\right]\Psi_{snml})(x,y) \tag{3.62}$$

where $n$ and $m$ are integers. The subscript $s$ distinguishes TE and TM modes while $l$ distinguishes modes having zero azimuthal component (horizontal modes) from those having zero radial component (vertical modes). Also

$$\nu_{1nm} = \sqrt{1-\frac{\chi'^2_{nm}}{(k_0a)^2}} \tag{3.63}$$

$$\nu_{2nm} = \sqrt{1-\frac{\chi^2_{nm}}{(k_0a)^2}} \tag{3.64}$$

where $J'(\chi'_{nm}) = 0$ and $J(\chi_{nm}) = 0$ and $J_n$ and $J'_n$ are the $n$th order Bessel function and its derivative, respectively.

The amplitude of the plane wave expressions is found by applying continuity conditions at the surfaces of the grid and by numerically solving the resulting equations with the help of a computer. Different authors have shown the good concordance of this theoretical model with experimental measurements [49, 50].

### 3.7.2 High-Pass Filter Design

A series of high-pass filters were manufactured by drilling circular holes in brass plates. The diameter of the holes were determined by the required cut-off frequency for each filter according to (3.53). Although the behaviour of this type of filter is shown in several papers different samples of filters were designed, constructed and measured in order to obtain the most suitable parameters for our requirements. A Microwave Network Analyzer HP8722A capable of characterising the frequency response of RF components from 50 MHz up to 40 GHz, with a frequency resolution of 100 kHz, was used to measure the transmission and reflection coefficient of the filters. Figure 3.22 shows an schematic layout of the set-up for the measurements of the filter characteristics.

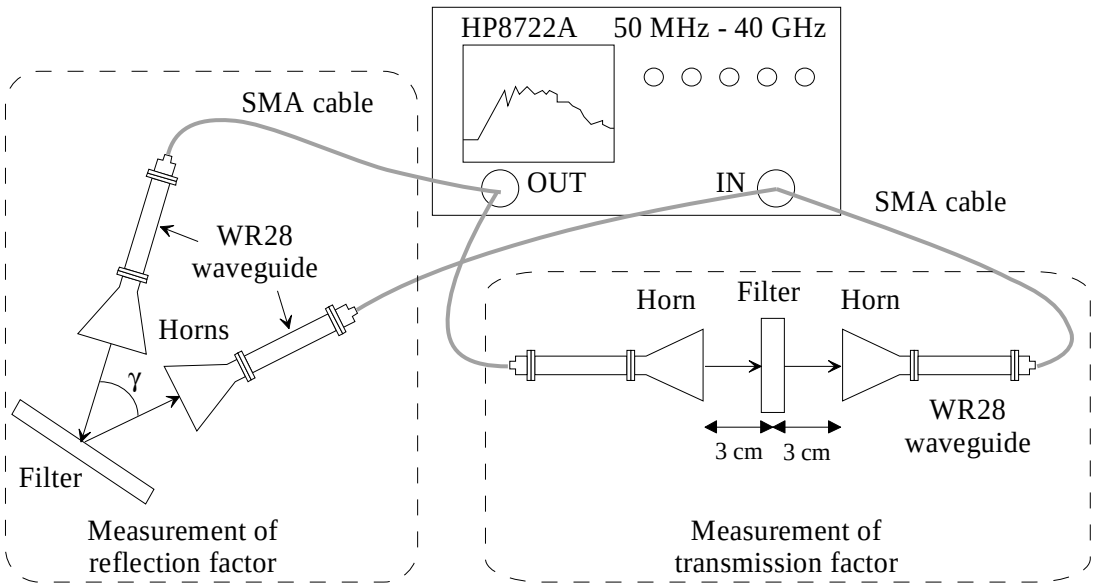


Figure 3.22: Layout of the measurement set-up.

The first samples were designed to obtain a cut-off frequency at 26.6 GHz. The geometric parameters (see Figure 3.21) were $\alpha = 60^o$, $d_x$ = 6.9 mm and $d_y$ = 6.0 mm with a hole radius of 3.3 mm and two different thicknesses, 13.2 mm (twice the diameter) and 26.4 mm (four times the diameter). Figure 3.23 shows an schematic layout.

The characteristics of these filter were measured according to the plot in Figure 3.22. These characteristics were measured several times in different conditions but only typical samples are shown in this report. The results obtained for the transmission coefficient are shown in Figure 3.24(a) and 3.24(b) for the two different thicknesses. The transmission curve increases around 26.6 GHz (the cut-off frequency, indicated in the plot by the pointer number 2), it is clearly seen that the cut-off properties improve with a

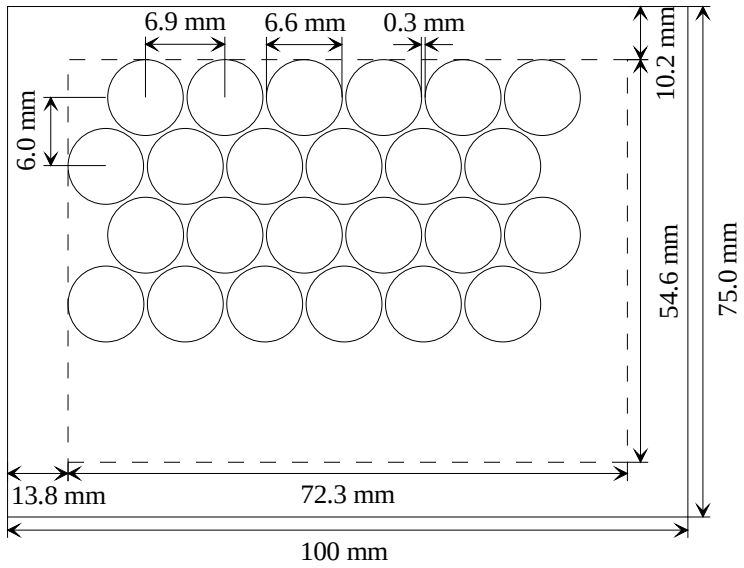


Figure 3.23: Design of a filter with a cut-off frequency of 26.5 GHz.

thicker plate but at the same time some resonances appear and the curve seems to ripple more.

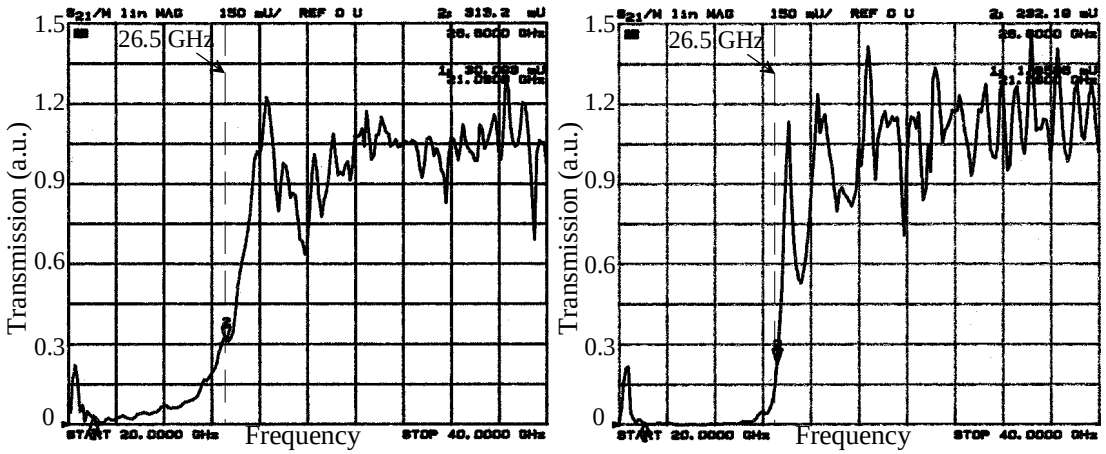


(a) 13.2 mm thick filter (b) 26.4 mm thick filter

Figure 3.24: Transmission spectrum.

The reflection properties were also measured and a sample of the results can be seen in Figure 3.25(a) and 3.25(b). The reflection spectrum is that of low-pass filters with a cutoff frequency around 26.6 GHz. The band-pass characteristic that show the Figure 3.25(a) and 3.25(b) is due to the fact that only waves with a frequency above 21.05 GHz are transmitted in the waveguide of the network analyzer.

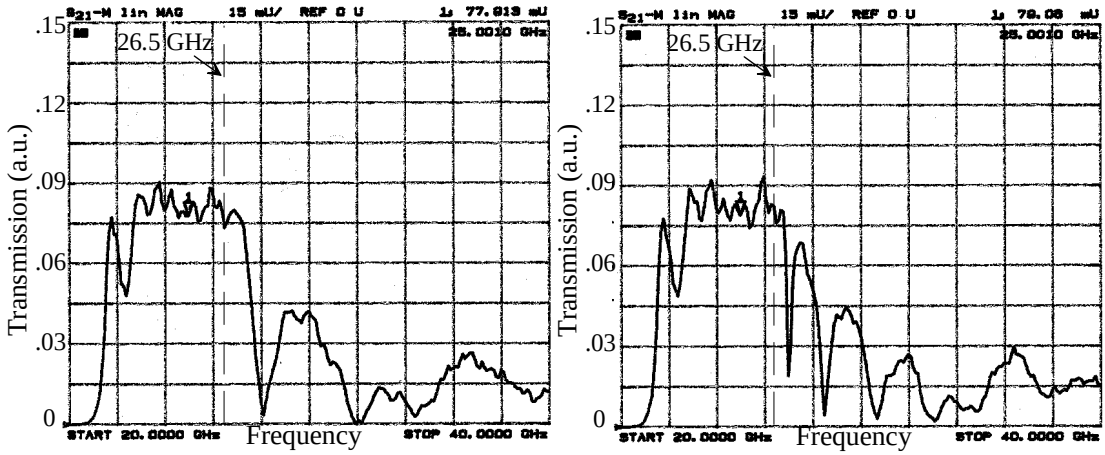


(a) 13.2 mm thick filter (b) 26.4 mm thick filter

Figure 3.25: Reflection spectrum.

In order to try to avoid the resonances in the transmission curve, two new filters were designed and tested. These new filters do not have simple holes perforated but in order to smooth the transition a conical edge was added to each side of the cylindrical hole. The designs of both filters are shown in Figure 3.26 and Figure 3.27, they differ in the total thickness (although the thickness of the cylindrical hole is the same in both cases) and in the angle of the conical edge, $30^o$ and $20^o$ respectively.

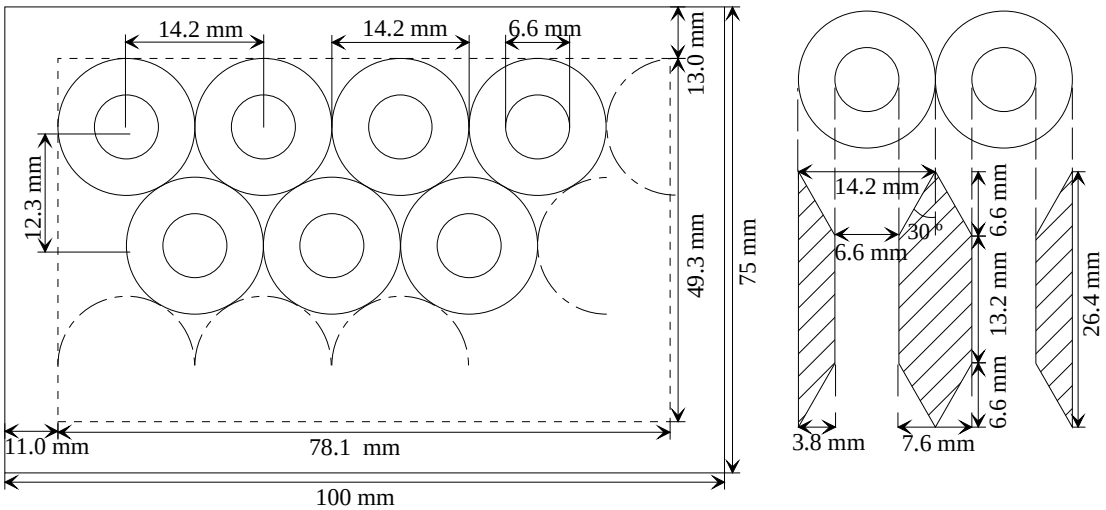


a) front view b) lateral view

Figure 3.26: Filter with cut-off frequency at 26.5 GHz and conical edges at an angle of $30^o$.

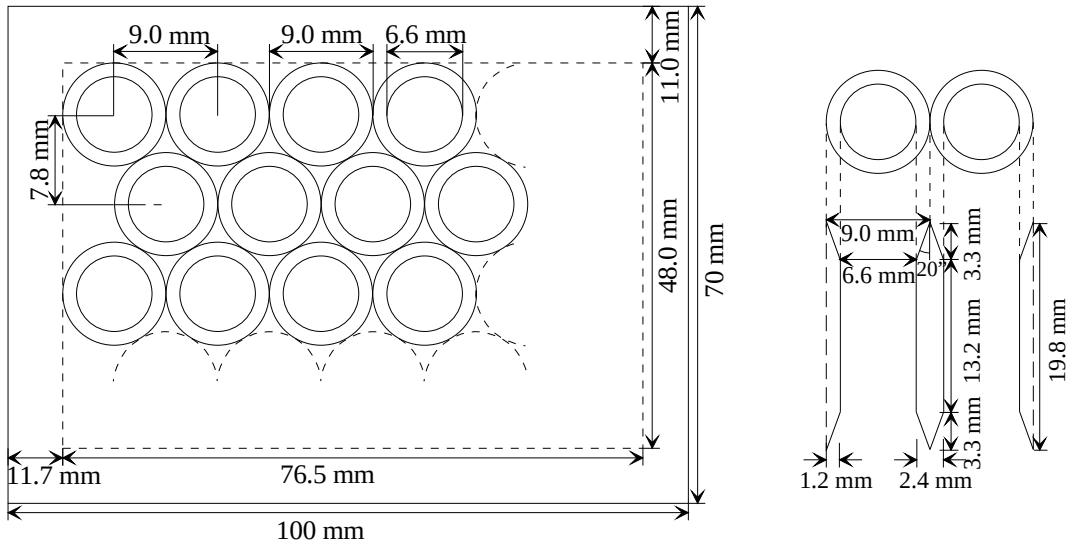


a) Front view b) lateral view

Figure 3.27: Filter with cut-off frequency at 26.5 GHz and conical edges at an angle of $20^o$.

The transmission and reflection characteristics of these filters were measured in the same way than the previous ones and the results are shown in Figure 3.28 and 3.29 respectively. It can be seen that the number and amplitude of the resonances decreases with the conical edges but the transmission is lower as a consequence of the reduction in the number of holes per unit of surface.

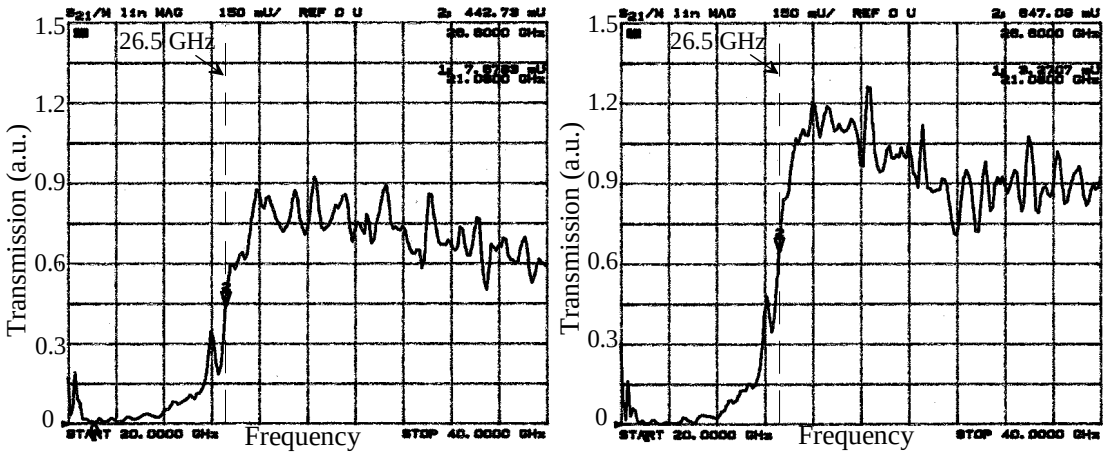


(a) $30^o$ angle for the edge (b) $20^o$ angle for the edge

Figure 3.28: Transmission spectrum.

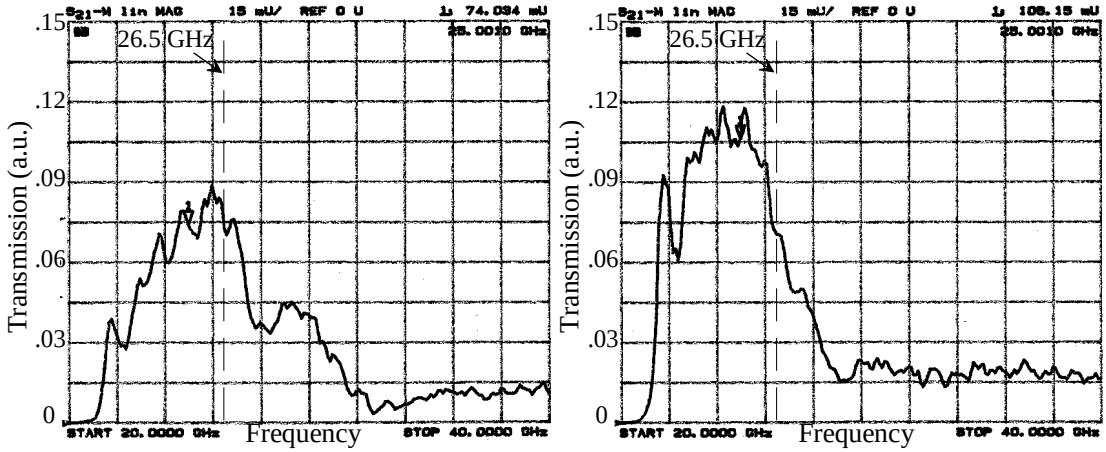


(a) $30^o$ angle for the edge (b) $20^o$ angle for the edge

Figure 3.29: Reflection spectrum.

As a compromise between good transmission and few resonances it was decided to make the high-pass filter according to Figure 3.27, the conical edge would have an angle of $20^o$, the thickness of the cylindrical hole would be twice its diameter while the thickness of the conical edge would be half its diameter (being the total thickness 3 times its diameter).

A series of high-pass filters were prepared for different cut-off frequencies, with conical edges at an angle of $20^o$. The diameter of the different filters were obtained according to Equation (3.53) for the different frequencies. In next table can be found the main parameters of the filters, cut-off frequency ($\nu_c$), hole diameter (d), period in x and y direction ($d_x$ and $d_y$), and thickness (t).

| $\nu_c$ [GHz] | d [mm] | $d_x$ [mm] | $d_y$ [mm] | t [mm] |
|---|---|---|---|---|
| 26.6 | 6.6 | 9.0 | 7.8 | 19.8 |
| 30.0 | 5.86 | 8.00 | 6.93 | 17.58 |
| 35.0 | 5.02 | 6.84 | 5.92 | 15.06 |
| 40.0 | 4.39 | 5.99 | 5.19 | 13.17 |
| 56.5 | 3.11 | 4.23 | 3.66 | 9.32 |
| 70.0 | 2.51 | 3.41 | 2.95 | 7.52 |
| 74.5 | 2.36 | 3.22 | 2.79 | 7.08 |
| 75.0 | 2.34 | 3.20 | 2.77 | 7.02 |
| 80.0 | 2.20 | 3.00 | 2.60 | 6.60 |

# Chapter 4

# Experimental Set-up of the Bunch Length Monitor in the CTF

This chapter describes the CTF drive beam (see Chapter 1) with special regard to the instrumentation and the bunch compressor, that can reduce the bunch length down to 0.5 ps (rms). The set-up of the Bunch Length Monitor (BLM) in this linac as installed in 1997 is described in detail as well as the measurement and data acquisition procedure which are in use. The detection can be made with a diode detector or with the two-mixers technique. In both cases the data acquisition is driven by a PC using programs specially made for this purpose. Some typical experimental signals are shown.

## 4.1 CTF Drive Beam Instrumentation

The CTF drive beam accelerator is a S band linac, that is working at a RF frequency of 3 GHz [8]. It can work in single bunch mode or with a train of bunches (2 to 48). The nominal radius of the beam pipe is 20 mm although some elements, like the accelerating structures, have a smaller aperture. Figure 4.1 shows a schematic layout of the CTF drive beam line showing the position of the beam diagnostic elements. The BLM is labelled as microwave spectrometer and it is installed downstream of the bunch compressor.

The electron bunches are produced inside a RF gun by illuminating a photocathode with a laser pulse, this system allows the generation of very short (8-10 ps fwhm) high charge bunches. The RF gun [14] has 2+1/2 S-band cells with an iris diameter of 40 mm and a $Cs_2Te$ photocathode [10] placed on the backplane. The cathode is illuminated by a laser pulse of 262 nm wavelength [12] and the electrons emitted are then accelerated by the field inside the gun (100 MV/m) to an energy of 7 MeV.

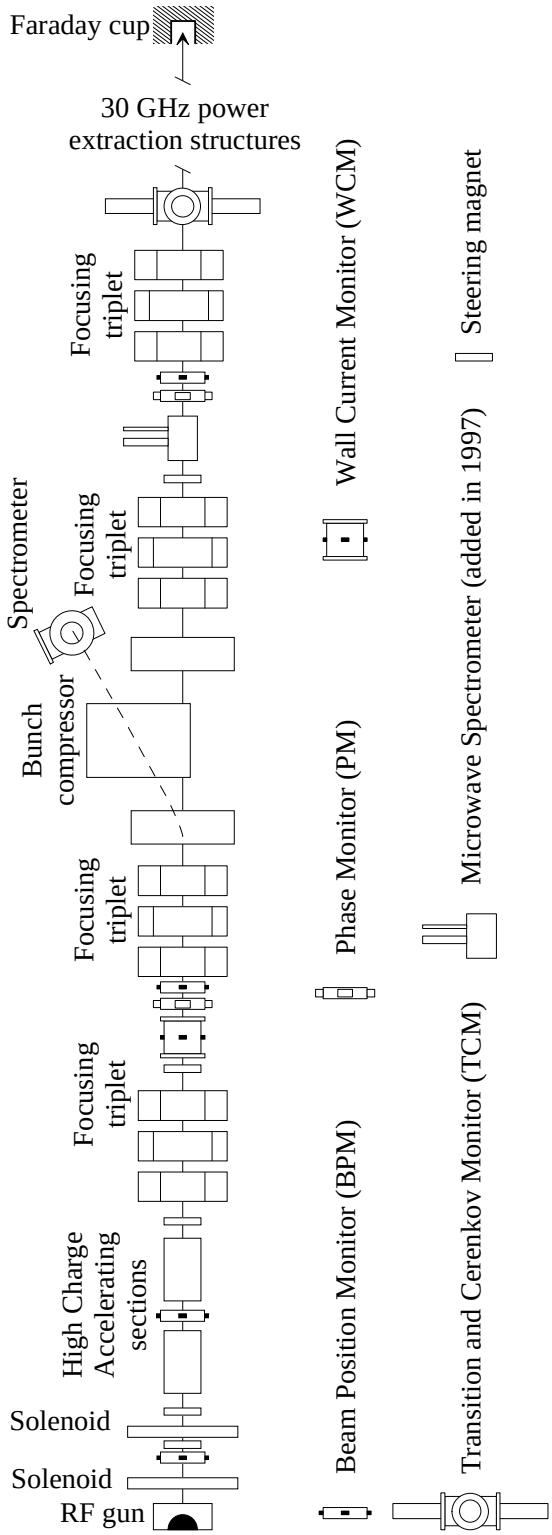


Figure 4.1: The CTF instrumentation.

The solenoids, that follow the RF gun, focus the beam before going into the High Charge Accelerating Structures (HCS) which will accelerate the bunches up to 50 MeV. The HCSs are specially designed to compensate for the strong beam loading caused by the high charge beam when operating with a train of bunches [15]. A sequence of quadrupoles allow to keep the beam focused before compression and the steering magnets correct the beam trajectory in both transverse directions. Several monitors are installed to measure the beam characteristics (charge, transverse position, phase).

The bunch compressor can reduce the length of the bunch down to 0.5 ps rms and will be described in detail in the next section. One of the dipole magnets of the bunch compressor can also be used as a spectrometer to measure the energy spectrum of the beam. After the bunch compressor several quadrupoles and steering magnets are used to match the beam to the aperture of the 30 GHz section, which has a 7.5 mm radius beam pipe. In the 30 GHz power extraction structures the beam is decelerated to produce power at 30 GHz in order to accelerate the main beam. The transition or Cĕrencov radiators are used to measure the bunch length and the emittance of the beam. Finally the beam is dumped in a Faraday Cup that measures the charge. A spectrometer (not drawn in Figure 4.1) is also installed at the end of the beam line to measure the final beam energy spectrum, after the passage through the 30 GHz power extraction sections.

The beam diagnostic elements installed are [55]:

- Beam Position Monitors (BPM).
  They indicate the position of the beam in the transverse plane by using 4 buttons (antennas) placed around the beam pipe. The difference in amplitude of the four signals gives the beam position.

- Phase Monitors (PM).
  They give the phase of the beam with respect to the 3 GHz RF. Mechanically they are identical to the 4 button BPMs but have a different readout electronics.

- Wall Current Monitors (WCM).
  Measures the charge of the bunch. They are composed of 6 feedthrough around the beam pipe (so as to be beam position independent) that measure the image current of the beam travelling on the beam pipe wall.

- Transition and Cĕrenkov Monitors (TCM).
  A pneumatic system introduces in the beam line an aluminium (0.5 mm thick) or a sapphire foil (0.3 mm thick) to produce transition or Cĕrenkov radiation respectively. The radiation is then analysed with the help of a CCD camera or a streak camera to measure the bunch transverse dimensions or the bunch length.

- Spectrometer.
  A dipole magnet deviates the beam so that it hits a scintillating screen. The energy spectrum of the bunch is measured by varying the magnetic field of the magnet as the deviation angle is proportional to the bunch momentum.

- Beam Loss Monitors.
  Measure the radiation emitted by the bunch. They are very useful to optimise the transmission as they indicate where the beam hits the chamber or is deviated. As they are moveable, they are not shown in Figure 4.1.

- Microwave Spectrometer or BLM.
  These are the rectangular RF pick-ups installed to collect the electromagnetic field of the bunch.

- Faraday Cup.
  Measures the beam charge at the end of the linac.

## 4.2 Bunch Compressor

The bunches in the CTF are compressed in a magnetic chicane composed of three dipole magnets, the one in the centre having inverted polarity with respect to the other two [16].

In a dipole magnet the electrons are deflected according to their energy, the particles with less energy follow a trajectory with a smaller radius than the ones with more energy. In a magnetic chicane this is translated in a longer path length for particles with less energy. In order to obtain compression with this method the energy in the bunch has to increase from head to tail. This effect can be achieved by a proper phasing of the accelerating structures. Then, the head of the bunch, with a lower energy, arrives first at the entrance of the chicane but follows a longer path while the particles in the tail, with more energy, arrive later but follow a shorter path. The global effect is a shortening of the bunch as shown schematically in Figure 4.2.

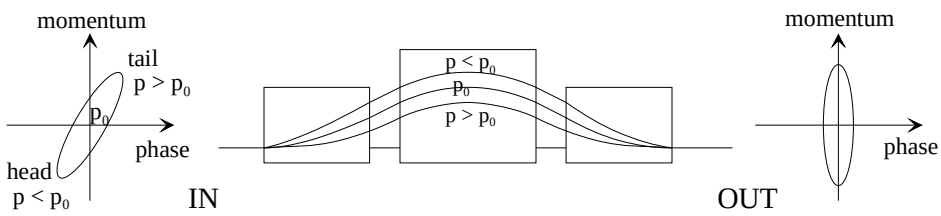


Figure 4.2: Compression in a magnetic chicane.

In order to have the beam centred (in the transverse plane) at the exit of the chicane the condition $\int Bdl = 0$ has to be fulfilled, $B$ is the magnetic induction and the integral is done over the particle trajectory . In our case the currents feeding the dipole magnets have to follow the relation

$$I_c = 1.2 \times I_e \tag{4.1}$$

where $I_c$ is the current in the central magnet and $I_e$ is the current of the other two (that are equal) [55]. The ratio between the current and the magnetic field in the magnets are

$2.49 \times 10^{-3}$ T/A for the central magnet and
$2.47 \times 10^{-3}$ T/A for the end magnets.

The compression ratio depends on two factors, the energy spread along the bunch and the current in the dipoles (that gives the intensity of the magnetic field). The energy spread along the bunch is controlled by the choice of the phase in the accelerating sections. The phase of these elements can not be arbitrarily chosen but has to be a compromise between obtaining the desired energy gain and having enough energy spread to allow compression. Once the phase is fixed the compression factor can be varied by changing the intensity of the current in the magnets, always constrained by Equation 4.1.

## 4.3 BLM Installation

The first RF pick-up (for a WR28 waveguide) was installed at a distance of 10.90 m from the photocathode (reference of all the longitudinal distances in the CTF) and there were 16.2 m of waveguide before reaching the detector. In this position the pick-up was very close to a BPM (so that it was possible to check that the beam is centred) and 1.40 m before a TCM. The first measurements showed that the TCM introduced a disturbance in the detected signal even when none of the foils were in the beam line (see Chapter 5). The TCM produces a discontinuity in the beam pipe impedance, the electromagnetic fields of the bunches are distorted and partially reflected and the pick-up also collects this signal, which is then superimposed (although delayed in time) to the original signal coming from the bunch. Therefore it was decided to move the pick-up away from the TCM.

The final installation of the two pick-ups (the second one for the WR12 waveguide) is as shown in Figure 4.3. The length of the two waveguides installed to reach the detector is different, the WR12 waveguide is 12 m long while the WR28 is 16 m (the latter one has a special delay line installed). A minimal waveguide length of 12 m is necessary

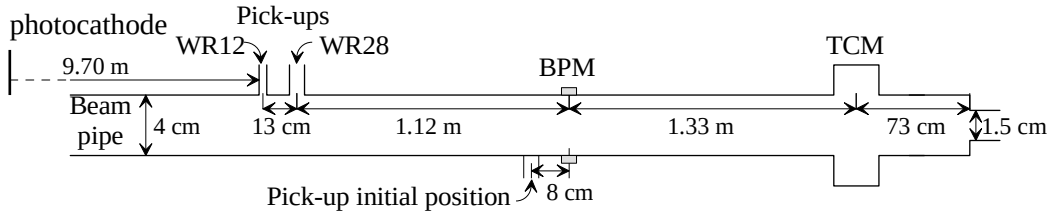


Figure 4.3: Pick-up situation.

to reach the detector situated in a room above the CTF hall. However, the waveguide introduces a dispersion in the signal (each frequency travels with a different velocity) that helps to separate the different frequencies as they will arrive at different times to the detector. Therefore, one would like to have a waveguide as long as possible. Yet another factor to take into account is the attenuation in the waveguide, that is much stronger in the WR12 ($\sim$0.2 dB/m) than in the WR28 waveguide ($\sim$0.1 dB/m) while much more power is collected by the WR28 waveguide. Consequently the actual lengths are a compromise among all this factor. Figure 4.4 shows a general layout of the CTF hall with the detection system above, after 1.6 m of concrete ceiling (for radiation protection).

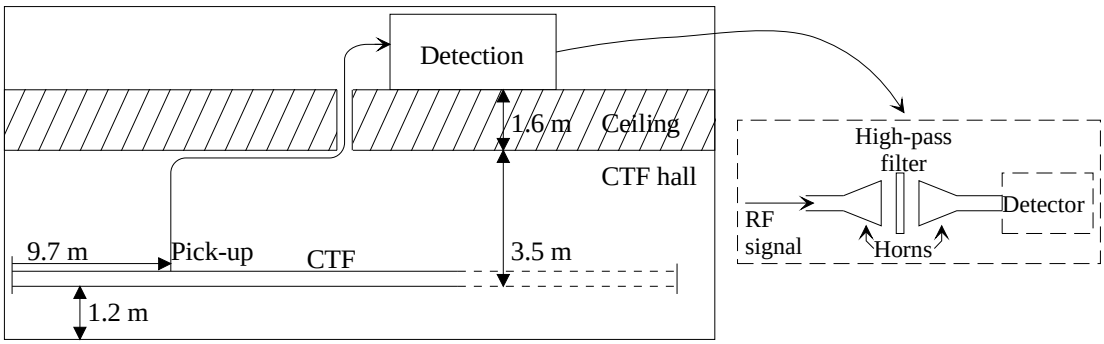


Figure 4.4: BLM set-up.

In Figure 4.5 is shown the actual installation of the RF pick-ups in the CTF drive beam. A Kapton$^{TM}$ foil was used to isolate the vacuum in the beam pipe, as indicated in the picture. For the WR12 waveguide this isolation proven to be enough but for the WR28 (with 4 times more surface) there was a small but continuous leak that spoiled the vacuum. In order to avoid this a two-step vacuum installation was set up, there are two Kapton$^{TM}$ foils and in between a special vacuum chamber which contains a piece of WR28 waveguide perforated with small holes to allow a vacuum pump to extract the air. This solution was very satisfactory concerning the vacuum quality but seems to slightly perturb the bunch spectrum signal travelling trough the waveguide.

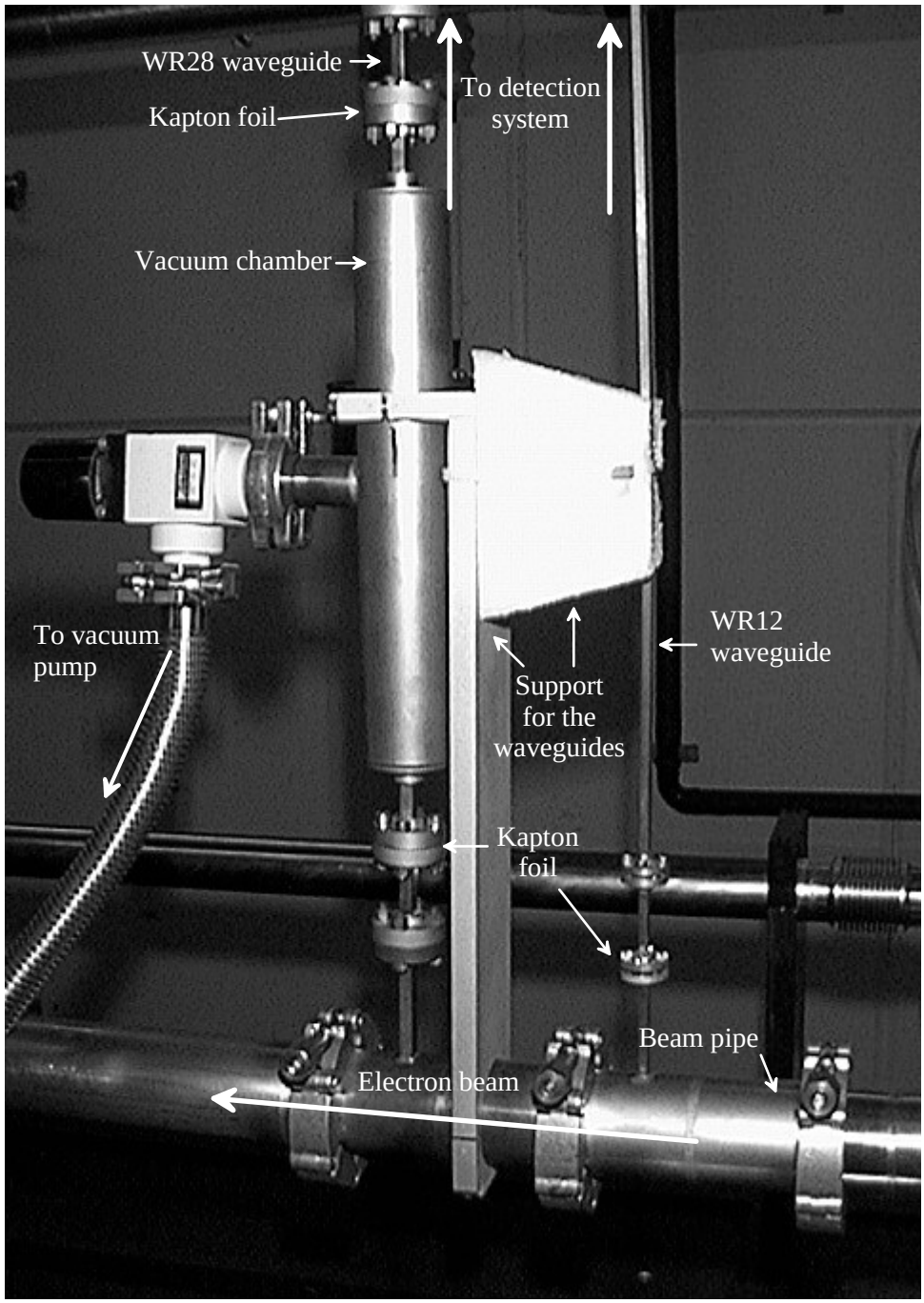


Figure 4.5: Picture of the RF pick-ups in the CTF drive beam.

## 4.4 Measurement and Data Acquisition Procedures

Two detection systems are currently in use, the diode detector with a set of high-pass filters and the two-mixers technique (see Chapter 3). In both cases the data acquisition is made with a PC, located in the CTF control room, using a GPIB (General Purpose Interface Bus) and specially built programmes. Several programs were written during the thesis work to help with the data acquisition and setting of the instruments. The programmes used for the data acquisition are written in C/C++ and make use of the SICL (Standard Interface Control Library) of Hewlett Packard to control and read out the oscilloscope and synthesizer.

### 4.4.1 Power detection

When detecting the signal with a diode detector the programme orders the oscilloscope to acquire the signal and send it back to the computer that will store the data as an ASCII file. The acquired signal can be one single sample or an average over several samples, the user can modify on-screen parameters to change those settings. Both signals, coming from the WR12 and WR28 waveguides, are acquired at the same time.

In Figure 4.6 are shown typical signals measured with a diode detector and a digitizing scope in both frequency bands ($K_a$: 26.5–40 GHz and E: 60–90 GHz). The two curves correspond to two different compressing ratios of the bunch compressor. A higher compression is translated into a larger amplitude of the signal. The higher the frequency measured the larger the increase in the amplitude, therefore this increase in amplitude is specially noticeable in the E band (as can be seen in the Figure 4.6 (b)) .

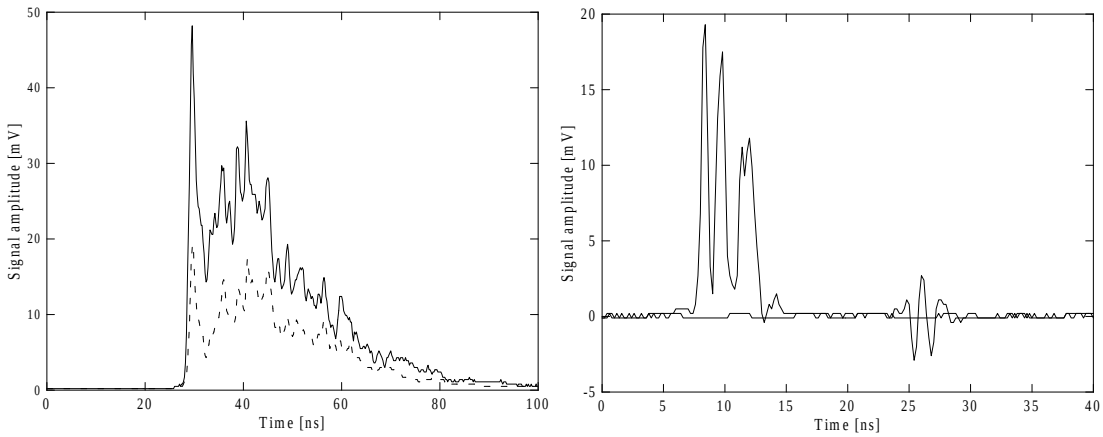


(a) $K_a$ band. (b) E band

Figure 4.6: Signal obtained with the diode detector in both frequency bands.

### 4.4.2 Two-mixers detection

The detection with two-mixers is a bit more complex, in Figure 4.7 is shown the process of the signal detection. The second mixer covers the range 2–18 GHz, so it has a maximum bandwidth of 16 GHz. In order to detect the whole E band (60–90 GHz), with a bandwidth of 30 GHz, it is necessary to split the signal in two. A high-pass filter (in transmission) with a frequency cut-off of 74.5 GHz let pass through the range 74.5–90 GHz that is collected by a horn, while reflects (as a low-pass filter) the band 60-74.5 GHz that is then collected by another horn. Both signals then follow the same process. The PC controls the oscilloscope acquisition and the sweeping oscillator (a HP synthesizer).

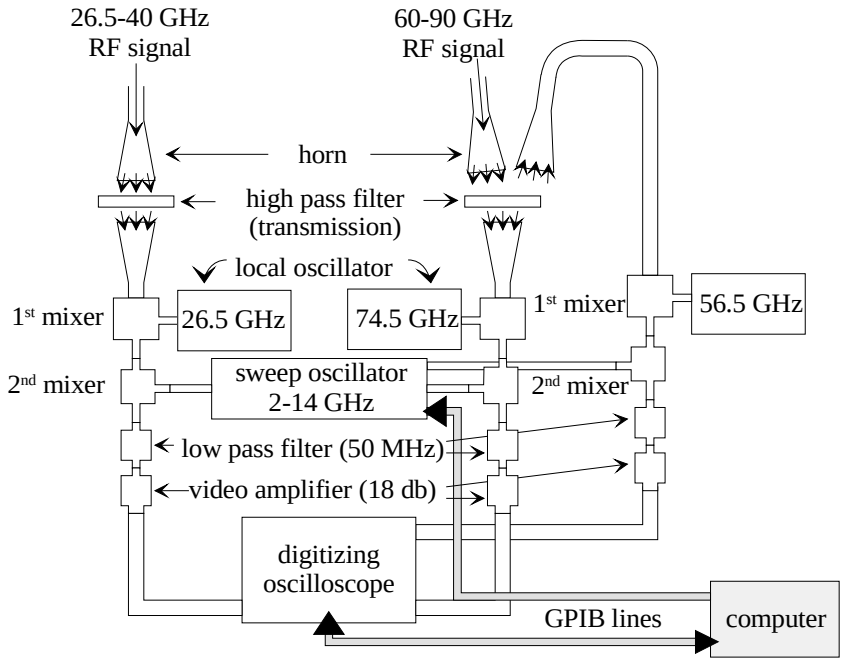


Figure 4.7: Computer control of the two-mixers detection system.

The measurement and acquisition process can be divided in several steps,

1. The PC orders the synthesizer to oscillate at a certain frequency.

2. The oscilloscope is ordered to start the acquisition (in envelope mode) averaging over several samples.

3. The oscilloscope sends the data to the computer.

4. The computer processes the data and stores the result.

5. The process starts again until the desired frequency range is covered.

Finally the computer will give the frequency spectrum of the incoming signal. Figure 4.8

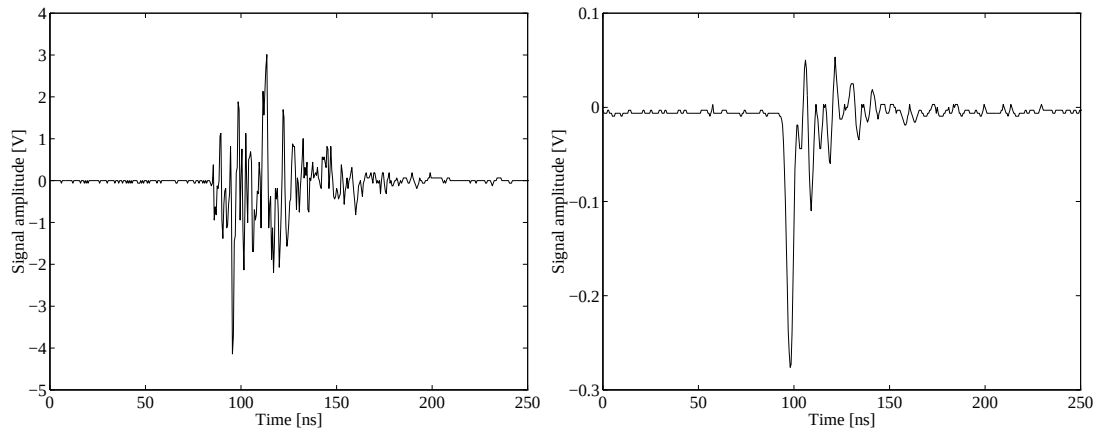


(a) Signal at 30 GHz (b) Signal at 60 GHz

Figure 4.8: Signal read out by the scope after the mixing procedure at two different frequencies

shows the signal read out by the scope after the mixing procedure (step 2 of the acquisition process) at two different frequencies. Due to the fact that the LO is not synchronous with the bunch, the LO signal has always a different phase with respect to the incoming RF signal (generated by the bunch), a direct average over several acquisitions after mixing would give a zero amplitude signal. Hence, the scope is set to "envelope mode", in this way it records the maximum amplitude at each time-point for each acquisition. The resulting signal will be the envelope of several superimposed signals. The number of signals necessary to obtain a good average was determined empirically by observing when the envelope of the superimposed signals became stable. That number was restricted by the need of keeping the measurement time as short as possible (not longer than a few minutes). Then the area of this signal is computed and used as the level of the signal at the corresponding frequency (step 4 of the acquisition process). This procedure is applied until the whole frequency range is covered so that the final result is the frequency spectrum of the signal as shown in Figure 4.9, for a single bunch, and in Figure 4.10 for a train of bunches.

The acquisition program allows the user to easily change most of the parameters that control the data acquisition as the number of averages, the frequency range or ranges and the frequency step. Another programs were written to be able to change the oscilloscope and synthesizer settings from the control room (vertical and horizontal ranges, acquisition mode, etc.).

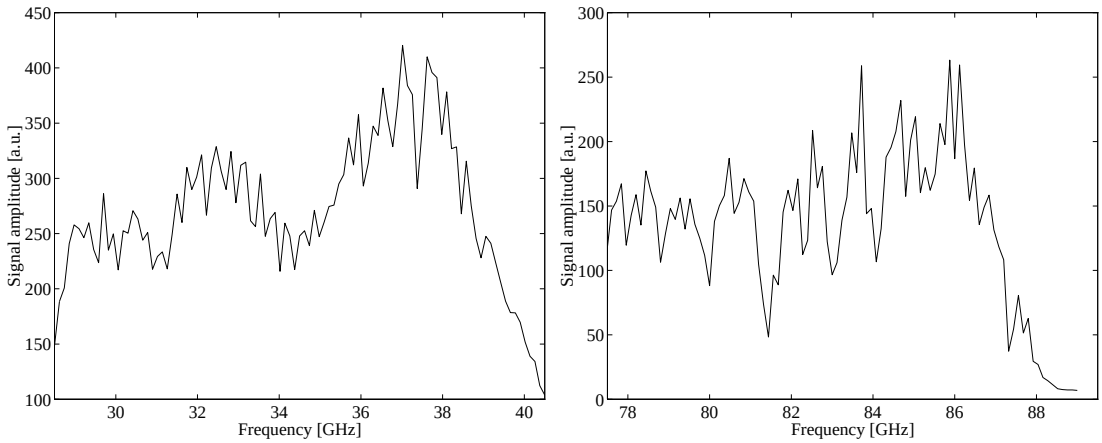


(a) $K_a$ band. (b) E band

Figure 4.9: Raw frequency spectrum for a single bunch.

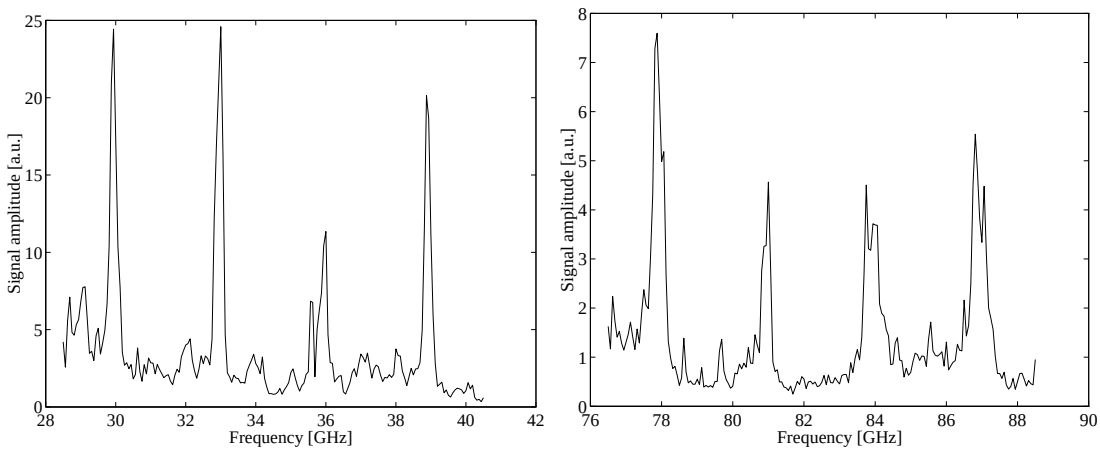


(a) $K_a$ band. (b) E band

Figure 4.10: Raw frequency spectrum for a train of bunches.

A calibration of the system is needed in order to deduce the bunch length from the data obtained by both methods. The calibration procedures are described in detail in the next chapter.

The next figures show the real installation of the mixing method in the CTF gallery. Figure 4.11 shows an overview of the whole installation in a rack, with the power supplies, the synthesizer that is used as sweeping oscillator, the digitizing scope and the $K_a$ and E band processing.

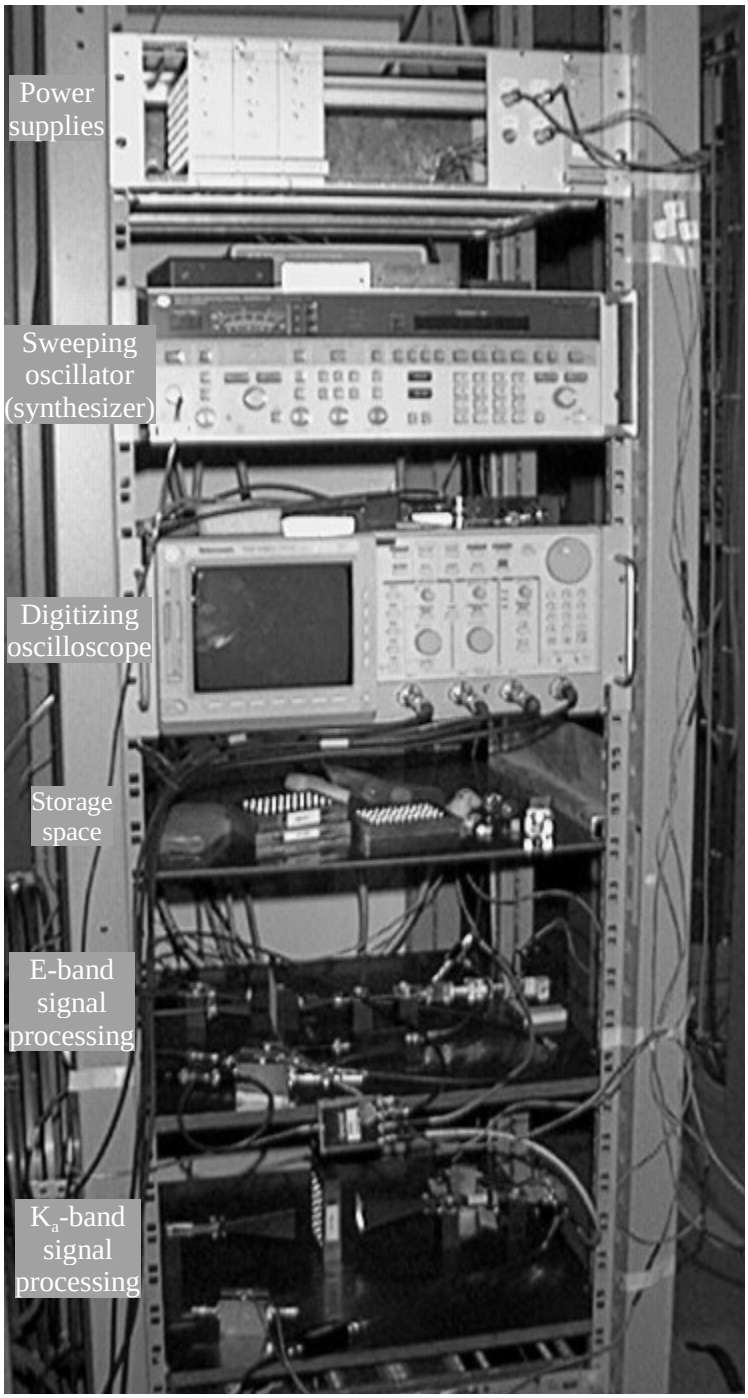


Figure 4.11: Overview of the detection system.

Figure 4.12 shows the set-up to measure the $K_a$ band in the frequency range: 28.5–42.5 GHz) and Figure 4.12 shows a closer view of the $K_a$ band mixers.

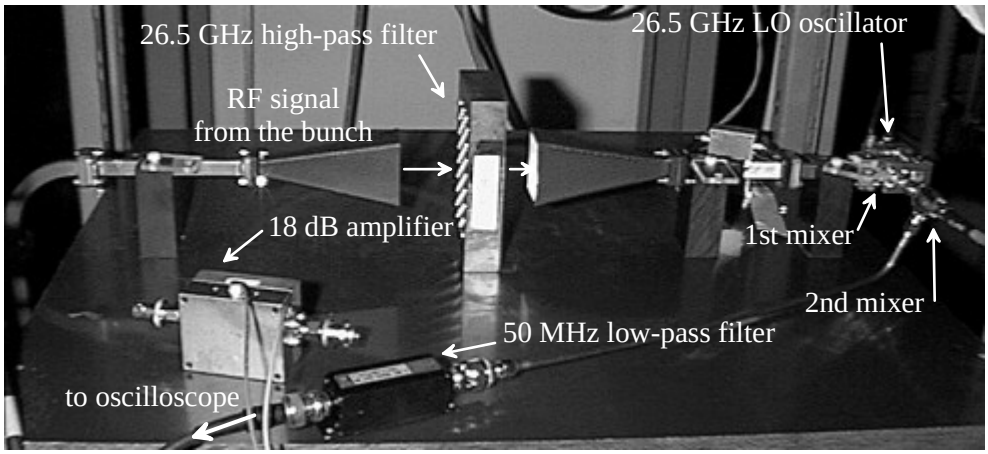


Figure 4.12: View of the $K_a$ band processing set-up.

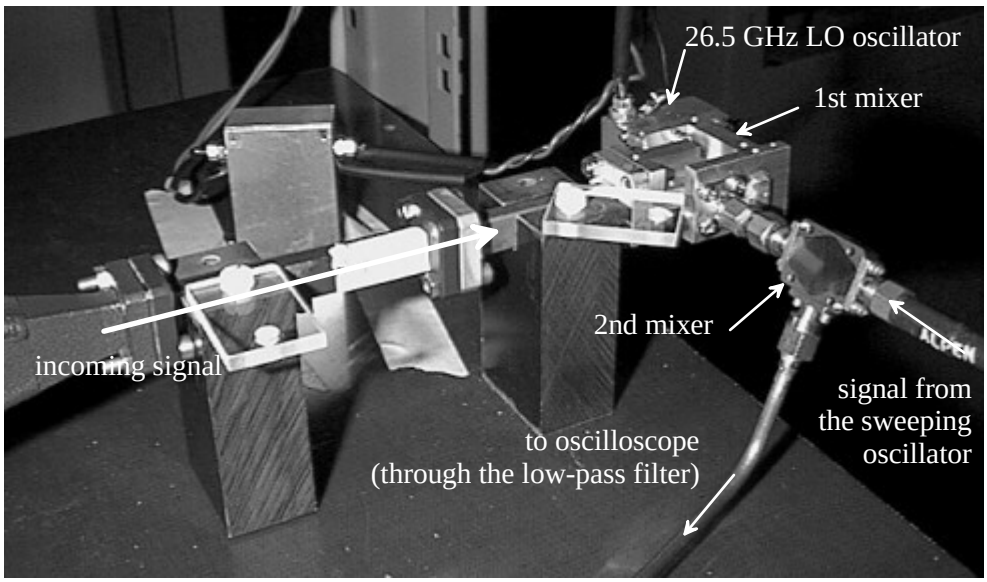


Figure 4.13: Closer view of the $K_a$ band mixers.

Figure 4.14 shows a general view where it is possible to see the set-up of the two processing areas for the E band. The filter that acts as a high-pass filter in transmission and as a low-pass filter in reflection allows the division of the E band in two parts.

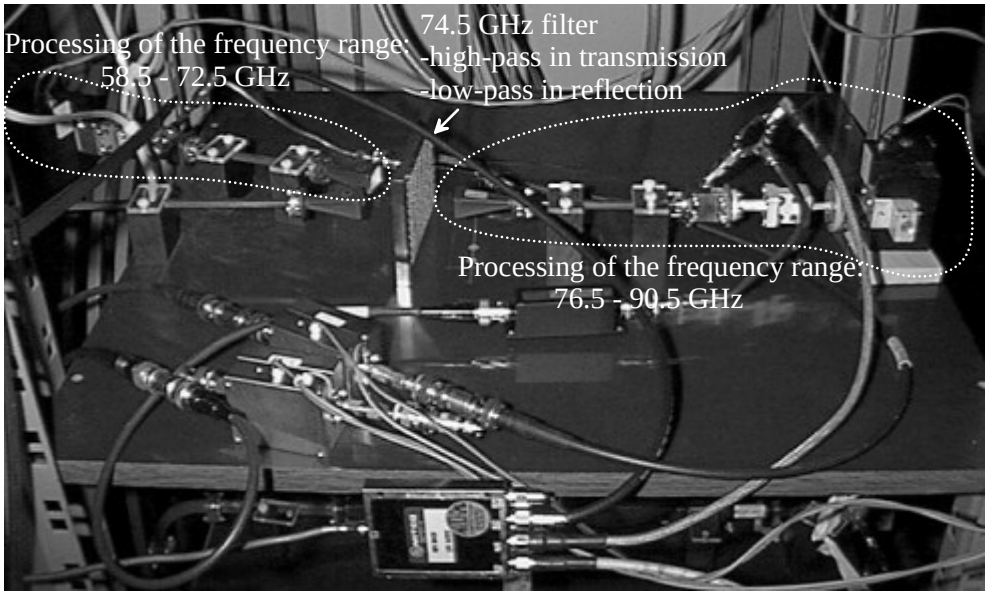


Figure 4.14: View of the E band processing.

In Figure 4.15 is shown in detail the set-up to process the frequency range 76.5–90.5 GHz of the E band. A closer look of the E band mixers can be seen in Figure 4.16.

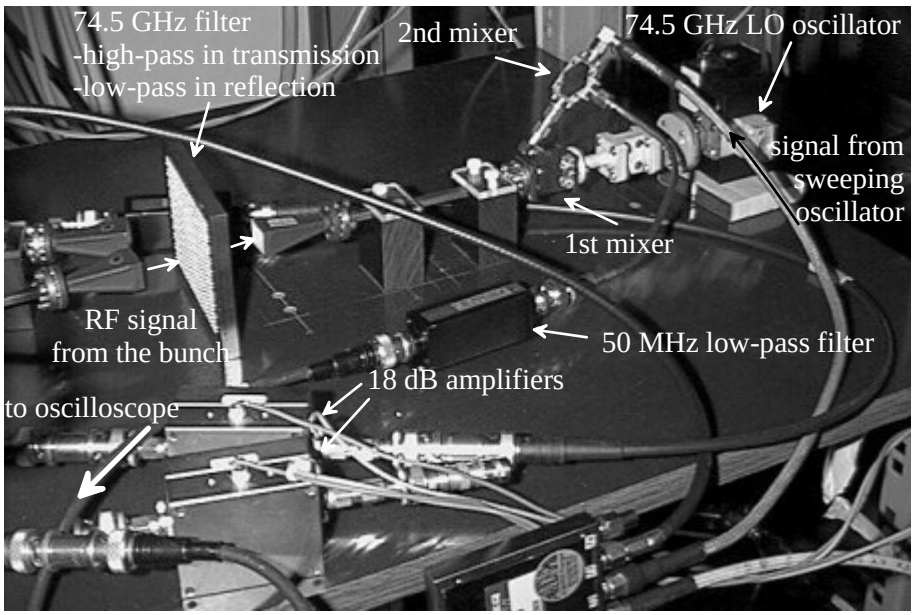


Figure 4.15: View of the set-up to process the frequency range 76.5–90.5 GHz.

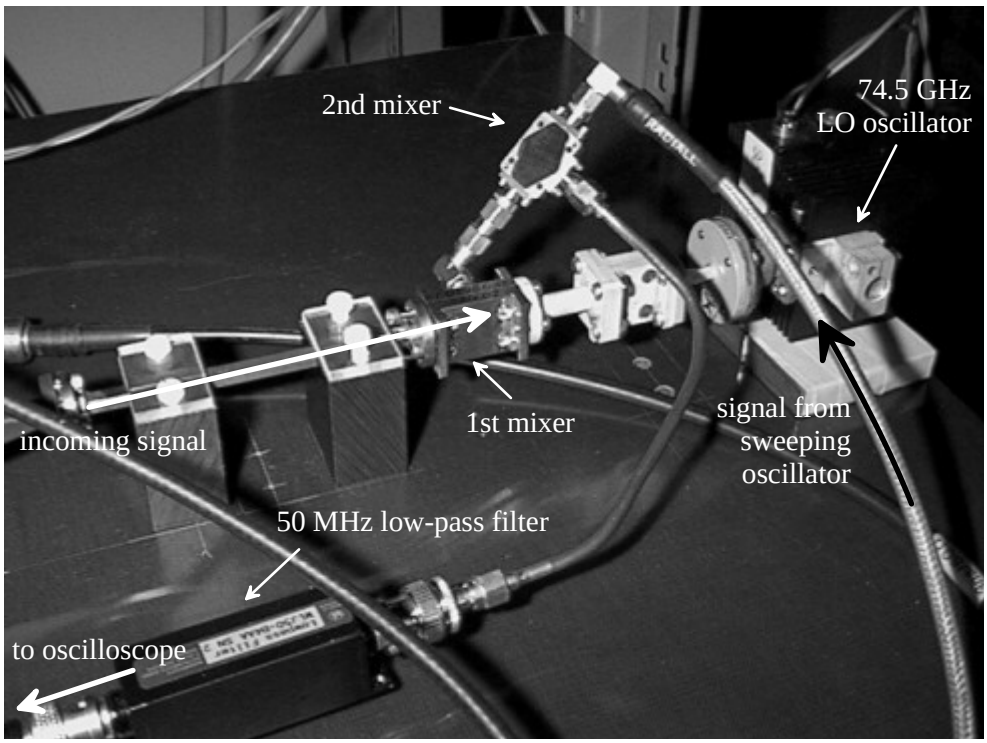


Figure 4.16: Closer view of the E band mixers.

# Chapter 5

# Data Analysis and Results

This chapter presents the experimental results and their analysis. The two detection techniques, power detection with a diode and RF mixing, follow different data processing techniques. Pictures and plots of the curves obtained during the experiments, using both detecting techniques (the diode and the mixing method), are shown together with plots of the expected signal coming from computer and analytical calculations. These figures will also show how the signal changes when compressing the bunch, and how this effect is particularly visible, as expected, for the higher frequencies.

The analysis of the experimental signal include the comparison with the expected signal, the understanding of unexpected effects, and a discussion of calibration procedures for both systems. Several plots will show the experimental results of the calibration procedures for both detection techniques.

## 5.1 Data from the Diode Detector

The diode detector measures the power of the incoming electromagnetic wave. Due to dispersion in the waveguides this signal is spread out in time, high frequencies arriving first. A series of high pass filters, with different cut-off frequencies, can be used to measure the signal in different frequency ranges and then reconstruct the frequency spectrum from these data. However, this method did not work because it was not possible to calibrate the whole system, that is, to know its frequency response. Nevertheless, the diode detector was successfully used to monitor variations in the bunch length and set-up the bunch compressor. A relative calibration method, using the bunch length measurements given by the streak camera was tried, but since the streak camera has a resolution of 2 ps rms the resulting calibration was not accurate enough.

### 5.1.1 Expected Signal

In order to have an estimate of the signal arriving at the diode, one has to make use of the frequency response of the RF pick-ups, obtained with the help of MAFIA, and analytical expression for the bunch shape and the dispersion and attenuation in the waveguide. These effects are frequency dependent, therefore it is necessary to work in Fourier space and once the final result is obtained transform it back to time space using an Inverse Fast Fourier Transform (IFFT). The process is as follows,

$$R(\omega,z,\sigma) = r(\omega) \times Dispersion(\omega,z) \times Attenuation(\omega,z) \times Bunch\,spectrum(\omega,\sigma)$$

$$\Longrightarrow \qquad p(\omega,z,\sigma) = \frac{R(\omega,z,\sigma)}{\sqrt{Z(\omega)}} \qquad \stackrel{IFFT}{\Longrightarrow} \qquad p(t,z,\sigma)$$

$$\Longrightarrow \quad \text{Expected Power: } P(t,z,\sigma) = |p(t,z,\sigma)|^2$$

where $r(\omega)$ is the frequency response of the pick-up, $R(\omega,z,\sigma)$ is the bunch spectrum after travelling a distance $z$ in the waveguide, $Z(\omega)$ is the waveguide impedance and $p(\omega,z,\sigma)$ is the function which inverse Fourier transform squared gives the signal power, $P(t,z,\sigma)$. The resulting power amplitude depends, not only on the time, but also on the distance travelled in the waveguide $z$ and the bunch length. In all this process only the first mode ($TE_{10}$) is taken into account, as is the only mode propagating in the frequency range that is measured. Moreover the power that is coupled to the other modes is negligible compared to the power carried by the first mode.

Figures 5.1 and 5.2 show the expected signals, in the $K_a$ and E band respectively, for a gaussian bunch after travelling through 8 m of waveguide, for four different bunch lengths. The signal amplitude increases when reducing the bunch length because the shorter the bunches the more important is the excitation of the high frequency part of the spectrum. The increase of the signal when reducing the bunch length is particularly clear in the E band (60–90 GHz), where for the longest bunch the level of the signal is almost zero, while it increases very fast for very short bunches. The increase in the maximum level when shortening the bunch length is shown in Table 5.1.

| | $K_a$ band | E band |
|---|---|---|
| from 3.5 ps to 2.5 ps | 42% | 356% |
| from 2.5 ps to 1.5 ps | 26% | 177% |
| from 1.5 ps to 0.5 ps | 12% | 71% |

Table 5.1: Increase of signal level when shortening the bunch length.

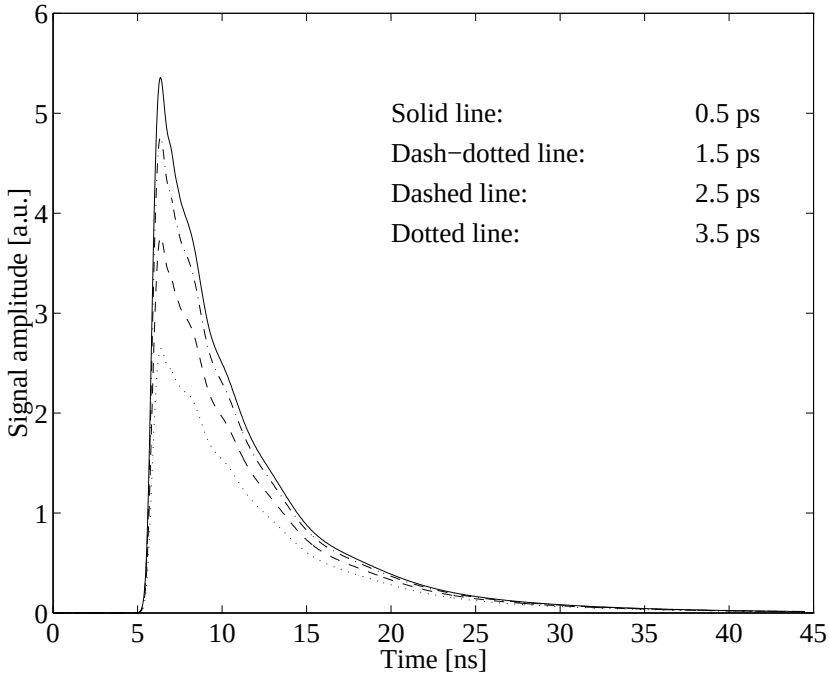


Figure 5.1: Expected power arriving to the diode detector in the $K_a$ band.

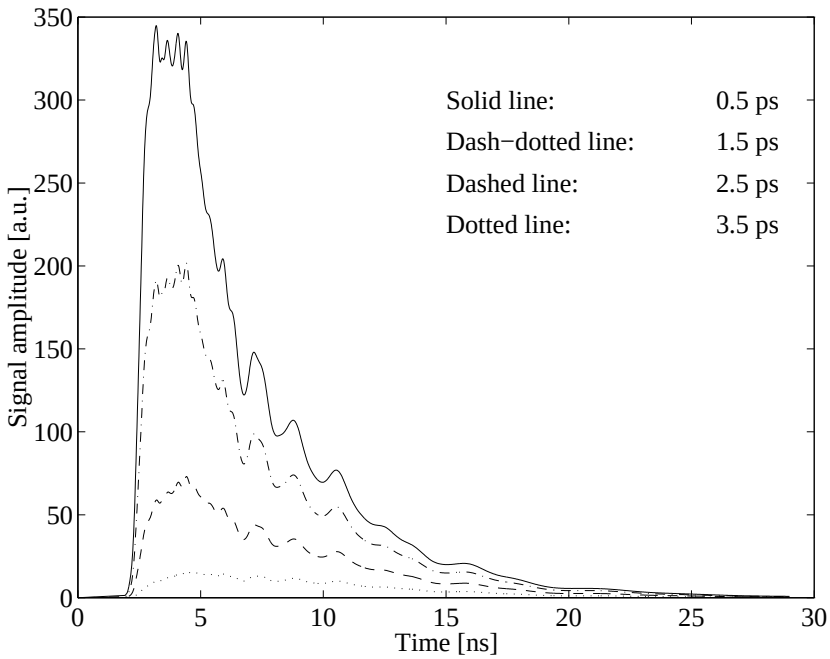


Figure 5.2: Expected power arriving to the diode detector in the E band.

The dispersion in the waveguides modifies the speed of transmission of the signal according to its frequency. The high frequencies travel faster than the low frequencies, hence they arrive first to the detector. In Figure 5.3 are shown the power amplitude after 8 and 16 m of waveguide, the attenuation in the waveguide has reduced the amplitude of this signal and a amplifying factor has been use to make both signal of the same height in order to see the stretching effect due to dispersion.

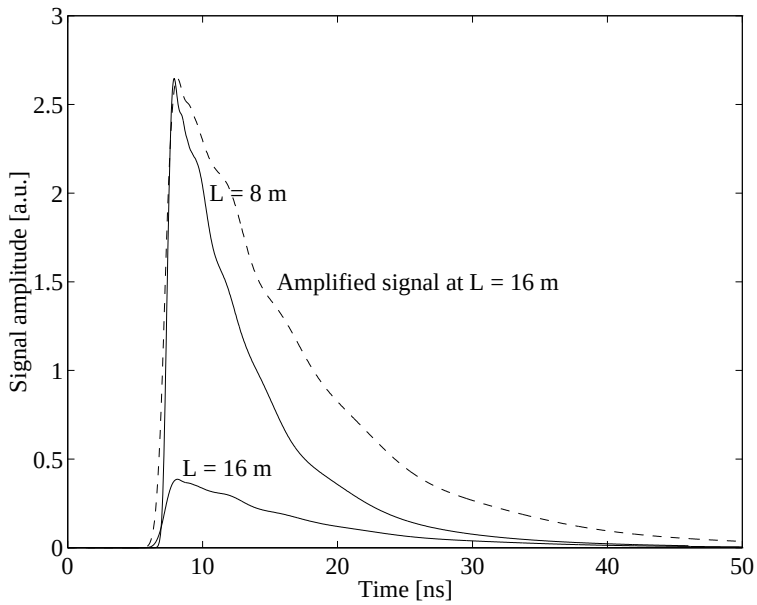


Figure 5.3: Signals after 8 and 16 m of waveguide.

### 5.1.2 Experimental Results

The first measurement with the diode detector was made the 5th October 1996, the signal is shown in Figure 5.4. At this time the horns were not installed, the diode was directly connected to the end of the waveguide. Is is noticeable, comparing this plot with the one for the expected signal (Figure 5.1) that it seems to be a superposition of the same signal with some time delay.

The main signal starts at 8–9 ns while this superimposed part starts around 10 ns later. After some tests part of this signal was proven to come after the passage of the beam through the TCM (see Chapter 4). At the time this measurement was done the TCM was around 1.5 m behind the RF pick-up, so that the beam would take 5 ns to reach this element and then the reflected RF signal 5 ns more to reach the RF pick-up. In order to test the influence of this element in the detected signal, several measurements

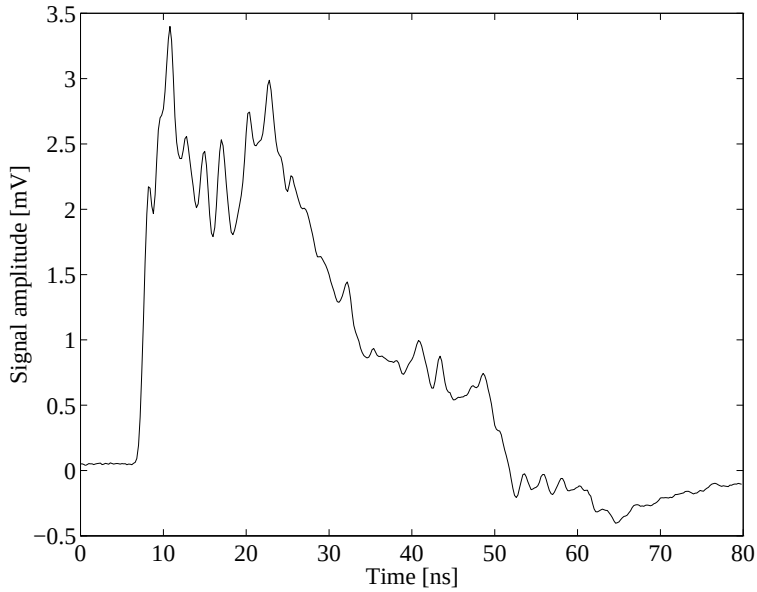


Figure 5.4: First signal measured with the diode detector.

were performed with the aluminium or sapphire sheet in the beam line and out of the beam line. When the sheets were in, the reflected signal level was much larger, while with the sheets out, the level of this part decreased but never disappeared, that is because the TCM cavity alone disturbs the bunch field producing some backwards reflected RF field. In Figures 5.5 are plotted the curves obtained with the TCM in and out of the beam line. The fact that part of the signal is generated in the TCM is specially noticeable with the use of a 35 GHz high-pass filter as shown in Figure 5.6.

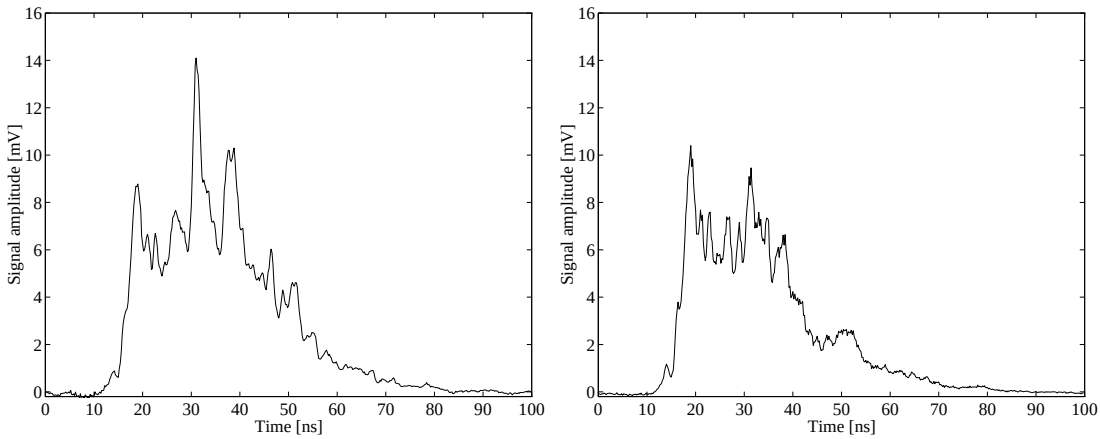


(a) TCM in. (b) TCM out.

Figure 5.5: Power curves with no high-pass filter.

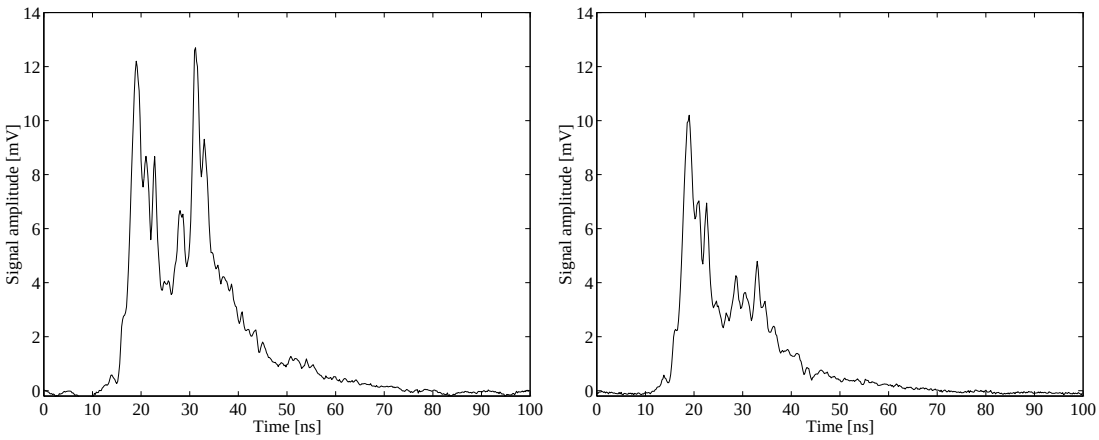


(a) TCM in. (b) TCM out.

Figure 5.6: Power curves with a 35 GHz high-pass filter.

Although the detection system is not calibrated it is possible to compare qualitatively the expected signal and the real signal by using a calibration factor (the ratio of maximum amplitudes) that makes both signal have the same maximum value. Figure 5.7 shows the experimental signal against a theoretical signal with an arbitrary calibration factor. In order to simulate the signal reflected form the TCM, the theoretical signal is superimposed to itself with a time delay of 10 ns.

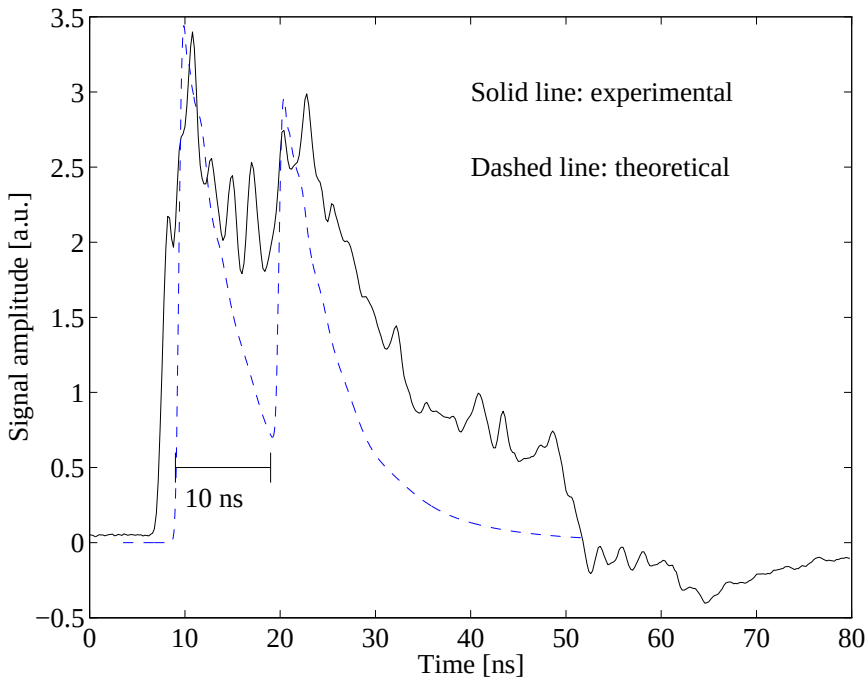


Figure 5.7: Comparison of expected to measured signal.

After these experiments the RF pick-up were move backwards so that the TCM was 1 m further away and the reflected signal would have an additional delay of 6 ns. It was not possible to place the RF pick-up in a better position due to a lack of space in the CTF beam line.

The current set-up of the Bunch Length Monitor (see Chapter 4) uses a horn to spread out the signal coming from the bunch and another horn to collect the signal after passing through a high-pass filter, this new configuration added some distortion to the signal. The horns were added not only to use the high-pass filters but also to provide a galvanic isolation for the diode since the first time the diode was used, without the horns, it was broken after a few minutes. This incident was thought to be caused by some current flowing through the waveguide from the beam pipe. Another element added to the transport line was a pumping section for the $K_a$ band (see Chapter 4), that also contributes to distort the signal. Typical signals obtained with the current set-up are shown in Figure 5.8 for the $K_a$ band and in Figure 5.9 for the E band. The different lines correspond to different compression settings, that is different bunch lengths, that are indicated by the current in the compressor end magnets.

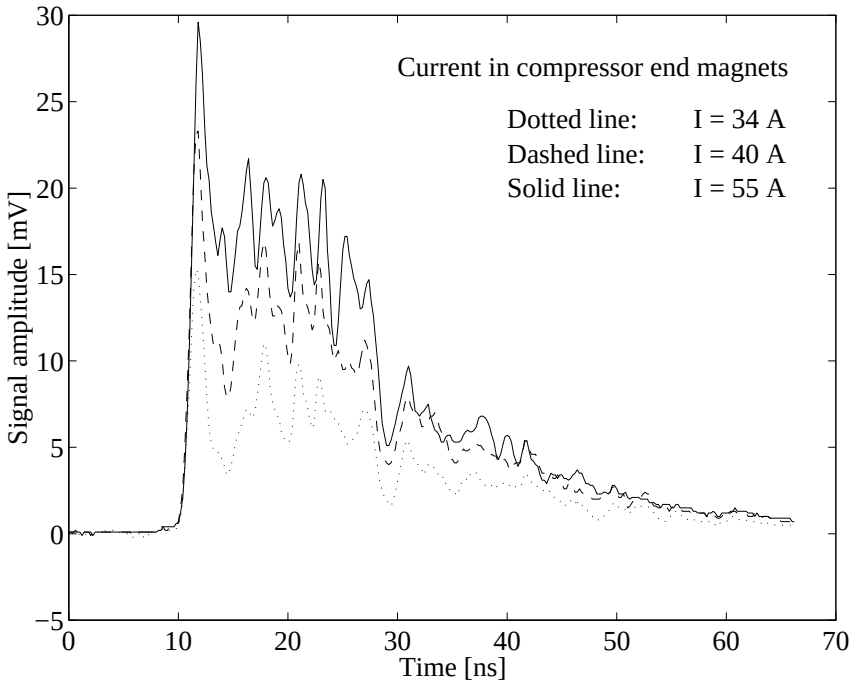


Figure 5.8: Signal measured with a diode detector in the $K_a$ band.

The signal shape is similar for different bunch lengths but the amplitude level increases as the bunch gets shorter, as expected. Because the diode detector measures power, the result is very sensitive to a variation in charge (power goes with the square

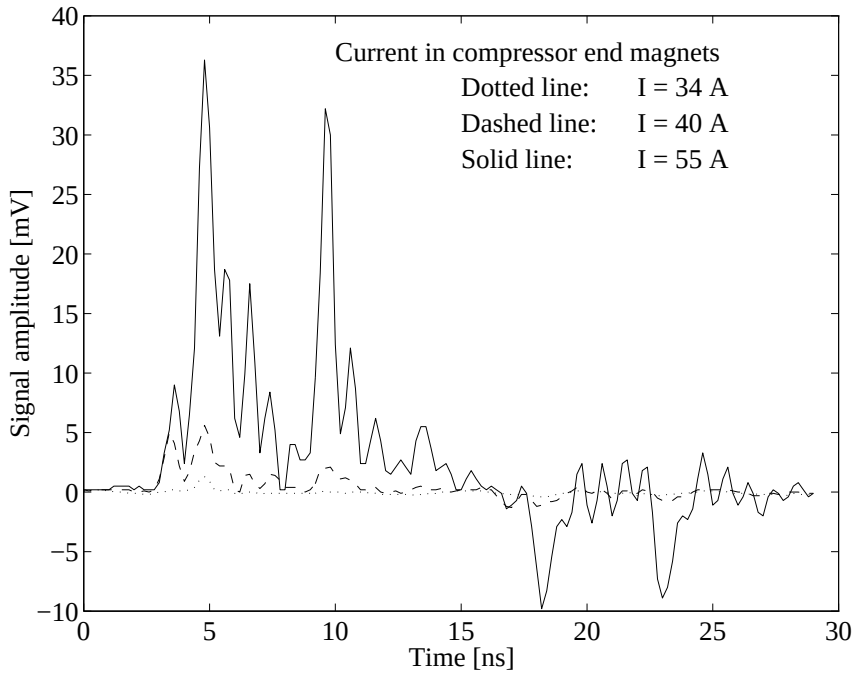


Figure 5.9: Signal measured with a diode detector in the E band.

of the charge), therefore either the charge of the bunch is kept very stable or it has to be measured for every shot to normalise the results.

The signals shown in these figures differ from the theoretical expected signals (Figure 5.1 and 5.2). At least the first part of the signals look similar to the expected, but later there are, apparently, some reflections adding to the signal. One of this reflection has been identified, in the $K_a$ band, as coming from the TCM, but there are some other signals coupled in the waveguide or even generated somewhere in the waveguide. At this high frequencies metallic surfaces act as mirrors so that is possible that some resonances are formed somewhere in the system.

In the E band some resonances are interfering with the main signal so that it looks distorted by rippling and there is clearly a reflection coming 5-6 ns after the initial signal. That reflection is generated in a vacuum pump that is installed 95 cm after the E band RF pick-up, that would make a delay of 6 ns for the signal reflected at this point. However that could not be tested because it was not possible to remove the vacuum pump. These same measurements were made using a 40 GHz and a 80 GHz high-pass filter in the $K_a$ and E band respectively, the results are shown in Figures 5.10 and 5.11. The reflection following the main signal in the E band has completely disappeared and in the $K_a$ band also part of the signal coming about 20 ns behind the main signal has vanished, thus they were composed of frequencies below 80 GHz and 40 GHz respectively.

In conclusion, it was difficult to analyse the signal coming from the bunch due to the coupling of signal reflected inside the beam pipe and the appearance of resonances (mainly due to the use of horns and the pumping chamber).

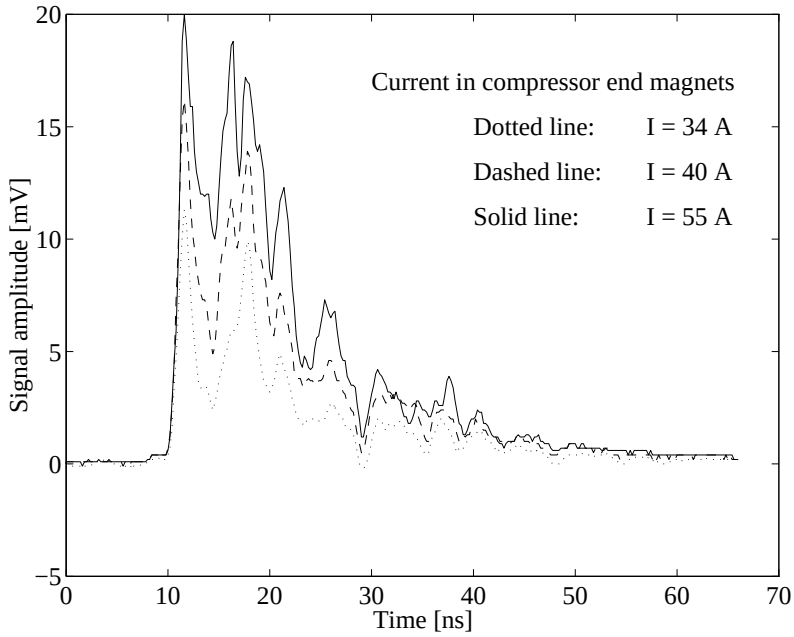


Figure 5.10: Measured power in the $K_a$ band with a 40 GHz high-pass filter.

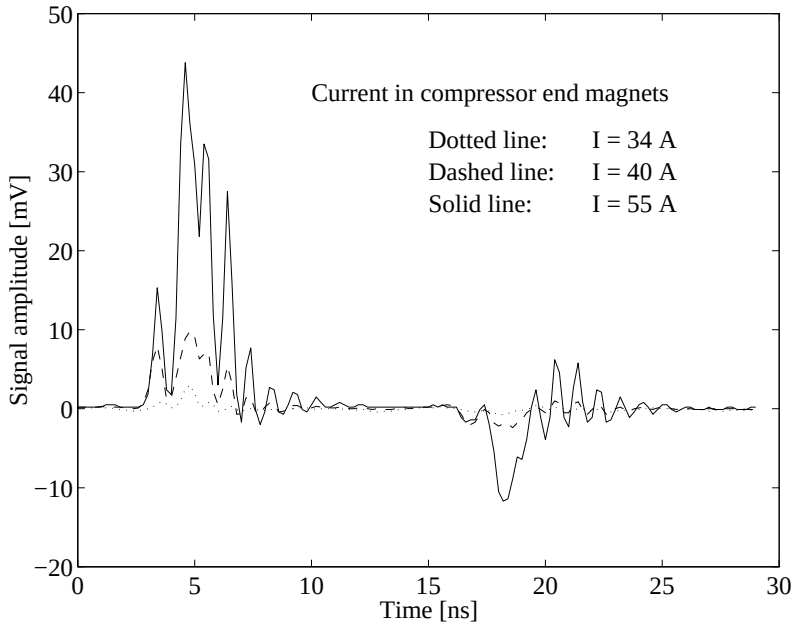


Figure 5.11: Measured power in the E band with a 80 GHz high-pass filter.

With this method is very difficult to measure the bunch length for a train of bunches due to interference effects among the signals for each bunch in the train, that are spaced by 0.333 ns in time. Figures 5.12 and 5.13 show the power detected from a train of 8 bunches in the $K_a$ band.

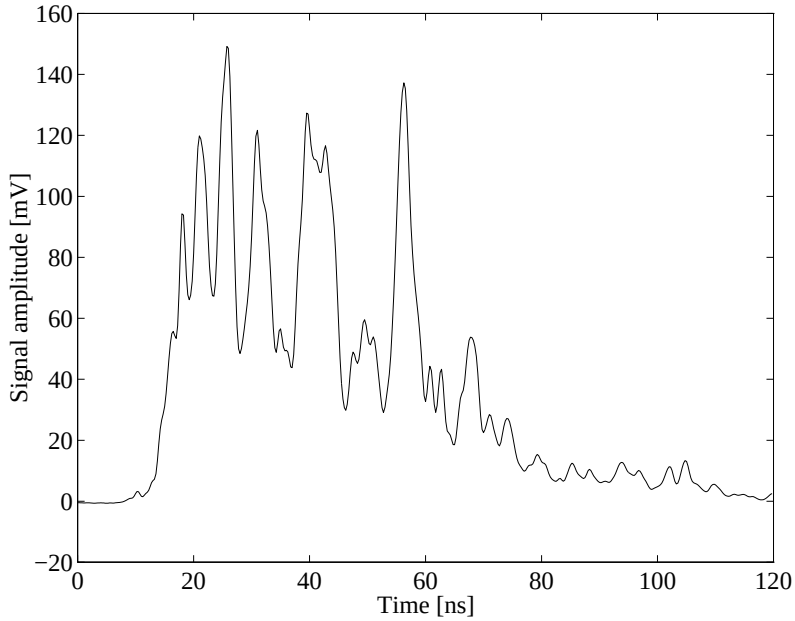


Figure 5.12: Power detected from a train of 8 bunches without high-pass filter.

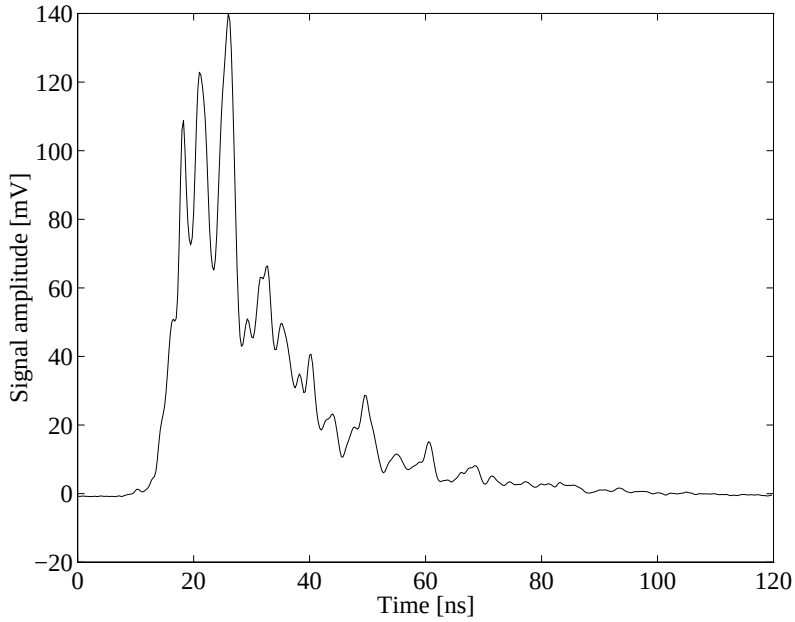


Figure 5.13: Power detected from a train of 8 bunches using a 35 GHz high-pass filter.

It was not possible to properly calibrate this set-up due to a lack of the necessary equipment, instead a calibration relative to the streak camera was tried, as explained in the next section.

### 5.1.3 Relative Calibration

An independent calibration procedure, based on the individual calibration of all the components of the system, failed as a consequence of not having the proper equipment. The filters characteristics, for example, could only be measured, with a network analyzer, in the frequency range 50 MHz–40 GHz. That implies that the frequency response of filters with a higher cut-off frequency have to be inferred from the response of those filters that were within the network analyzer frequency range. Some other components, as the diode detector, could not be properly calibrated as there was no microwave source with enough output power available.

As an alternative a calibration relative to the streak camera measurements was used. For different set-ups of the bunch compressor the bunch length was measured using the streak camera and at the same time the signal from the diode detector was recorded. Assuming a Gaussian bunch, the peak amplitude of the signal (supposed to be at 40 GHz for the Ka band and 90 GHz for the E band) is correlated with the form factor given by the bunch length measured with the streak camera. A regression line is found for the values of the peak amplitude against the form factor square. However the streak camera is known to have a resolution of about 2 ps rms and any calibration using the results obtained with that device will not be very accurate. Figures 5.14, 5.15 and 5.16 show some experimental results of the calibration procedure in both frequency bands.

This calibration seems to work fine for the $K_a$ band in Figure 5.14, although there are two points, at 40 and 48 A, where the streak camera measurements where wrong. At 40 A the length measured is larger than on both sides while at 48 A it is much smaller, and in both cases the errors bars are significantly smaller than in the neighbour points. This could have been caused by a transverse shift of the beam in the TCM.

In Figure 5.15 both bands are calibrated, but because the E band is much less sensitive to long bunches not all point are used in the calibration but only the measurements which bunch length is less than 4 ps rms. The $K_a$ band follows the same behaviour than in the previous plot and the E band shows a better sensitivity to shorter bunches and a saturation for long bunches. The observed behaviour, in the E band, is expected as long bunches do not excite high frequencies, hence there will be no signal excited in this band.

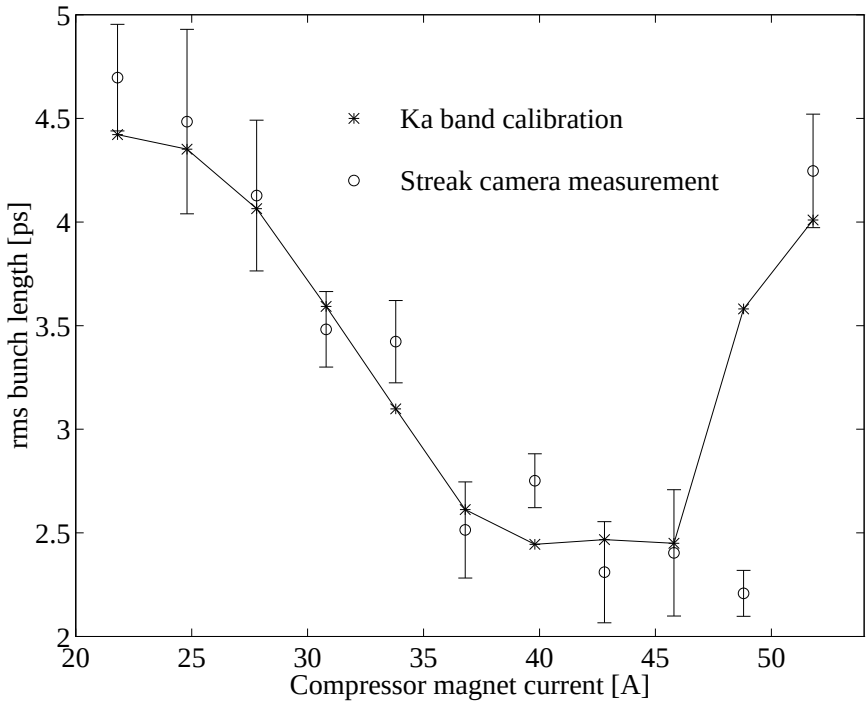


Figure 5.14: Calibration result for the $K_a$ band.

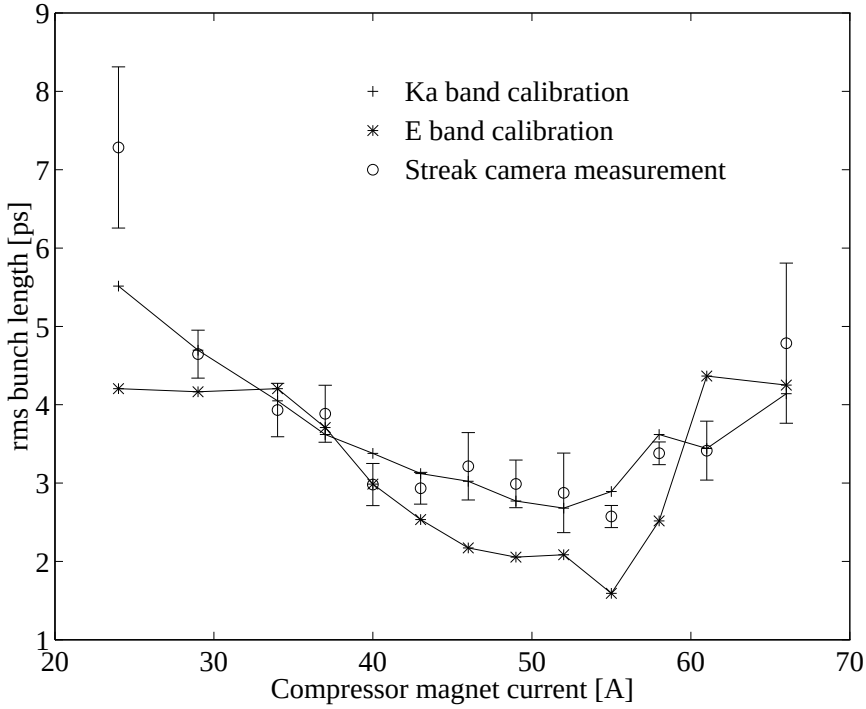


Figure 5.15: Calibration result for the $K_a$ and E band.

Figure 5.16 shows a calibration that was done with very short bunches only, in this case the results from the streak camera are doubtful, they show a minimum length at 46 A while the detection of power shows in both bands a minimum length (a maximum signal level) at 42 A.

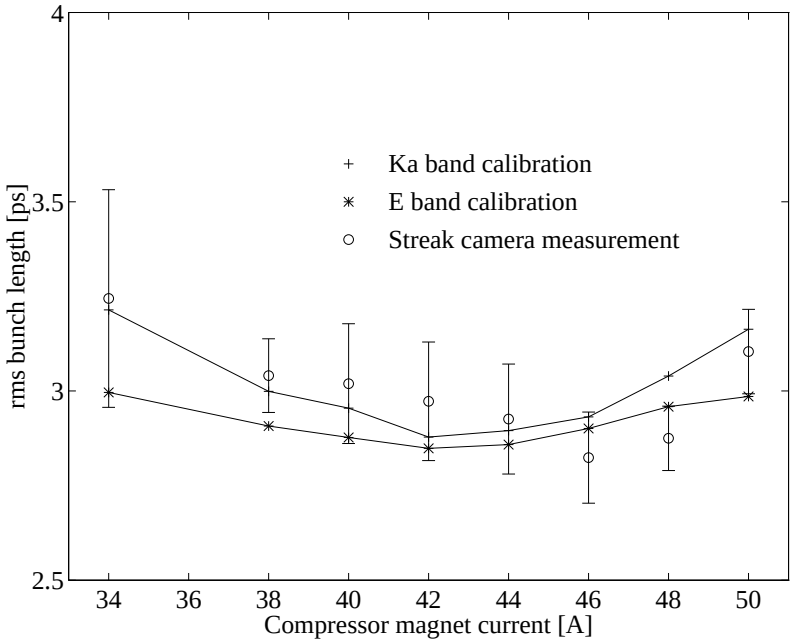


Figure 5.16: Calibration result for the $K_a$ and E band.

With this method single shot measurements of the signal are obtained. Thus, the diode detector proved to be a very useful to obtain fast qualitative information of the variation of the bunch length. However, it is not well adapted to quantitative bunch length measurements because of the difficulties to obtain an absolute calibration.

## 5.2 Data from the Mixing Method

With the mixing technique it has been possible to measure the frequency spectrum of a train of bunches as well as of a single bunch. Moreover, a method was found to obtain the frequency response of the system, that is an absolute calibration. By applying this method the mixing technique was successfully calibrated and was able to measure bunches as short as 0.7 ps. However, the calibration is still a lengthy procedure and has to be repeated whenever any modification in the set-up changes the frequency response of the system.

### 5.2.1 Expected Signal

The process to calculate the signal expected is similar to the one used for the diode detector. The results obtained for the frequency response are multiplied by the attenuation and a gaussian bunch spectrum. Also the frequency response of some elements was taken into account, some of the mixers, for example, have a calibration delivered by the company which produces them. However there are some elements that could not be calibrated so that the signal obtained can only give an approximate idea of the expected signal. In Figures 5.17 and 5.18 are shown the expected frequency spectra of a single bunch and a train of bunches, respectively, for different rms bunch lengths.

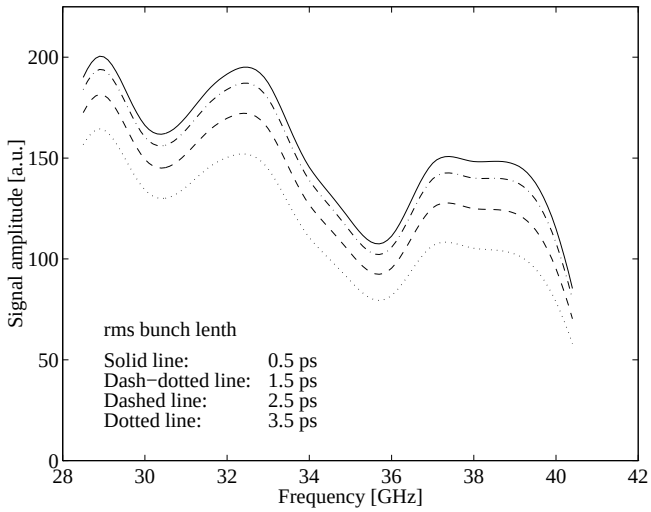


(a) $K_a$ band.

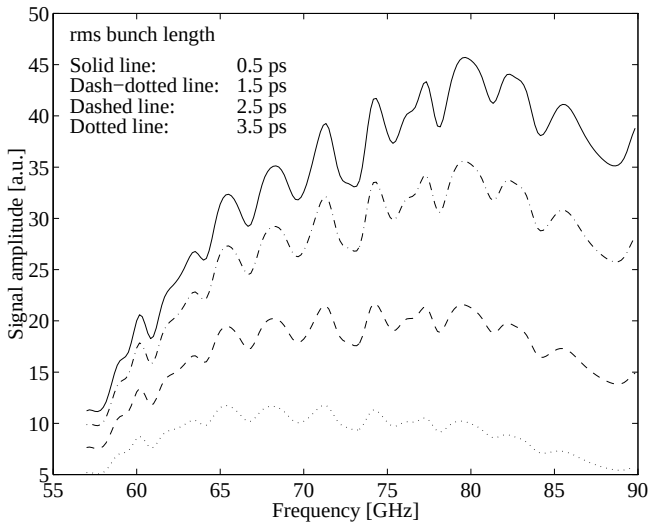


(b) E band.

Figure 5.17: Expected frequency spectrum of a single bunch.

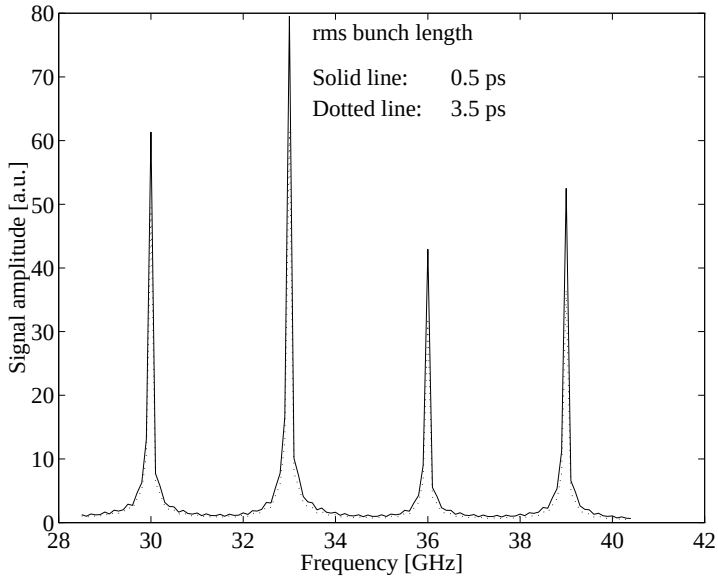


(a) $K_a$ band.

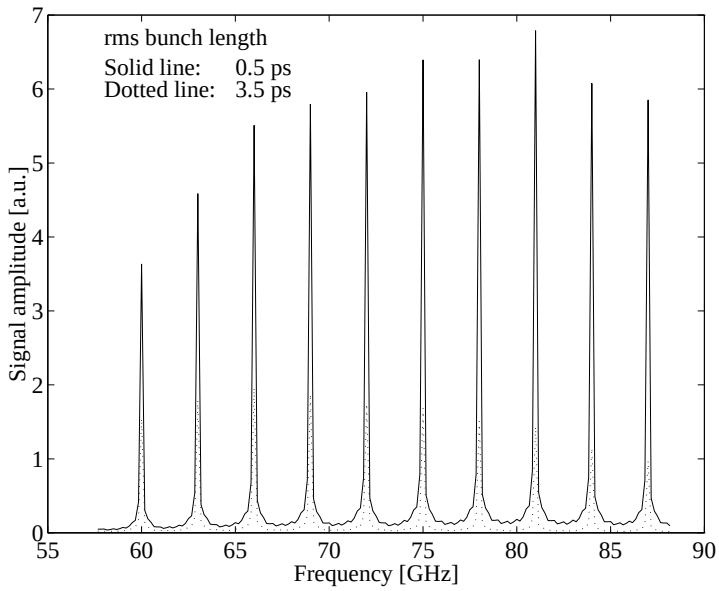


(b) E band.

Figure 5.18: Expected frequency spectrum of a train of 16 bunches.

It is difficult to observe the change in amplitude with bunch length for a train of bunches but the envelope of that spectrum is the same than for a single bunch so that the variation of amplitude level is also the same. The variation of the signal level for different lengths is listed in Table 5.2. Comparing these values with the values for the power detection (Table 5.1), it is seen that the increase of signal level when the bunch gets shorter is less pronounced. This technique measures the square root of power,

therefore the increase is smaller. However, the signal is directly proportional to the charge so that is less sensitive to variations in the charge of the bunch than the power detection.

| | at 40 GHz | at 87 GHz |
|---|---|---|
| from 3.5 ps to 2.5 ps | 21% | 99% |
| from 2.5 ps to 1.5 ps | 13% | 58% |
| from 1.5 ps to 0.5 ps | 6% | 26% |

Table 5.2: Increase of signal level with the bunch length at different frequencies.

### 5.2.2 Experimental Results

First of all, and in order to show how the mixing system works, some plots showing the behaviour of the system using a network analyzer as a RF source are presented. The network analyzer, which is able to cover the frequency range 50 MHz–40GHz, was coupled just before the first mixer and set to oscillate at several different frequencies. The resulting signals for the network analyzer oscillating at 30, 34 and 38.5 GHz are shown in Figures 5.19(a) 5.19(b) and 5.19(c) respectively. The lines indicating the frequency of oscillation are clearly visible in all cases, demonstrating that the system performs correctly and can be considered as a satisfactory spectrum analyzer. It is also visible a background signal and some noise in the form of small lines appearing at different frequencies. However, the noise is a cw signal and can be suppressed by a dedicated routine when processing the data. This routine was not used to obtain these because it would have also suppressed the cw signal generated by the network analyzer. Anyhow, the noise suppressing routine was implemented and in use during the experiments performed with the CTF drive beam bunches.

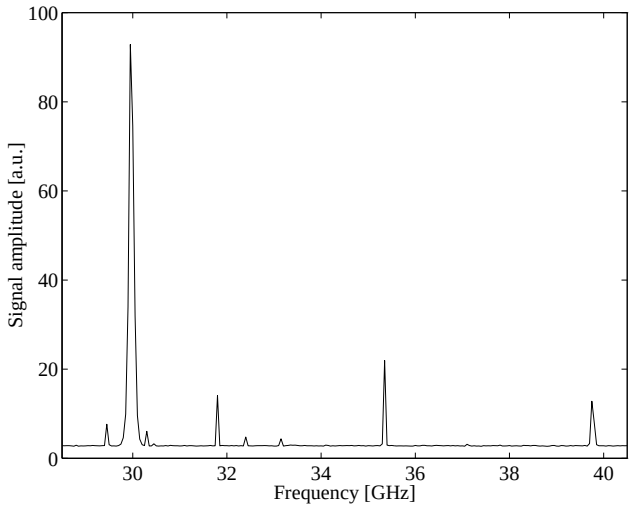


(a) Network analyser at 30 GHz.

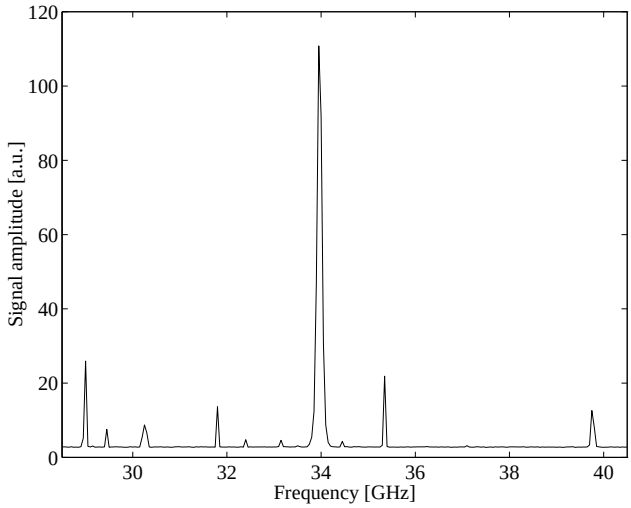


(b) Network analyser at 34 GHz.

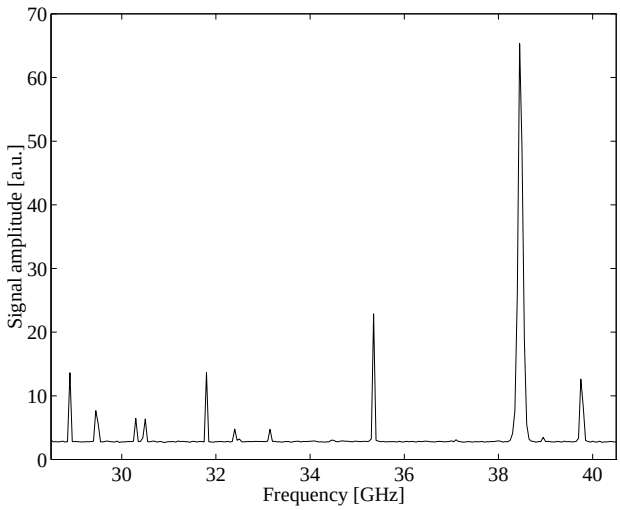


(c) Network analyser at 38.5 GHz.

Figure 5.19: Signal obtained using a network analyzer as a source.

The first measurements performed with the mixing method for a single bunch and a train of bunches are shown in Figures 5.20 and 5.21. Comparing these figures with the ones showing the expected signals they look quite different, but the response function of many elements was not known and thus, could not be used to calculate the expected signal. However, in the spectrum of a train of bunches the expected line spectrum is well visible, the line spacing of 3 GHz corresponding to the bunch time-spacing of 0.333 ns.

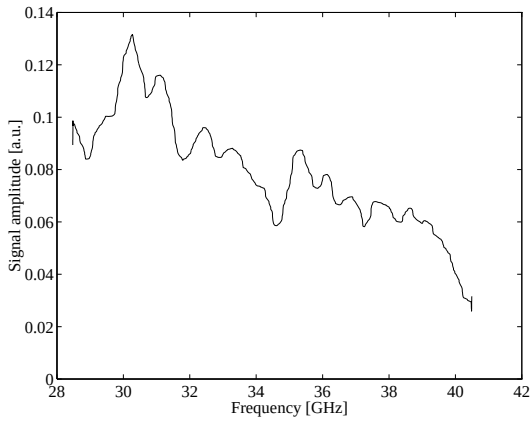


Figure 5.20: Frequency spectrum of a single bunch in the $K_a$ band.

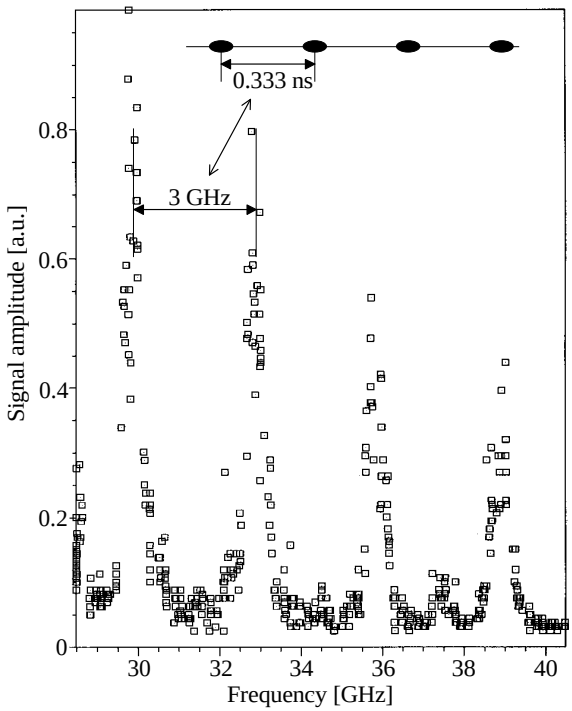


Figure 5.21: Frequency spectrum of a train of 8 bunches in the $K_a$ band.

Typical signals measured with the current experimental configuration are shown in Figures 5.22, 5.23 and 5.24 in different frequency ranges. When measuring the bunch length or calibrating the system only the frequency points under the lines are measured. For single bunch measurements only a few frequency points are measured (for simplicity the same than for a train spectrum) because measuring the whole spectrum is not necessary and it is a slow procedure. The speed of the measurement is limited by several factors. First the beam repetition frequency is 5 Hz, hence only 5 measurements per second are possible. Second, the measured bandwidth, 50 MHz, imposes small steps (<50 MHz) in the frequency scanning. And third, the fact that 25-30 measurements per frequency point are necessary to have a good average. Altogether gives between 20 to 24 minutes to determine the whole spectrum. Moreover, the speed of data transmission of the GPIB link also affects the process speed.

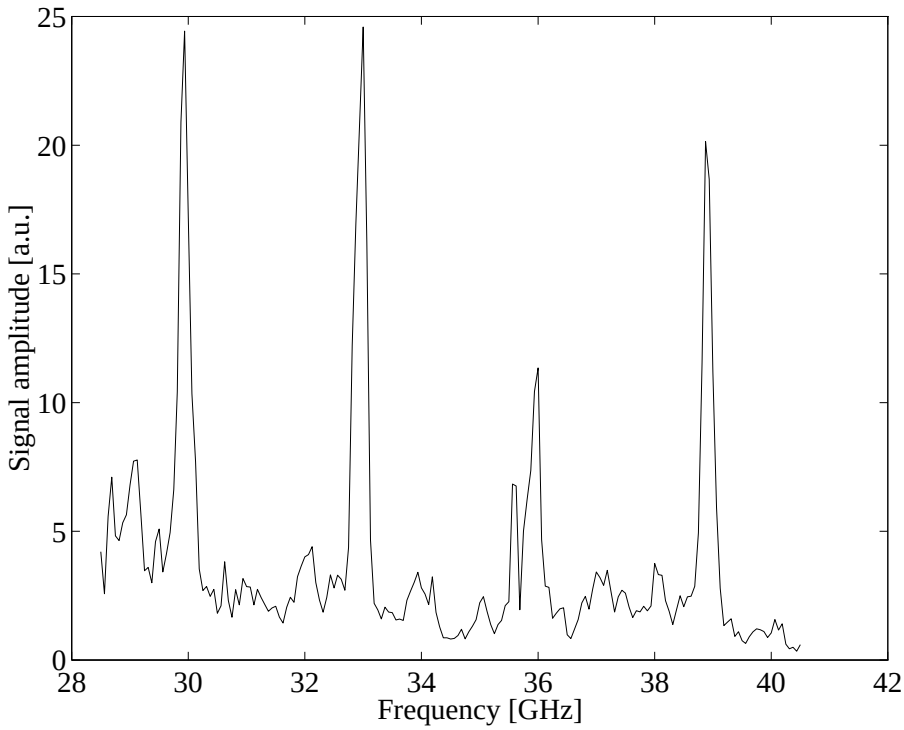


Figure 5.22: Frequency spectrum of a train of 48 bunches in the $K_a$ band.

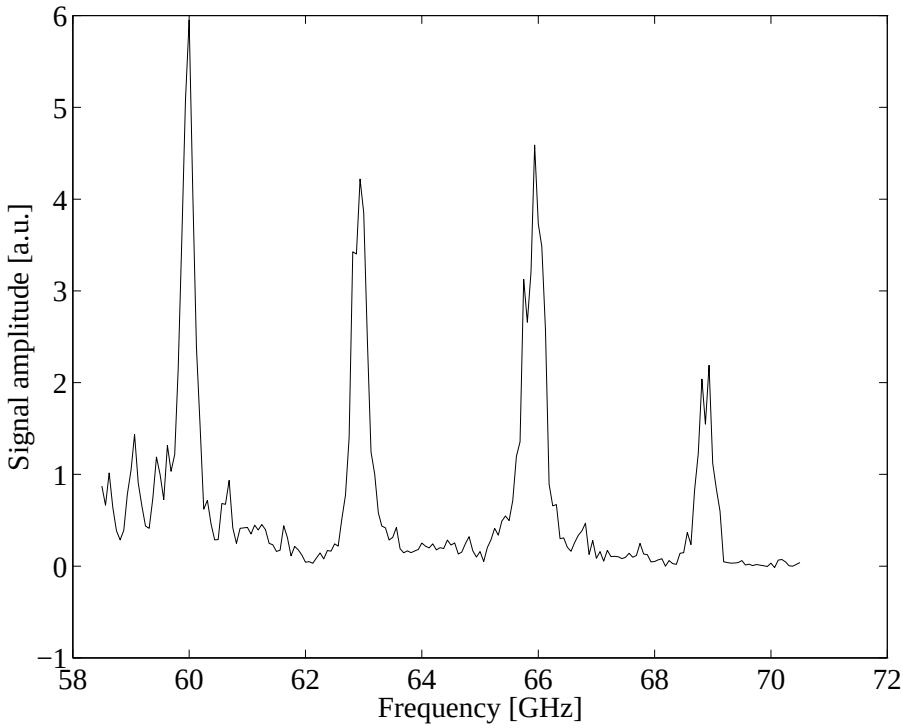


Figure 5.23: Frequency spectrum of a train of 48 bunches in the range 58.5–70.5 GHz.

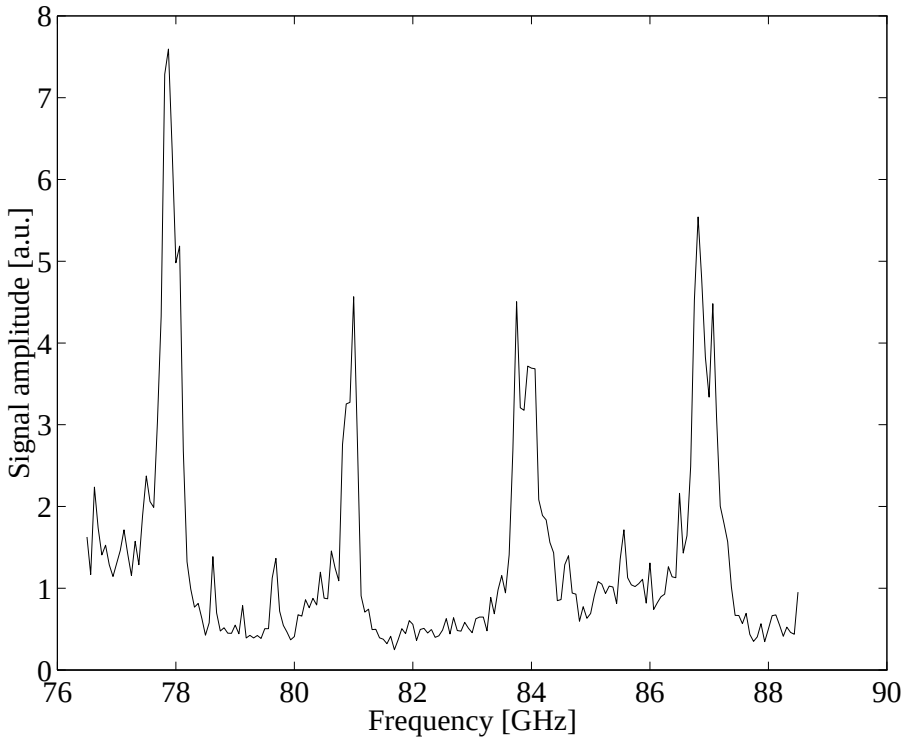


Figure 5.24: Frequency spectrum of a train of 48 bunches in the range 76.5–88.5 GHz.

In Figures 5.25, 5.26 and 5.27 are shown the frequency spectrum of 48 bunches before and after compression. The increase in the signal level is specially significative in the E band (as expected). The line at 69 GHz is not visible because it is partly suppressed by the low-pass reflecting filter characteristics and at the same time it is very sensitive to the position of this filter. The line at 84 GHz is also sensibly smaller than other lines, but that is not always the case as is shown in Figure 5.24. This was probably caused by the positioning of the high-pass filter that changed from one measurement to the other, showing that the signal is fairly sensitive to a change in the position of this high-pass filter. This has motivated the study of a new set-up that should allow to find the position which best shows all the lines and then can be fixed in this configuration.

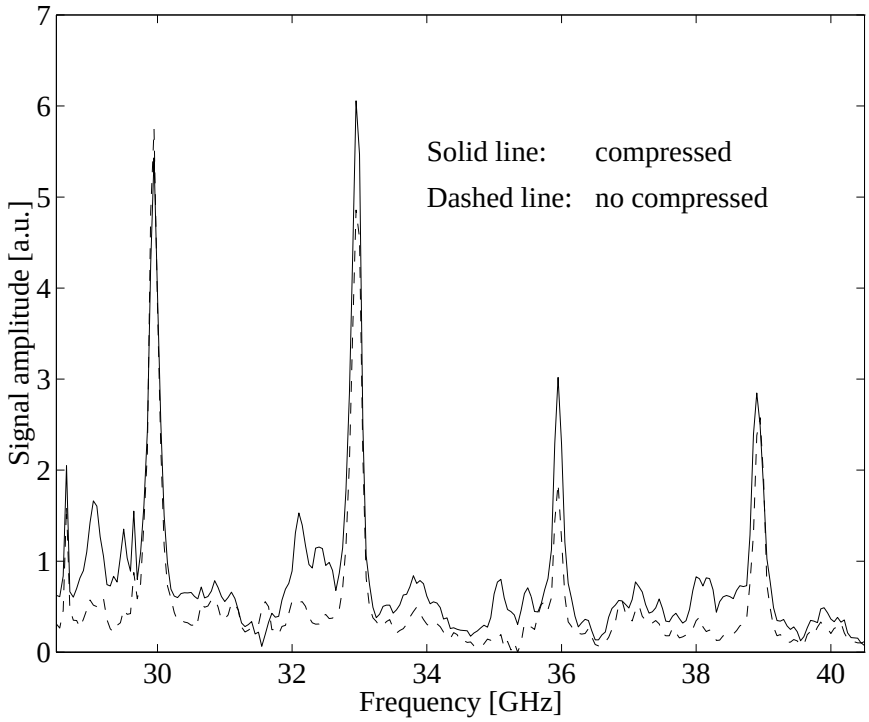


Figure 5.25: Compression spectrum of a train of 48 bunches in the $K_a$ band.

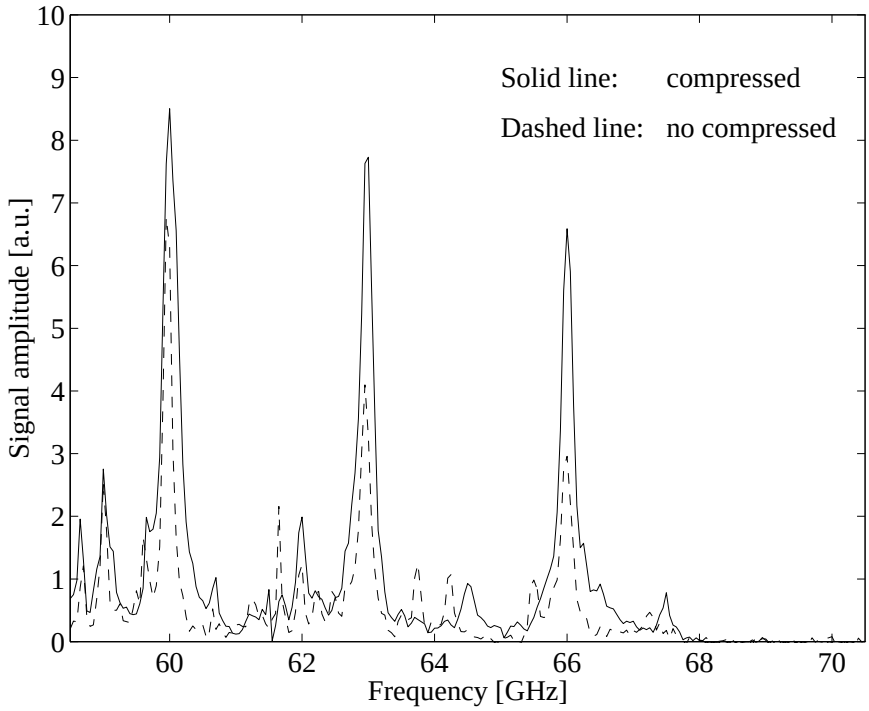


Figure 5.26: Compression spectrum of a train of 48 bunches in the frequency range 58.5–70.5 GHz.

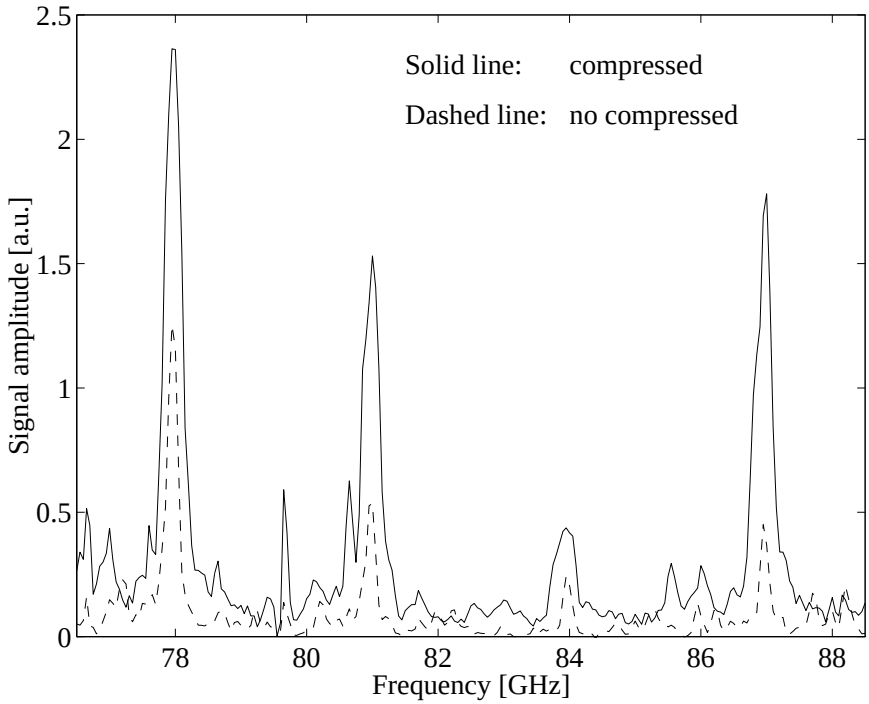


Figure 5.27: Compression spectrum of a train of 48 bunches in the frequency range 76.5–88.5 GHz.

The mixers used in the detection system work symmetrically on both sides of the LO frequency. Therefore if the high-pass filter in the E band is suppressed, it should be possible to see the lines of the train spectrum that are above and below the LO frequency (74.5 GHz). Figure 5.28 shows the lines above the LO frequency, that is 78, 81, 84 and 87 GHz, and below, that is 77, 80, 83, 86 GHz in the plot that correspond to the "real" frequencies of 72, 69, 66 and 63 GHz respectively.

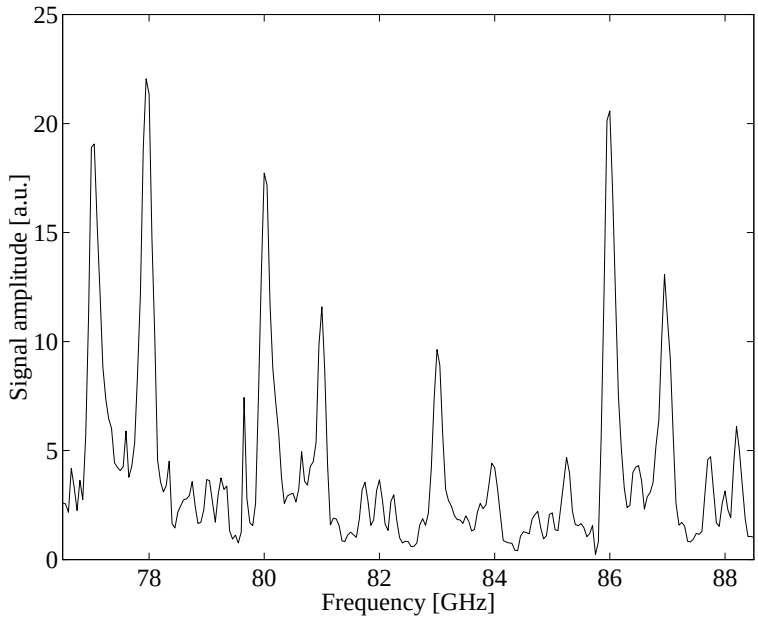


Figure 5.28: Spectrum of a train of bunches showing the lines above and below the LO frequency (74.5 GHz).

### 5.2.3 Absolute Calibration

Since the calibration of the system by measuring the frequency response of all the elements failed, a new method was developed. This method can give the bunch length by making two different measurements (for different bunch lengths) at two different frequencies points. Although the method is theoretically possible, it does not work in practice because the experimental measurements are not accurate enough. However, the same method but using a non-linear fitting to several measurements at several frequency points, was successfully applied to obtain the frequency response of the system as well as the bunch length. Once the frequency response of the system is known there is no need for another calibration (unless the frequency response of the system is modified) and the bunch length can be obtained from a single measurement. Nevertheless, it is recommended to perform periodic calibration of the system.

**A simple calibration procedure**

A simple method can be used to obtain the bunch length and the response function from frequency spectrum of the signal. Only two different measurements at two different frequencies are needed.

Let $\rho_i(\omega)$ be the frequency spectrum of the signal for a given bunch length as it is measured by the monitor. For two measurements for different bunch lengths, let us define $R(\omega)$ as the ratio between the two frequency spectrums,

$$R(\omega) = \frac{\rho_1(\omega)}{\rho_2(\omega)} \tag{5.1}$$

The frequency spectrum signal is composed of the frequency spectrum of the bunch, $b(\omega)$ times the frequency response of the system, $r(\omega)$ times the charge $q$,

$$R(\omega) = \frac{\rho_1(\omega)}{\rho_2(\omega)} = \frac{r(\omega)\, q\, b_1(\omega)}{r(\omega)\, q\, b_2(\omega)} \tag{5.2}$$

where the frequency response stays the same for the different measurements. For not too high frequencies (see Equation 3.3)

$$R(\omega) = \frac{r(\omega)\, q\,(1 - \frac{1}{2}\sigma_1^2\,\omega^2)}{r(\omega)\, q\,(1 - \frac{1}{2}\sigma_2^2\,\omega^2)} = \frac{1 - \frac{1}{2}\sigma_1^2\,\omega^2}{1 - \frac{1}{2}\sigma_2^2\,\omega^2} \tag{5.3}$$

If we consider the values of the bunch spectrum at two different frequencies, labelled $a$ and $b$, the last equation becomes

$$R_a = \frac{1 - \frac{1}{2}\sigma_1^2\,\omega_a^2}{1 - \frac{1}{2}\sigma_2^2\,\omega_a^2} \qquad \text{and} \qquad R_b = \frac{1 - \frac{1}{2}\sigma_1^2\,\omega_b^2}{1 - \frac{1}{2}\sigma_2^2\,\omega_b^2} \tag{5.4}$$

solving for $\sigma_1$ in both expressions and after some algebraic manipulation we obtain:

$$\sigma_2 = \frac{1}{\omega_a\,\omega_b}\sqrt{2\,\frac{\omega_a^2 - \omega_b^2 + \omega_b^2 R_a - \omega_a^2 R_b}{R_a - R_b}} \tag{5.5}$$

where $\sigma_2$ depends only on $\omega$, $R_a$ and $R_b$ and does not depend on $\sigma_1$. Therefore, it is possible to obtain the value of the length provided that we have two measurements for two different bunch lengths. Moreover, the response functions, $r(\omega_a)$ and $r(\omega_b)$ can be also computed from the above equations, so that is for further measurements is no longer necessary to follow this process, but one can compute the bunch length directly from

$$\rho(\omega) = r(\omega)\, q\left(1 - \frac{1}{2}\sigma^2\omega^2\right) \tag{5.6}$$

In practice this method, using two frequencies, did not work, the accuracy of the measurement was not good enough for a direct computation of the bunch length. As an alternative, a calibration using a non-linear fitting was successfully applied to the experimental data as described in next section.

### Calibration by means of a non-linear fitting procedure

In order to calibrate the system several measurements for different bunch lengths are needed. From these measurements only the value of the signal at some frequency points is used. These frequency points are multiples of 3 GHz, as this is the repetition frequency when working with a train of bunches, but for a single bunch any points would be valid. Let us suppose we have $m$ measurements (for $m$ different bunch lengths) and we used the values of the amplitude at $n$ frequency points. Neither the values of the length nor the response of the system at the different frequency points are known, therefore we have a system of $m \times n$ equations with $m+n$ unknown parameters, some of them with a non-linear dependence.

We have to consider a fitting for a system of $m \times n$ equations with nonlinear dependence on the $m+n$ unknown parameters. Starting with some trial values for the parameters a minimisation procedure for $\chi^2$ is iteratively applied, where $\chi^2$ is a function of merit that determines the best-fit parameters when it reaches its minimum value. In our case

$$\chi^2 = \sum_{i=0}^{n} \sum_{j=0}^{m} (r_i q (1 - \frac{1}{2}\omega_i^2 \sigma_j^2) - \rho(\omega_i, \sigma_j))^2 \tag{5.7}$$

where $r_i$ and $\rho_i$ are the system response and the measured signal, respectively, at a frequency $\omega_i$. As can be seen a second order polynomial is used as bunch spectrum function. The function $\chi^2$ is minimised with the help of the program Matlab using a Simplex method in multidimensions.

The results of calibrations procedures done in December 1997 and July 1998 are shown in Figures 5.29 and 5.30 respectively. In the first case 9 measurements were done (for different compressor settings) and 6 frequency points were scanned (30, 39, 72, 78 and 87 GHz). In the second case 8 measurements at 12 frequency points were made (30, 33, 36, 39, 60, 63, 66, 69, 78, 81, 84 and 87 GHz), but the measurements at 69 GHz were not use because the signal starts to be suppressed by the low-pass filter around 68 GHz. In both cases the signal was measured in a range of 300 MHz around the corresponding frequency, at steps of 25 MHz and 20 MHz respectively. The area under the signal was used as an indicator of the signal amplitude and the procedure

explained above was then applied. Once the frequency response of the system is known for the frequency points that are used, the bunch length can now be directly deduced for each single measurement. The fact that the shortest bunch is at a different setting of the bunch compressor is due to different sets of machine parameters for the two cases.

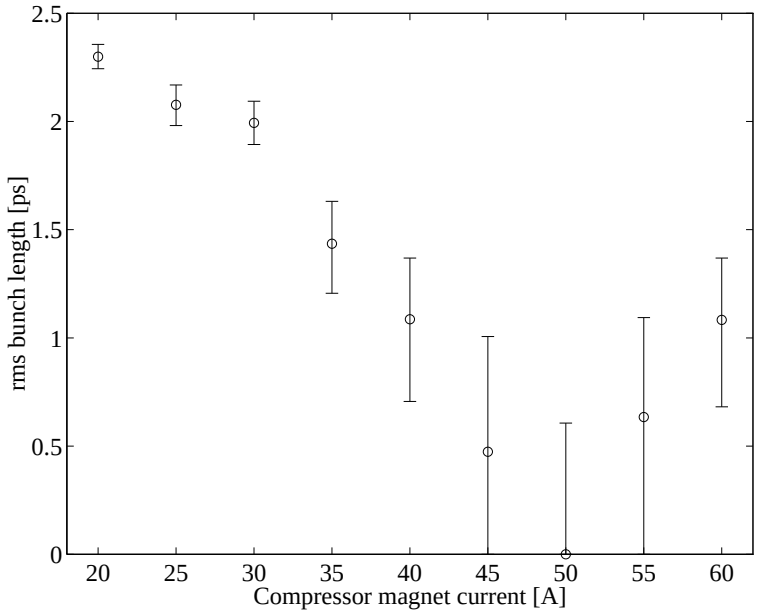


Figure 5.29: Calibration result.

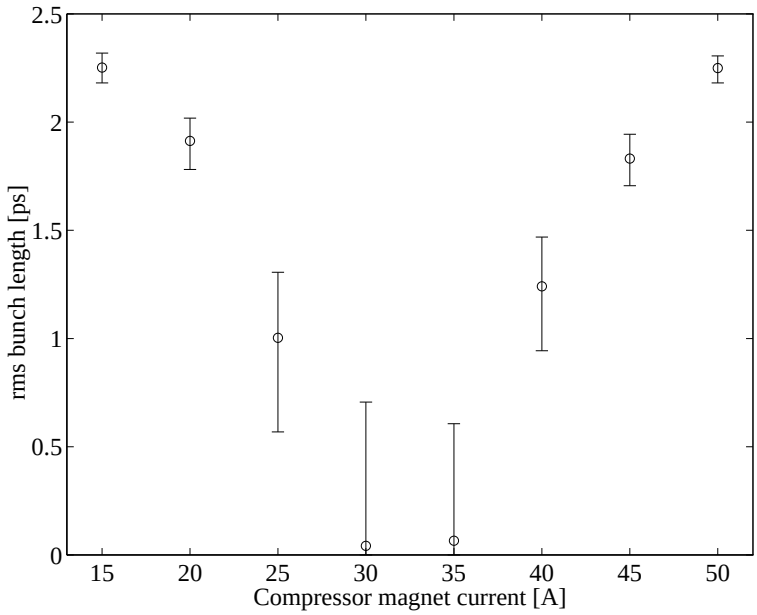


Figure 5.30: Calibration result.

The Monitor is able to measure bunches as short as 0.5 ps, although the error bar at this point has the same value than the measured length. The largest value for the error is 0.6 ps and that occurs for the shortest bunches. In Table 5.3 and 5.4 are listed the values of the measured bunch lengths with the corresponding errors.

| compressor current [A] | 20 | 25 | 30 | 35 | 40 | 45 | 50 | 55 | 60 |
|---|---|---|---|---|---|---|---|---|---|
| rms bunch length [ps] | 1.43 | 1.09 | 0.47 | 0.00 | 0.63 | 1.08 | 1.99 | 2.08 | 2.30 |
| left error [ps] | 0.23 | 0.38 | 0.47 | 0.00 | 0.63 | 0.40 | 1.00 | 0.09 | 0.05 |
| right error [ps] | 0.20 | 0.28 | 0.53 | 0.60 | 0.46 | 0.28 | 0.10 | 0.09 | 0.06 |

Table 5.3: Values of the bunch length measured in December 1997.

| compressor current [A] | 15 | 20 | 25 | 30 | 35 | 40 | 45 | 50 |
|---|---|---|---|---|---|---|---|---|
| rms bunch length [ps] | 2.25 | 1.91 | 1.00 | 0.04 | 0.06 | 1.24 | 1.83 | 2.25 |
| left error [ps] | 0.07 | 0.13 | 0.43 | 0.04 | 0.06 | 0.30 | 0.12 | 0.07 |
| right error [ps] | 0.07 | 0.10 | 0.30 | 0.66 | 0.54 | 0.23 | 0.11 | 0.06 |

Table 5.4: Values of the bunch length measured in July 1998.

The values of the frequency response of the system (and the corresponding errors) are listed in Table 5.5 and 5.6.

| Frequency [GHz] | 30 | 39 | 63 | 72 | 78 | 87 |
|---|---|---|---|---|---|---|
| response function | 12.39 | 11.68 | 1.01 | 2.40 | 9.50 | 7.87 |
| left error | 0.58 | 0.56 | 0.07 | 0.16 | 0.62 | 0.51 |
| right error | 0.59 | 0.56 | 0.06 | 0.15 | 0.63 | 0.52 |

Table 5.5: Values of the response function measured in December 1997.

| Frequency [GHz] | 30 | 33 | 36 | 39 | 60 | 63 | 66 | 78 | 81 | 84 | 87 |
|---|---|---|---|---|---|---|---|---|---|---|---|
| response function | 18.68 | 23.51 | 10.11 | 12.27 | 30.68 | 23.79 | 20.49 | 86.50 | 59.85 | 22.94 | 73.45 |
| left error | 1.97 | 2.39 | 1.08 | 1.22 | 3.89 | 2.54 | 2.15 | 9.72 | 5.84 | 2.74 | 7.79 |
| right error | 1.98 | 2.38 | 1.09 | 1.20 | 3.88 | 2.51 | 2.17 | 9.80 | 5.78 | 2.78 | 7.81 |

Table 5.6: Values of the response function measured in July 1998.

The estimation of the error associated to this calibration procedure was rather complicate because of the big number of different parameters [56]. The possible correlation

between any pair of parameters was studied by computing the variation of $\chi^2$ as a function of the these parameters. Contour plots were obtained by varying two parameters while holding all the others fixed at their optimum value (the one that minimised $\chi^2$). In an ideal case, if the two parameters are uncorrelated, in the region of the $\chi^2$ minimum the contours will be ellipses that would become circles by suitable scaling of the axis. For the measurements made in December 1997, contour plots were drawn for every possible pair of parameters demonstrating that they were uncorrelated or very weakly correlated. Some of these plots are shown in Figure 5.31. The central points (star) in these plots indicates the position of the minimum value for $\chi^2$.

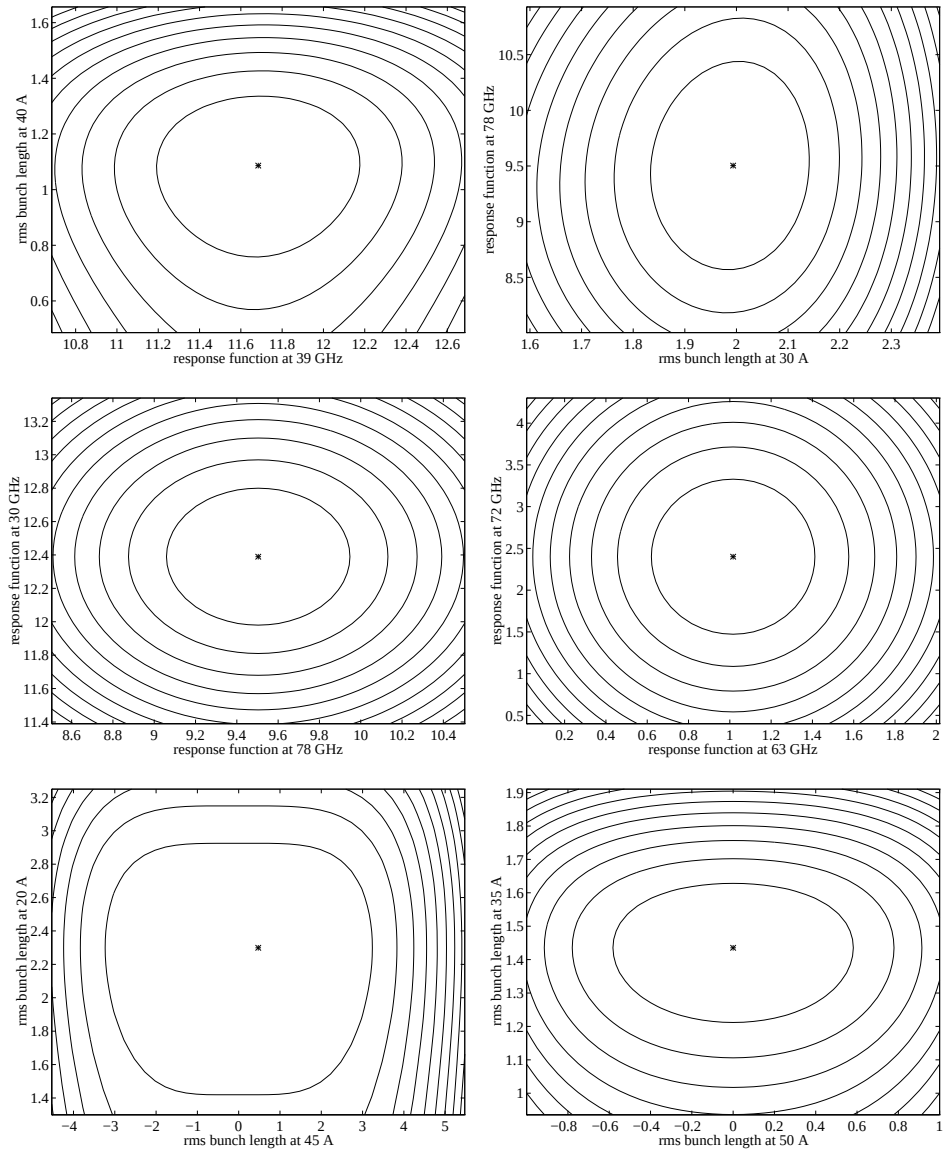


Figure 5.31: Typical correlation plots between different parameters.

Because of the apparent weak correlation between parameters the errors were estimated by varying that parameter to the left and right of the ideal value (keeping all other parameters fixed) and computing $\chi^2$ until it reached a value $\sigma$ over the minimum value. This procedure is shown in Figure 5.32, where $\chi^2$ is plotted as a function of some parameter $p$, the minimum of $\chi^2$ is at $p = p(\text{optimum})$ and $le$ and $re$ represent the error on the left and right side, respectively, of the optimum value. The value of $\sigma^2$ for $\chi^2$ is obtained by dividing $\chi^2$ by the number of degrees of freedom,

$$\sigma^2 = \frac{\chi^2}{\nu} \qquad \nu\text{: number of degrees of freedom} \tag{5.8}$$

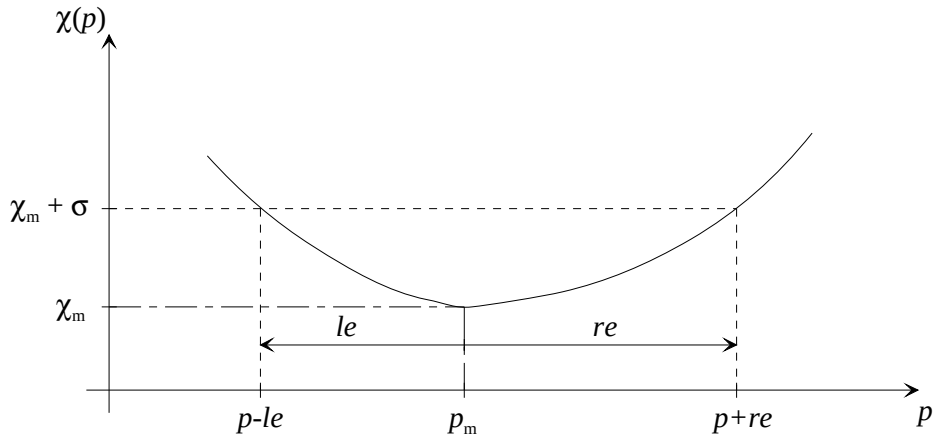


Figure 5.32: Graphical representation of the procedure to find the error for $\chi^2$

# Chapter 6

# Discussion of Results

Some of the results presented in the previous chapter are discussed and compared with the results given by another measurement method, namely Cerenkov radiation analysed with the streak camera, and with bunch length predictions given by the beam dynamics simulation programme PARMELA [57]. The comparison of these results will show, first, that the streak camera is limited by a resolution of 2 ps (rms) and, second, that the bunch length values measured with the mm-wave monitor using the mixing method are in excellent agreement with those calculated with PARMELA.

## 6.1 Results Obtained with PARMELA and the Streak Camera

A short introduction to the programme PARMELA is given first. The results obtained with both methods, the PARMELA simulations and the streak camera measurements, are discussed and then compared with the bunch length values measured with the mm-wave bunch length monitor (BLM). All the results presented in this section correspond to measurements done in the CTF on the 4th and 5th December 1997 (see Chapter 5).

### 6.1.1 Beam Dynamics Simulations with PARMELA

PARMELA is a linac particle-dynamics code. The name comes from, “Phase and Radial Motion in Electron Linear Accelerators”. It is a versatile multi-particle code that transports the beam, represented by an ensemble of particles, through a user-specified linac or transport system. It includes a 3-D point-to-point space-charge calculation. PARMELA integrates the particle trajectories through the fields. This approach is specially impor-

tant for electrons where some of the approximations used by other codes would not hold. PARMELA works equally well for either electrons or ions. PARMELA can use field distributions generated by either SUPERFISH for RF problems or POISSON [58, 59] for magnet problems.

A simulation with PARMELA was made for each compression setting used to calibrate the BLM on the 4th December 1997. These simulations included all the magnetic and RF elements in the drive beam line from the photocathode in the RF gun to the position of the RF pick-up. Space charge effects were not included because of the low charge per bunch, 1.3 nC, and the relatively high beam energy of 50 MeV. The results of these simulations are listed in Table 6.1.

| Compressor current [A] | 20 | 25 | 30 | 35 | 40 | 45 | 50 | 55 | 60 |
|---|---|---|---|---|---|---|---|---|---|
| rms bunch length [ps] | 2.16 | 2.04 | 1.74 | 1.40 | 0.98 | 0.59 | 0.42 | 0.72 | 1.32 |

Table 6.1: Bunch lengths calculated with PARMELA.

These results show that the bunches are (theoretically) compressed down to 0.4 ps rms, the minimum length corresponding, in this case, to a electric current of 50 A in the compressor end magnets.

### 6.1.2 Results from the Streak Camera

In the CTF the streak camera obtains information about the longitudinal bunch distribution by analysing the transition or Cerenkov radiation produced in the TCMs. Details about the streak camera working principle can be found in Chapter 2.

The values of the bunch lengths measured with the streak camera for each compression setting are listed in Table 6.2. These results are plotted together with the bunch length values given by PARMELA in Figure 6.1. It is clearly seen, in this figure, that the streak camera is not able to measure a bunch length smaller than 1.9 ps rms even if, theoretically, the bunches are as short as 0.4 ps.

| Compressor current [A] | 20 | 25 | 30 | 35 | 40 | 45 | 50 | 55 | 60 |
|---|---|---|---|---|---|---|---|---|---|
| rms bunch length [ps] | 2.67 | 2.46 | 2.33 | 2.29 | 2.08 | 2.04 | 1.91 | 1.87 | 1.91 |

Table 6.2: Bunch length measured by the streak camera.

The resolution of the measurements made with the streak camera is the sum of the resolution of the streak camera itself plus the dispersion introduced by the optical path

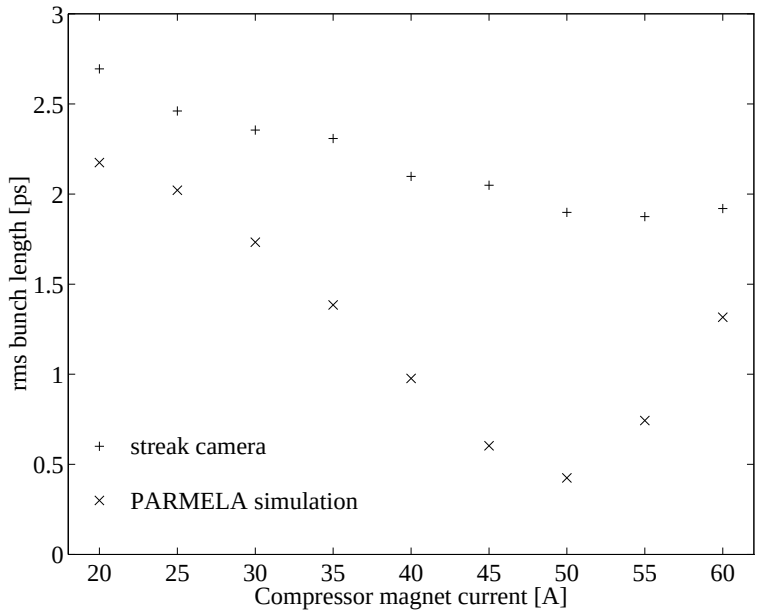


Figure 6.1: Bunch length obtained with the streak camera and PARMELA simulations.

that leads the light from the TCM to the streak camera. The camera has a resolution of about 1 ps (rms) and the optical path is responsible for the remaining 1 ps (rms).

## 6.2 Calibration of the mm-Wave Monitor

In the previous chapter (Chapter 5) were presented the results of the calibration procedure done in December 1997. Those measurements showed that the mm-wave monitor, using the mixing technique, can measure bunches as short as 0.6 ps although the precision is of $\pm 0.5$ ps. The measured bunch length values, together with the associated errors, are listed in Table 6.3 and then plotted in Figure 6.2.

| compressor current [A] | 20 | 25 | 30 | 35 | 40 | 45 | 50 | 55 | 60 |
|---|---|---|---|---|---|---|---|---|---|
| rms bunch length [ps] | 1.43 | 1.09 | 0.47 | 0.00 | 0.63 | 1.08 | 1.99 | 2.08 | 2.30 |
| left error [ps] | 0.23 | 0.38 | 0.47 | 0.00 | 0.63 | 0.40 | 1.00 | 0.09 | 0.05 |
| right error [ps] | 0.20 | 0.28 | 0.53 | 0.60 | 0.46 | 0.28 | 0.10 | 0.09 | 0.06 |

Table 6.3: Values of the bunch length measured in December 1997.

As described is Chapter 5 these results were obtained by measuring 6 frequency points (30, 39, 63, 72, 78 and 87 GHz) for 9 different settings of the bunch compressor. A non-linear fitting routine finds, by minimising $\chi^2$, the bunch length values as well as

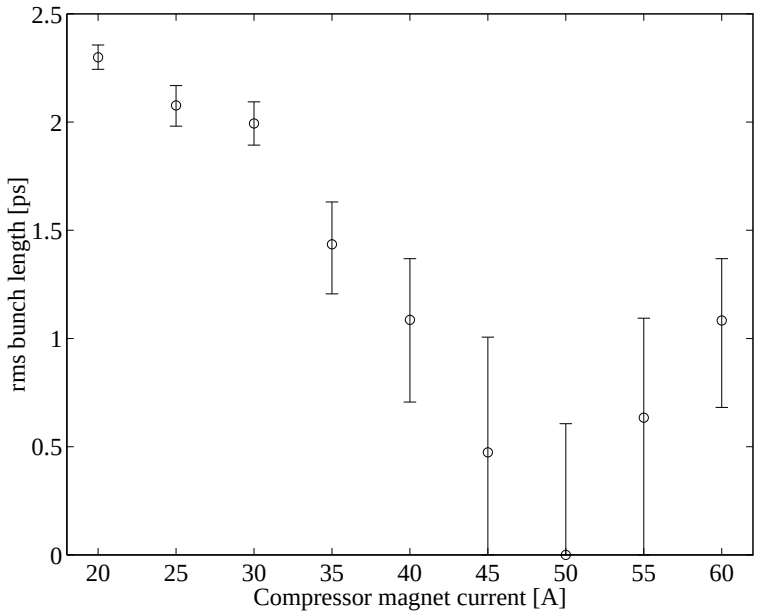


Figure 6.2: Bunch lengths measured with the mm-wave monitor in December 1997.

the response function at each measured frequency. It was also possible to demonstrate that all these parameters (bunch lengths and response functions) were almost uncorrelated and the error associated to each measurement was calculated by varying each bunch length until the corresponding $\chi^2$ reached a value $\pm\sigma$ of the minimum value.

The error bars are larger for the shortest bunches. When the bunch length is reduced higher frequencies of the bunch spectrum are excited. For a very short bunch the bunch spectrum in the frequency range measured by the monitor is quite flat (see Chapter 3) so that the fitting routing cannot properly fit a second order polynomial trough the different points. For the shortest bunch the spectrum is almost flat and for a horizontal line $\sigma = 0$ and the associated error is very large. In the next table are listed the ratio of the amplitude of the bunch spectrum at 87 GHz to the amplitude at 30 GHz for several bunch lengths.

| | $\sigma = 0.5$ ps | $\sigma = 1$ ps | $\sigma = 2$ ps |
|---|---|---|---|
| $\frac{\text{Amplitude at 87 GHz}}{\text{Amplitude at 30 GHz}}$ | 0.97 | 0.88 | 0.59 |

One possibility to increase the precision of the measurement would be to measure higher frequencies, but the present limitation for the resolution of the measurements is the pulse to pulse jitter, of about 10%, of the electron beam charge. The effect of such a jitter on the measurement would be reduced by measuring simultaneously, to the bunch length, the charge of the beam.

## 6.3 mm-Wave Monitor versus Streak Camera

It was already obvious from the previous sections that the mm-wave monitor has a much better resolution than the streak camera. Figure 6.3 shows both, the streak camera and the mm-wave results, together for a better comparison. The mm-wave monitor shows a better resolution in all cases, and not only for the shortest bunches, although in these cases is specially noticeable.

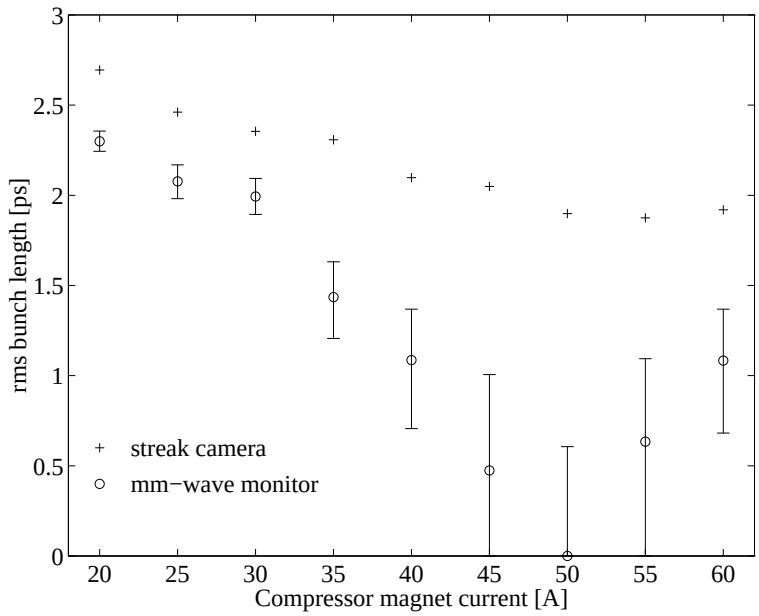


Figure 6.3: Bunch lengths measured with the mm-wave monitor and the streak camera.

## 6.4 mm-Wave Monitor versus PARMELA

Figure 6.4 shows both, the PARMELA and the mm-wave results for the bunch length. The agreement between both sets of results is very good.

The mm-wave monitor resolution is about 0.7 ps (the smallest value measured) so that it is already not possible to resolve the shortest bunch length (0.42 ps calculated with PARMELA), although this value is anyhow in the range covered by the error bars. In two cases the monitor results have a small disagreement with the PARMELA results, at 20 and 30 A, that was thought to be caused by an increase of the bunch charge when measuring these points. The laser pulses that create the bunches were, during the whole period of experiments, not very stable and there were variations in the charge per bunch from pulse to pulse.

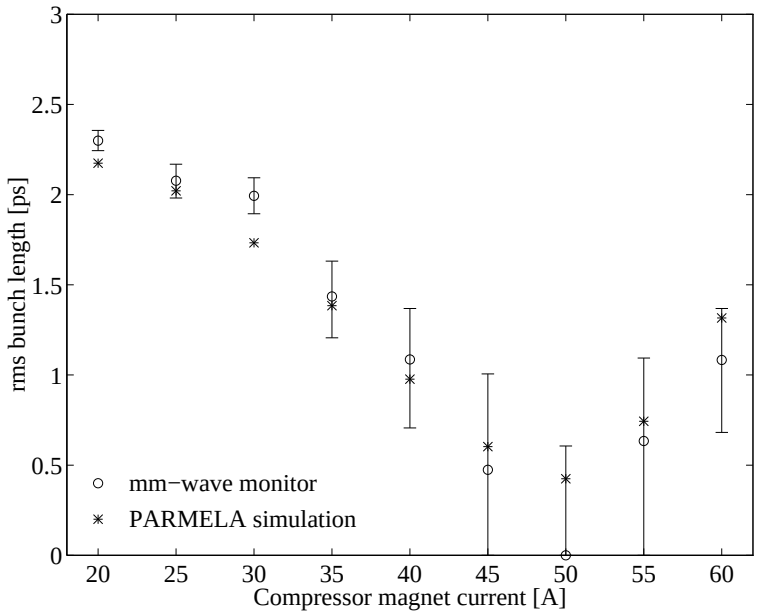


Figure 6.4: Bunch lengths measured with the mm-wave monitor and PARMELA.

# Chapter 7

# Summary and Concluding Remarks

The present work describes the design, installation, testing and operation of a novel non-intercepting bunch length monitor for very short electron bunches. The main achievements are hereby summarised.

The CTF studies the production of power at 30 GHz by means of an electron beam with very short bunches ($\leq$ 2 ps rms). In order to study the efficiency of the power production it is necessary to know the electron bunches length. Conventional bunch length measurements techniques did not have the required resolution to measure the CTF bunches and in most cases were destructive or very perturbative. At the moment this thesis work started the length of the CTF electron bunches was measured with a streak camera using Cerenkov or transition radiation produced by the beam going through a sapphire sheet or an aluminium foil respectively. The resolution of such a system was of the order of 2 ps rms.

Following the study of the state of the art in bunch length measurements techniques it was decided to start the design of a new monitor. The new bunch length monitor is based on the measurement of the frequency spectrum of the electromagnetic field of the bunch. The bunch length is then obtained by studying the variation of the signal amplitude with frequency.

- The electromagnetic field of the electron bunch is collected by a non-destructive RF pick-up. The RF pick-up consists of a rectangular waveguide coupled to a rectangular hole (of the same dimensions) made on the beam pipe surface.

- The frequency response of the pick-up was computed with the help of MAFIA, a program package for the computation of electromagnetic fields by solving the Maxwell's equations.

Two different detection systems have been designed to obtain the frequency spectrum of the bunch from the collected signal. The first uses a diode detector and the second is a system of RF mixers in combination with a sweeping oscillator, that acts as a frequency analyzer for very short duty cycle signals. Both systems were installed and tested in the CTF. The final set-up installed in the CTF could measure the bunch spectrum in three different frequency bands: 26.5–40 GHz, 60–74.5 GHz and 74.5–90 GHz.

- A series of microwave filters were designed and fabricated to be installed in the CTF set-up. These filters consisted of metal plates perforated with cylindrical holes. A new feature was added to improve the filtering properties: conical endings to the cylindrical holes to avoid resonances.

- The diode detector proved to be a very useful tool to tune the accelerator. With this method single shot measurements of the signal are obtained, giving a fast qualitative information of the variation of the bunch length. However, this method is not well adapted for quantitative bunch length measurements because of the difficulties to obtain an absolute calibration.

- The mixing technique detection is able to measure the spectra of a single bunch as well as that of a train of bunches, although an average over several bunches is necessary. An independent self-consistent calibration technique has been developed to obtain the frequency response of the system. The mixing technique has demonstrated its capability to measure bunches as short as 0.7 ps rms. Furthermore, it showed a very good agreement with the theoretical bunch length values obtained with the code PARMELA.

- The acquisition procedure is controlled remotely by means of a PC and specially made programs. Additional programs were written to calibrate the system and to obtain the bunch length in real time.

- The system is now routinely in use in the CTF.

## 7.1 Future upgrades

During the last stages of the thesis work, and after analysing the experimental results, several possible improvements or upgrades were already proposed for the current installation so that it will be possible to measure shorter bunches with even a better resolution.

- The construction of an electromagnetic isolation for the detection system is already underway.

- One possibility to measure shorter bunches would be the increase of the measured frequency band to higher frequencies, this could be accomplished by installing a waveguide of smaller transversal dimensions and a detection system similar to the ones already in use.

- It was notorious during the experimental part of this thesis work that the laser system had a energy jitter from pulse to pulse that caused variations in the bunch charge. It would be desirable, to improve the quality of the measurements, an stable production of electron bunches, with the smallest possible variation in the bunch charge. That kind of improvement is, of course, limited by the time available and, especially, the budget. An alternative solution to avoid the effect of the charge variation is described below.

- The resolution of the system is mainly limited by the jitter in the pulse to pulse bunch charge. In order to achieve a better resolution the bunch charge should be measured at the same time than the signal coming from the bunch, so that, the oscilloscope (or the acquisition program) could normalise the signal to the charge for each measurement.

# Appendix A

# List of Common Acronyms and Abbreviations

| | |
|---|---|
| CERN | European Laboratory for Particle Physics |
| LHC | Large Hadron Collider |
| CLIC | Compact LInear Collider (CERN project) |
| CTF | CLIC Test Facility |
| LEP | Large Electron Positron (collider) |
| LIL | LEP Injector Linac |
| BLM | Bunch Length Monitor (presented in this thesis) |
| TCM | Transition - Cerenkov Monitor |
| BPM | Beam Position Monitor |
| WCM | Wall Current Monitor |
| PM | Phase Monitor |
| LO | Local Oscillator |
| CAS | CLIC Accelerating Structure |
| CTS | CLIC Transfer Structure |
| HCS | High Charge (Accelerating) Structure |
| LAS | LIL Accelerating Structure |
| MAFIA | Solution of MAxwell's equations by the Finite Integration Algorithm |
| PARMELA | Phase and Radial Motion in Electron Linear Accelerators (tracking code) |
| FFT | Fast Fourier Transform |
| IFFT | Inverse Fast Fourier Transform |
| $K_a$ (band) | Frequency range: 26.5–40 GHz |
| E (band) | Frequency range: 60–90 GHz |
| TM | Transverse Magnetic (mode) |

| | |
|---|---|
| TE | Transverse Electric (mode) |
| CCD | Charge Coupled Device |
| rms | Root mean square |
| fwhm | Full width at half maximum |

# Bibliography


[1] http://wwwlhc01.cern.ch/, "The Compact Linear Collider study web information pages."

[2] http://www.cern.ch/CERN/Divisions/PS/CLIC/, "The Large Hadron Collider project web information pages."

[3] J.-P. Delahaye for the CLIC study team, "CLIC, a 0.5 to 5 TeV $e^+e^-$ Compact Linear Collider," in *proceedings of the 1998 EPAC, Stockholm, Sweden*, pp. 58–62, June 1998. CERN/PS/LP 98-009.

[4] W. Schnell, "A two-stage rf linear collider using a superconducting drive linac," in *proceedings of the 1986 Workshop on New Techniques for Future Accelerators, Erice, Italy*, May 1986. Note CERN/LEP/RF 86-06 and CLIC 13.

[5] H. Braun, R. Corsini, T. D'Amico, J. Delahaye, G. Guignard, C. Johnson, A. Millich, P. Pearce, L. Rinolfi, A. Riche, R. Ruth, D. Schulte, L. Thorndahl, M. Valentini, and I. Wilson, "A new method of rf power generation for two-beam linear colliders," in *proceedings of the 1998 European Particle Accelerator Conference, Stockholm, Sweden*, pp. 248–252, June 1998. Note CERN/PS/LP 98-014 and CLIC 367.

[6] J. Madsen, "Results with the CTF in 1995," CLIC Note 296, CERN, 1996.

[7] Y. Baconnier, R. Bossart, J. Delahaye, K. Geissler, J. Godot, K. Hübner, J. Madsen, J. Potier, A. Riche, J. Sladen, G. Suberlucq, I. Wilson, and W. Wuensch, "The CERN Linear Collider Test Facility (CTF)," PS/LP 92-49, CERN, 1992.

[8] The CLIC study group, "CTF2 design report," PS/LP Note 96-14, CERN, 1996. Also CLIC Note 304.

[9] http://nicewww.cern.ch/ ctfop, "The CLIC Test Facility web information pages."

[10] G. Suberlucq, "Développement et production de photocathodes," CLIC Note 299, CERN, 1996.

[11] E. Chevallay, J. Durand, S. Hutchins, G. Suberlucq, and H. Trautner, "Photocathodes for the CERN CLIC Test Facility," in *proceedings of the 1998 International Linac conference, Chicago, USA*, August 1998. CERN/PS/LP 98-036.

[12] S. Hutchins, "The CTF laser system," CTF Note 98-18, CERN, 1998.

[13] J. Bouché, W. Coosemans, and R. Pittin, "Active alignment system for CLIC 30 GHz modules in CTF2," in *proceedings of the 1997 Fith International Workshop on Accelerator Alignment, Argonne National Laboratory, USA*, October 1997.

[14] R. Bossart, H. Braun, M. Dehler, and J. Godot, "A 3 GHz photoelectron gun for high beam intensity," PS/RF Note 95-25, CERN, 1996. Also CLIC Note 297.

[15] M. Valentini and H. Braun, "Analytical calculation of beam loading compensation in the High Charge Structures," CTF Note 98-05, CERN, 1998.

[16] F. Chautard, *Un compresseur de paquets d'électrons fortement chargés au CERN*. PhD thesis, Université Paris 6, 1996.

[17] K. Aulenbacher, H. Braun, F. Chautard, R. Corsini, J. Madsen, and L. Rinolfi, "Bunch compressor performance at the CLIC Test Facility," PS/LP Note 96-27, CERN, 1996. Also CLIC Note 307.

[18] R. Bossart, H. Braun, G. Carron, M. Chanudet, F. Chautard, J. Delahaye, J. Godot, S. Hutchins, I. Kamber, C. Martínez, G. Suberlucq, L. Thorndal, M. Valentini, I. Wilson, and W. Wuensch, "Demonstration of two-beam acceleration in CTF II," in *proceedings of the 1998 International Linac Conference, Chicago, USA*, August 1998. CERN/PS/LP 98-038.

[19] H. Braun, "Methods for measuring short electron bunches," CTF Note 95-19, CERN, 1995.

[20] V. Ginzburg, *Radiation by uniformly moving sources*. The lesson of quantum theory, Elsevier Science Publishers, 1986.

[21] S. Battisti, "Measurement of the short bunch length in the CLIC Test Facility," CERN/PS Note 93-40 (BD), CERN, 1993. CLIC Note 211.

[22] Y. Pellegrina, "Radiation de transition – Radiation Cerenkov," PS/LP Note 89-30, CERN, 1989.

[23] J. Jelley, *Cerenkov radiation and its applications*. Pergamon Press, 1958.

[24] M. Cuzin and C. Bovet, "Single-shot temporal measurements of short x-ray pulses using very fast photoconductive detectors," in *proceedings of the Third European Workshop on Room Temperature Semiconductor X and Gamma Ray Detectors Associated Electronics and Application, Grenoble, France*, September 1995. Also: CERN-SL-95-77.

[25] C. Bovet, D. Cocq, A. Manarin, E. Rossa, H. Schmickler, and G. Voors, "Measurement results with the BEXE detector at LEP," in *proceedings of the Third European Workshop on Beam Diagnostics and Instrumentation for Particle Accelerators (DIPAC97), Frascati, Italy*, October 1997. Also: CERN-SL-97-70 (BI).

[26] E. Rossa, N. Adams, F. Tomasini, and J.-M. Roth, "Double sweep streak camera for LEP," in *proceedings of the 1990 EPAC, Nice, France*, June 1990. Also: CERN/SL Note 90-24 (BI).

[27] H. Euteneuer, H. Herminghaus, K. Nilles, and H. Schöler, "Fast longitudinal phase space diagnostics for the injector linac of MAMI," in *proceedings of the 1988 EPAC, Rome, Italy*, pp. 1149–1150, June 1988.

[28] Y. Bylinsky, A. Feschenko, A. Liiou, A. Menshov, P. Ostroumov, H. Kugler, and K. Williams, "Bunch length and velocity detector and its application in the CERN heavy ion linac," in *proceedings of the 1994 EPAC, London, U.K.*, pp. 1702–1704, June 1994.

[29] A. Feschenko and P. Ostroumov, "Bunch shape analyser with transverse scanning of the low energy secondary electrons," in *proceedings of the 1990 EPAC, Nice, France*, pp. 750–752, June 1990.

[30] J. Hurd, G. Arbique, C. Crist, F. Guy, G. Leifeste, D. Raparia, K. Saadatmand, D. Swenson, S. Esin, A. Feschenko, A. Stepanov, and A. Mirzojan, "Bunch shape monitor for SSCL linac," in *proceedings of the 1993 PAC, Washington D.C., U.S.A.*, pp. 2426–2428, May 1993.

[31] C. Hirschmugl, M. Sagurton, and G. Williams, "Multiparticle coherence calculations for synchrotron-radiation emission," *Physical Review A*, vol. 44, pp. 1316–1320, July 1991.

[32] D. Bocek, P. Kung, H.-C. Lihn, C. Settakorn, and H. Wiedemann, "Measurement of subpicosecond electron bunch lengths," SLAC-PUB 95-7052, SLAC, 1995.

[33] R. Lai and A. Sievers, "Determination of a charged-particle-bunch shape from the coherent far infrared spectrum," *Physical Review E*, vol. 50, pp. 3342–3344, November 1994.

[34] R. Lai, U. Happek, and A. Sievers, "Measurement of the longitudinal asymmetry of a charged particle bunch from the coherent synchrotron or transition radiation spectrum," *Physical Review E*, vol. 50, pp. 4294–4297, December 1994.

[35] E. Babenko, R. Jobe, K. McCormick, and J. Seeman, "Length monitor for 1 mm SLC bunches," in *proceedings of the IEEE PAC 93, Washington D.C., U.S.A.*, pp. 2423–2425, May 1993. Also: SLAC-PUB-6202.

[36] E. Babenko, "Length monitors for single bunches," SLAC Note CN-396, SLAC, 1993.

[37] Z. Greenwald, D. Hartill, R. Littauer, S. Peck, and D. Rice, "Bunch length measurement using beam spectrum," in *proceedings of the IEEE PAC 91, New York, U.S.A.*, pp. 1246–1248, May 1991. Also: CLNS Note 91-1084.

[38] A. Nassiri and A. Grelick, "A fifth harmonic RF bunch monitor for the ANL-APS electron linac," in *proceedings of the IEEE PAC 93, Whasington D.C., U.S.A.*, pp. 2412–2414, May 1993.

[39] S. Jing and S. Song, "Bunch length information in wall current signal," BIHEP-DE 90-SJ15, BIHEP, 1990.

[40] J. Swartz, B. Guenther, F. D. Lucia, W. Guo, C. Jones, H. Kosai, and J. Dutta, "Non-destructive diagnostics for relativistic picosecond bunched electron beams," *Physical Review E*, vol. 52, pp. 5416–5424, November 1995.

[41] F. Zimmermann, G. Yocky, D. Whittum, M. Seidel, P. Raimondi, C. Ng, D. McCormick, and K. Bane, "An RF bunch length monitor for the SLC final focus," in *proceedings of the IEEE PAC 97, Vancouver, BC, Canada*, pp. 2189–2191, May 1997. Also: SLAC-PUB-7456.

[42] CST (Computer Simulation Technology), *MAFIA Release 4.00 Manual*. CST, Darmstadt, Germany, first ed., 1997.

[43] L. Rivkin, "Beamstrahlung and disruption," in *proceedings of the 1993 CERN Accelerator School, Rhodes, Greece* (S. Turner, ed.), pp. 557–572, November 1995. CERN 95-06.

[44] E. Keil, "Beam-beam dynamics," in *proceedings of the 1993 CERN Accelerator School, Rhodes, Greece* (S. Turner, ed.), pp. 539–555, November 1995. CERN 95-06.

[45] R. E. Collin, *Field theory of guided waves*. McGraw-Hill Book Company, Inc., 1960.

[46] N. Marcuvitz, *Waveguide Handbook*. Peter Peregrinus Ltdl, London, UK, 1986.

[47] R. Ulrich, "Inductive grids in the region of diffraction anomalies: Theory, experiment, and applications," *Applied Optics*, vol. 7, pp. 1987–1996, October 1968.

[48] T. Timusk and P. Richards, "Near millimeter wave bandpass filters," *Applied Optics*, vol. 8, pp. 1355–1360, April 1981.

[49] R. Compton, "Bandpass filters: Theory and experiments," *Applied Optics*, vol. 22, pp. 3920–3924, December 1983.

[50] A. Roberts, M. von Bibra, H.-P. Gemünd, and E. Kreysa, "Thick grids with circular apertures: a comparison of theoretical and experimental performance," *International Journal of Infrared and Millimetre Waves*, vol. 15, no. 3, pp. 505–517, 1994.

[51] C.-C. Chen, "Transmission through a conducting screen perforated periodically with apertures," *IEEE Transactions on Microwave Theory and Techniques*, vol. MTT-18, pp. 627–632, September 1970.

[52] C.-C. Chen, "Diffraction of electromagnetic waves by a conducting screen perforated periodically with circular holes," *IEEE Transactions on Microwave Theory and Techniques*, vol. MTT-19, pp. 475–481, May 1971.

[53] P. Bliek, L. Botten, R. Deleuil, R. McPhedran, and D. Maystre, "Inductive grids in the region of diffraction anomalies: Theory, experiment, and applications," *IEEE Transactions on Microwave Theory and Techniques*, vol. MTT-28, pp. 1119–1125, October 1980.

[54] N. Amitay and V. Galindo, "The analysis of circular waveguide phased arrays," *Bell Systems Technical Journal*, vol. 47, pp. 1903–1932, November 1968.

[55] F. Chautard, “CTF II parameter list,” CTF Note 97-08, CERN, 1997.

[56] P. Bevington and D. Robinson, *Data reduction and error analysis for the physical sciences*. McGraw-Hill, Inc., second ed., 1992.

[57] B. Mouton, “The PARMELA program,” LAL/SERA Note 93-455, LAL-Orsay, 1993.

[58] M. Menzel and H. Stokes, “User’s guide for the POISSON/SUPERFISH group of codes,” LANL Report LA-UR-87-115, Los Alamos National Laboratory, 1987.

[59] LAACG, “Los Alamos Accelerator Code Group “POISSON/SUPERFISH“ reference manual,” LANL Report LA-UR-87-126, Los Alamos National Laboratory, 1987.